Studies of Heterogeneously Catalyzed Liquid-Phase Alcohol Oxidation on Platinum by Sum-frequency Generation Vibrational Spectroscopy and Reaction Rate Measurements

By

Christopher Mark Thompson

A dissertation submitted in partial satisfaction of the requirements for the degree of

Doctor of Philosophy

in

Chemistry

in the

Graduate Division

of the

University of California, Berkeley

Committee in charge:

Professor Gabor A. Somorjai, Chair
Professor Stephen R. Leone
Professor Holger Müller

Spring 2014

Abstract

Studies of Heterogeneously Catalyzed Liquid-Phase Alcohol Oxidation on Platinum by Sum-frequency Generation Vibrational Spectroscopy and Reaction Rate Measurements

by

Christopher Mark Thompson
Doctor of Philosophy in Chemistry
University of California, Berkeley
Professor Gabor A. Somorjai, Chair

Sum-frequency generation (SFG) vibrational spectroscopy has been used to study the interfacial environment in heterogeneously catalyzed alcohol oxidation on platinum catalysts in the liquid phase. In this work, theoretical concepts relevant to studying the metal liquid interface with non-linear spectroscopy are discussed, and the design of a home-built flow reactor cell with *in situ* SFG capabilities is described. SFG data is correlated with reaction rate measurements in liquid-phase isopropanol and ethanol oxidation in order to deduce the effect of the surface environment on the catalyst activity and to elucidate the evolution of the surface throughout the course of the reaction. In conditions of aqueous oxidation of ethanol and isopropanol to acetaldehyde and acetone, respectively, SFG results show that water and alcohol competitively populate the first molecular layer. The reaction rate of isopropanol shows an enhancement in the concentration regime where both water and isopropanol are present in the interfacial region. Water is thus implicated in the reaction as a stabilizer of an intermediate or serving as a proton acceptor in a deprotonation step. Similar results are seen for ethanol oxidation, but the role of water appears to be different in ethanol oxidation. Non-resonant SFG is used as a probe for oxygen adsorption on the platinum surface, and it is seen that the surface is covered in oxygen during the oxidation reaction. A kinetic model is proposed where the build-up of oxygen on the catalyst surface is prevented by its reaction with surface hydrogen. A key part of the model is its inclusion of a mechanism for positive feedback through a proposed step involving hydrogen abstraction by an adsorbed oxygen species. A synthetic method for synthesizing nanoparticles of diameter less than 2 nm is reported using platinum ion reduction in the poly(amidoamine) dendrimer induced by ultra violet light irradiation. The new method is inspired by the need for a reduction method other than sodium borohydride, which we show is not effective in reducing platinum, because platinum ions are strongly stabilized by multidentate interaction with the dendrimer amide groups. The interfacial orientation of isopropanol on platinum nanoparticles under conditions of gas and liquid phase catalysis is investigated using SFG based orientational analysis. The SFG results show that the isopropanol adopts a much different configuration on platinum in the liquid phase compared to the gas phase. Finally, the adsorption of amino acids at the polystyrene/H_2O and SiO_2/H_2O interfaces is shown to have significant effect on the orientation and/or concentration of water at both interfaces. The effect of these molecules on water spans the range from highly disordering to highly ordering and depends on the amino acid identity.

Contents

List of Figures **xiii**

List of Tables **xiv**

Acknowledgements **xv**

1 Introduction **1**

2 Theory of sum-frequency generation vibrational spectroscopy **3**
Introduction . . . 3
Sum-frequency generation history . . . 4
Theory of sum-frequency generation . . . 4
The sum-frequency process and its surface specificity . . . 4
The sum-frequency generation spectroscopy experiment . . . 5
Resonant SFG spectroscopy . . . 6
Non-resonant SFG from surfaces . . . 8
The experimental geometry in sum-frequency generation . . . 8
Orientational analysis with SFG . . . 12
Conclusions . . . 14
References . . . 14

3 Experimental apparatus for sum-frequency generation spectroscopy and reaction rate studies **18**
Introduction . . . 18
Literature review: Studies of the solid/liquid interface with sum-frequency generation 19
In-situ SFG flow reactor for liquid-phase catalysis . . . 20
Flow cell reactor . . . 20
The Teflon reaction cell . . . 21
Aluminum housing block . . . 21
Flow control . . . 22
Oxygen concentration control . . . 23
Product detection by gas chromatography . . . 23
Sum-frequency generation spectroscopy setup . . . 24
Laser and frequency conversion components . . . 24
Sample and detection system . . . 25
Conclusions . . . 28
References . . . 28

4 Isopropanol oxidation on platinum catalysts studied using SFG and reaction rate measurements 31
Introduction . . . 31
Experimental details . . . 32
Catalyst preparation . . . 32
Reaction rate measurements . . . 32
SFG measurements . . . 32
Results and discussion . . . 35
Reaction rates for isopropanol oxidation . . . 35
Sum-frequency generation of aqueous isopropanol mixtures on platinum . . . 37
Conclusions . . . 43
References . . . 43

5 Ethanol oxidation on platinum catalysts studied using SFG and reaction rate measurements 46
Introduction . . . 46
Experimental details . . . 47
Catalyst preparation . . . 47
Reaction rate measurements . . . 47
SFG measurements . . . 48
Results and discussion . . . 49
Kinetic measurements of ethanol oxidation on platinum . . . 49
SFG of ethanol and aqueous ethanol mixtures on platinum . . . 51
Conclusions . . . 55
References . . . 56

6 Investigation of induction behavior in ethanol oxidation using non-resonant SFG to monitor oxygen adsorption on the surface 59
Introduction . . . 59
Experimental details . . . 60
Catalyst preparation . . . 60
Reaction rate measurements . . . 60
SFG measurements . . . 60
Kinetic modelling . . . 61
Results and discussion . . . 61
Reaction rate results . . . 61
Non-resonant SFG results . . . 61
Modelling the induction period in alcohol oxidation . . . 67
Implications for alcohol oxidation . . . 69
Conclusions . . . 72
References . . . 72

7 Study of the platinum-poly(amidoamine) dendrimer system and formulation of an ultraviolet light induced synthesis 74
Introduction . . . 74

Experimental details . . . 75
Particle synthesis . . . 75
Spectroscopic characterization . . . 76
Transmission electron microscopy . . . 76
Results and discussion . . . 76
UV-Vis monitoring of the complexation and reduction of metal ions on G4OH 76
Characterization of G4OH, PtG4OH, RhG4OH samples by resonance Raman spectroscopy: Identification of the metal complexation site . . . 77
Temperature programmed FTIR of the PtG4OH and RhG4OH systems . . . 80
Effects of ultraviolet light on the dendrimer and metal-dendrimer systems . . 84
UV induced platinum reduction for the formation of Pt nanoparticles in the dendrimer template . . . 88
UV-Vis spectroscopic monitoring of particle growth . . . 88
Conclusions . . . 93
References . . . 93

8 Comparison of isopropanol oxidation on platinum nanoparticles in the gas and liquid phases: Kinetics and sum-frequency generation spectroscopy 96
Introduction . . . 96
Experimental details . . . 97
Synthesis of Pt nanoparticles with various sizes . . . 97
Catalyst preparation . . . 98
Catalytic measurements . . . 98
SFG measurements . . . 98
Results and Discussion . . . 99
Nanoparticle synthesis . . . 99
Liquid phase isopropanol oxidation kinetics . . . 99
Gas phase isopropanol oxidation . . . 102
Sum-frequency generation of isopropanol on nanoparticles in the liquid and gas phases . . . 104
Conclusions . . . 107
References . . . 107

9 An SFG study of interfacial amino acids at the hydrophilic SiO_2 and hydrophobic deuterated polystyrene surfaces 110
Introduction . . . 110
Experimental details . . . 110
SFG measurements . . . 110
Quartz crystal microbalance measurements . . . 111
SFG sample preparation . . . 111
Results and discussion . . . 111
SFG spectra . . . 111
SFG of the hydrophobic deuterated polystyrene interface . . . 112
SFG data at the hydrophilic SiO_2 interface . . . 119
Conclusions . . . 126

References 126

List of Figures

2.1 A diagram of the SFG from the perspective of the process as sequential IR absorption and anti-Stokes scattering events. Within the electronic potential, vibrational energy levels exist, which are represented by the horizontal lines labeled "v=0", "v=1", etc. An IR photon (red) can excite a vibrational mode to the v=1 level and a second photon (green) can be inelastically scattered. The energy from the vibrational mode is transfered to the second photon producing a photon (blue) with the energy, $E_{SFG} = E_{IR} + E_{Vis}$. 6

2.2 Experimental geometries for SFG experiments. In transmission mode, the SFG in the transmitted direction is detected. In reflection modes the reflected SFG is detected. The distinction between internal and external reflection is in the indices of refraction of the materials on either side of the interface. . . 9

2.3 The real part of the local field factors for the quartz/water interface (n_{quartz} = 1.46, n_{water} = 1.33, $n_{interface}$ = 1.33) as a function of the incident angle using the thin layer model. The L here are most representative of those for the visible and SFG pulse in SFG experiments. 11

2.4 The real part of the local field factors calculated for the quartz/liquid interface. The three plots show the dependence of the L on the index of refraction of the liquid for incident angles 30°, 45° and 70°. (n_{quartz} = 1.46, $n_{interface} = n_{liquid}$). At 70° total internal reflection conditions are reached at $n_2 \sim 1.37$. 11

2.5 The magnitude of $\chi^{(2)}_{xxz}$,$\chi^{(2)}_{xzx}$,$\chi^{(2)}_{zxx}$ and $\chi^{(2)}_{zzz}$ of a methyl symmetric stretch mode as a function of its tilt angle with respect to the surface normal. It is worth noting that the xzx and zxx components of $\chi^{(2)}$ are equal for the methyl group and their contributions to the overall SFG intensity become distinct only in the difference in the z and x components of the electric field strength and the Fresnel factor difference. 13

2.6 A graphical depiction of the effect of parameter d. Top left: graph of the distributions of the tilt angle around the average for d = 0, d= 0.1 radians and d = 0.5 radians. Top Right: the amplitude of $\chi^{(2)}_{zzz}$ for the methyl stretching transition with varying d values. Notice that as the system becomes more isotropic (as d increases) the value of χ tends toward a constant. 14

3.1 Schematic of the thin-layer analysis mode and the internal reflection mode for SFG of the solid-liquid interface. 19

3.2 Schematic of the setup for integrated SFG and reaction studies. 21

3.3 The design of the Teflon flow cell used for in situ SFG spectroscopy and reaction rate measurements. Units are in inches. 22

3.4 Side view of the aluminum block with integrated magnetic stirring. 22

3.5 Example of a calibration curve for the liquid-vapor exchange system. The signal of acetone was integrated to obtain the area in units of mV·s. The calibration proved to be highly linear over the range of interest. 24
3.6 Diagram of the non-linear system for conversion of the Nd:YAG output to visible (532 nm) and tunable infrared (2700-4000 cm^{-1}). 25
3.7 The angles of incidence for visible and IR pulses on the prism used in SFG experiments. The visible light is incident at 62° to the normal, while the IR pulse is incident at 45°. The direction of the SFG is determined by the conservation of momentum, and it exits the prism at an angle slightly lower angle than the visible, allowing for the spatial separation of the two. 26
3.8 The calculated Fresnel factors for (left) the quartz/platinum/water system and (right) the quartz/platinum/isopropanol system. L_1 is the Fresnel factor for the quartz/platinum interface and L_2 the factor for the platinum/liquid interface. 27
3.9 Left: Schematic of the catalyst used for SFG and reaction studies coupled with a CaF_2 prism using the custom index matching gel. A 2 nm adhesion layer is evaporated onto a glass slide, followed by 5 nm of platinum metal. The glass slide is index matched to a CaF_2 prism using a homemade index matching gel. Right: Molecular structure of the components of the index matching gel. 27
3.10 Reference spectra of gold (blue) deposited directly on to a SiO_2 prism, and (red) deposited onto a glass slide and then index matched to a CaF_2 prism with the home-made index matching gel. 28

4.1 HR-TEM image of 5 nm electron beam deposited platinum on an ultra-thin silicon substrate. It is expected that platinum deposited on quartz forms islands similar to those imaged. 33
4.2 Oxygen solubility in isopropanol/water mixtures from the work by Tokunaga et al. (squares). Polynomial fit used for the calculation of solubilities at intermediate concentration is shown (solid line). 34
4.3 Oxygen concentration dependence of acetone production for increasing alcohol concentrations. The legend above the graph gives the mole fraction of alcohol used. 36
4.4 Maximum rates achieved in the oxygen-independent range for aqueous alcohol mixtures. These rates represent the rate limiting step on the surface. 36
4.5 SFG spectra of pure isopropanol at the liquid/platinum interface. Fit is shown in red. The modes assigned are the CH_3 symmetric stretch (2863 cm^{-1}), CH stretch (2921 cm^{-1}), CH_3 fermi resonance (2955 cm^{-1}) and CH_3 asymmetric stretch (2981 cm $^{-1}$). 38
4.6 Spectra of H_2O and D_2O. The spectrum of D_2O is the background from the platinum metal, while two dips from the OH stretching modes are present in the H_2O spectrum. 39
4.7 SFG spectra of the interfacial layer at varying alcohol concentration with mole fraction of isopropanol varying from 0 to 1. Thick lines are the results of the fitting procedures, which were done separately in the OH region and CH region. 40

4.8 Oscillator strengths (A_q) determined for peaks of isopropanol and H_2O. The peaks in the SFG spectra were fit to equation 4.3, using four peaks for the CH region and two for the OH region. Each colored line corresponds to the vibrational mode whose center frequency (ω_0) is printed in the same color. The spectra suggest that isopropanol reaches saturation at the surface above 0.23 mole fraction and water is completely excluded from the surface. 42

5.1 Oxygen solubility in ethanol/water mixtures and the fit used to calculate O_2 solubility in this work. 48
5.2 Oxygen concentration dependence of acetaldehyde production for increasing alcohol concentrations. The legend gives the mole fraction of alcohol used. . 50
5.3 Kinetic reaction rate for ethanol oxidation for ethanol concentrations of 0, 0.021, 0.066, 0.177 and 1.0. The maximum rate observed with respect to oxygen concentration corresponds to the true kinetic rate. 50
5.4 SFG spectra of the platinum/H_2 and platinum/ethanol interfaces in the gas phase. The ethanol spectrum shows the resonances assigned to the $CH_{3,fr}$, CH_2 symmetric and CH_3 asymmetric modes. 51
5.5 Spectrum and overlaid fit of pure ethanol on platinum. The resonant features can be assigned to the CH stretching modes of ethanol. 52
5.6 SFG spectra of the platinum/liquid interface for increasing concentrations of ethanol in water. The concentrations of ethanol are $x_{EtOH} = 0$, 0.02, 0.25, 0.55 and 1. Fits are shown in black. 54
5.7 Oscillator strengths for the CH_3 group as determined by spectral fitting for mole fractions of ethanol 0, 0.02, 0.25, 0.55, and 1.0. The sign of the oscillator strength is indicative of the phase of the transition. 55

6.1 Reaction rates for ethanol oxidation to acetaldehyde as measured in the flow mode. The induction period exists in the first 60 minutes of reaction, followed by an increase in the acetaldehyde production rate. Conditions: 217 mM ethanol in water, 160 μM O_2, 30 °C. 62
6.2 The induction time as a function of oxygen concentration in the solution for mixtures of ethanol in water. Arrows point to the experiments where the surface was precovered with oxygen to eliminate the induction period. This was done by exposing the catalyst to gaseous or aqueous oxygen. 63
6.3 Activity of 20 nm thick platinum catalyst showing the induction period for the thick film and ruling out significant effect of the titania underlayer . Conditions: 217 mM ethanol in water, 62 μM O_2, 30°C. 64
6.4 The SFG spectrum during the induction period and after the onset of activity. The figure on the left shows the average SFG spectra before and after activity onset. The average of the non-resonant background between 2800 $^{-1}$ and 3600 cm^{-1} as a function of time is shown on the right. Conditions: 217 mM ethanol in water, 30°C. 65

6.5 Left: Non-resonant SFG spectra of platinum under conditions of H_2/H_2O, O_2/H_2O and O_2/217 mM ethanol in H_2O. Right: The averaged signal for the SFG spectra under aforementioned conditions, showing the abrupt decrease upon adsorption of oxygen on surface. 66
6.6 The local field factor, L_{zz} as a function of $n_{interface}$ calculated using equation 6.3 for the platinum liquid interface in the systems of platinum/water calculated for $\lambda = 532$ nm. An angle of 62° was used for the incident angle. . 67
6.7 Left: Non-resonant SFG spectra of platinum under conditions of H_2/H_2O, H_2/Ethanol, N_2/Ethanol, O_2/Ethanol, and O_2/H_2O. Right: The averaged signal for the SFG spectra under aforementioned conditions. Apparently neither water nor ethanol affects the non-resonant signal, but exposure to oxygen immediately causes the decrease in the signal similar to what is seen under reaction conditions. 68
6.8 Top: Relative coverages (in monolayers) of surface species on platinum catalyst as a function of time during the reaction. The induction period consists of the consumption of surface hydrogen, limited by the slow desorption of alcohol from the surface. The fast increase in oxygen species at the end of the induction period is accompanied by a decrease in ethoxy coverage and an increase in the adsorbed product. The rate directly follows the coverage of the adsorbed product. Bottom: the reaction rate (s^{-1}) as a function of time. 70
6.9 Top: the reaction rates as of acetaldehyde production as a function of time for varying oxygen concentrations. The induction period shortens with increased alcohol concentration. Also apparent is the increased rate of oxidation with oxygen concentration. Bottom Left: The induction period length as a function of oxygen concentration. The black dots are the experimental data and the blue line represents the results of the model. Bottom Right: The reaction rate as a function of oxygen concentration. Rate constants used for this figure were $k_a = 1 \times 10^6$;$k_{-a} = 25$;$k_b = 0.35$;$k_{-b} = 5 \times 10^{-4}$; $k_c = k_d = 25$; $k_e = 5 \times 10^{-3}$; $k_f = 0.005$; $k_g = 0.5$; $k_h = 0.1$; $k_i = k_j = 50$. 71

7.1 (a) UV-vis spectra of PtG4OH (1) Absorption spectrum in water solution after complexation. The background corrected spectrum is traced in dots. (2) Absorption spectrum of dry sample (on quartz window) after reduction by $NaBH_4$ (3) Diffuse reflectance spectrum of dry sample after reduction by $NaBH_4$ (b) Comparison of UV absorption spectra of PtG4OH, RhG4OH, and pure G4OH in H_2O. (c) Absorption spectra of PtG4OH (1) before reduction and (2) after reduction by $NaBH_4$. (Inset of c) Background corrected and deconvoluted UV spectrum of reduced PtG4OH. 78

7.2 UV-vis diffuse-reflectance spectra of PtG4OH/Al. (a1) Spectrum of initial PtG4OH/Al and (a2) after reduction at 150 °C for 60 min in flow H_2/Ar. (b1) Background corrected spectra of initial PtG4OH/Al and (b2) spectrum of PtG4OH/Al after reduction at 150 °C for 60 min in flow H_2/Ar. (c) Time dependence of the charge-transfer band N $\rightarrow$ Pt^{2+} during reduction of PtG4OH in H_2/Ar flow at 150 °C: (c-a) initial, (c-b) 30 min and (c-c) 90 min. (Inset of c) The deconvoluted CT band after reduction for 90 min with three components at 266, 302 and 342 nm. 79
7.3 (a) UV-Raman spectra of systems dried on aluminum foil. (1) Pure G4OH, (2) PtG4OH , and (3) RhG4OH(3). (b)UV-vis spectra of PtG4OH and RhG4OH. (c) Raman spectra of PtG6OH in H_2O (1) after the "complexation" stage and (2) after reduction by BH_4^- 81
7.4 Scheme of the coordination of platinum to the G4OH dendrimer as proposed in this work. 82
7.5 (a) FTIR-ATR spectra of G4OH, PtG4OH, and RhG4OH. Drop cast films on Ge prism, s-polarization. (b) Comparison of the FTIR-DRIFT spectra for G4OH heated in O_2 flow at 40 and 270 °C. Intensity is normalized to N-H stretch at 3296 cm^{-1}. (c) Deconvolution of the CH stretching bands (background corrected in panel b) at 40 °C. (d) Deconvolution of the CH stretching bands at 270 °C. 83
7.6 The likely products of dendrimer dehydrogenation following hydrogen abstraction at the amide-neighboring methylene group. 83
7.7 (a) FTIR spectra of PtG4OH heated in a flow of oxygen (2.5 °C/min) at three temperatures: RT-30, 230, and 350 °C. (b) Absorption bands amI and amII of G4OH (black) and PtG4OH (red) upon heating in H_2 at 30 and 200 °C. . 85
7.8 FTIR-DRIFT spectra of PtG4OH and RhG4OH heated in a flow of O_2 (2.5 °C/min.) (a) Three-dimensional spectra of PtG4OH. (b) The change in intensities for characteristic bands: N-H (♦), C-H (•), and amide I + amide II (▲).(c) Three-dimensional spectra of RhG4OH. (d) The normalized intensities for characteristic bands: N-H, C-H, and amide I + amide II. 86
7.9 Time-dependent FTIR spectra of (a) PtG4OH irradiated in O_2 environment. (b) PtG4OH irradiated in H_2 environment. (c) RhG4OH irradiated in hydrogen flow for 0, 180, 1200 min and (d) RhG4OH irradiated in argon flow for 0, 180, 1200 min. 87
7.10 UV-Vis spectra of samples with Pt:G4OH ratios of 10 – 40 and their evolution with irradiation. 89
7.11 Size distributions of platinum nanoparticles synthesized using UV-induced synthesis in the PAMAM dendrimer for Pt:G4OH ratios of 10:1 to 60:1. . . . 90
7.12 Ultrahigh resolution TEM images of a large particle whose shape and crystallinity are constant over time. 91
7.13 Ultrahigh resolution TEM images showing the mesocrystalline Pt particle transitioning through various crystalline (0 s, 20 s) and non-crystallne states. 92
7.14 Ultrahigh resolution TEM images showing a very small particle fluidly moving between disordered structures. The scale bar in the top left image is 2 nm. . 93

8.1 TEM images of synthesized Pt nanoparticles with average sizes of (a) 2 nm synthesized by reduction in ethylene glycol with NaOH, (b) 4 nm synthesized by reduction in ethylene glycol without NaOH, (c) 6 nm synthesized from Pt(II) acetylacetonate and (d) 8 nm also synthesized from Pt(II) acetylacetonate. 100
8.2 Liquid-phase IPA oxidation reaction. (a) TOF in pure IPA catalyzed by Pt nanoparticles with various sizes at 60 °C. (b) Reaction conversion in pure IPA and IPA diluted with various solvents, catalyzed by 4 nm Pt nanoparticles at 60 °C. (c) Comparison of size-dependent TOF in pure IPA and IPA diluted with water and heptane at 60 °C. (d) Comparison of reaction activation energy in pure IPA and IPA diluted with water and heptane, catalyzed by Pt nanoparticles with various sizes at 60 °C. 101
8.3 Gas-phase IPA oxidation reaction. (a) Size-dependent TOF in the gas-phase reactions compared to that in the liquid-phase reactions in pure IPA and IPA diluted with heptane. (b) Dependence of catalytic activity on water incorporation in the gas-phase and liquid-phase IPA oxidation reactions catalyzed by 4 nm Pt nanoparticles at 60 °C. (c) Size-dependent reaction activation energy for the gas-phase IPA oxidation reaction compared with that for the liquid-phase reaction in pure IPA. 103
8.4 SFG vibrational spectra of pure IPA obtained on the surface of 4 nm Pt nanoparticles under gas-phase and liquid-phase reaction conditions. The results of the fitting procedure is shown by the blue line. The vertical red lines mark the frequencies of symmetric stretch ($CH_{3,ss}$ 2870 cm^{-1}), CH stretch (2905 cm^{-1}), the Fermi resonance mode ($CH_{3,fr}$ 2940 cm^{-1}), and asymmetric stretch ($CH_{3,as}$ 2970 cm^{-1}) of the isopropyl moiety. 104
8.5 The ratio of intensities of the CH_3 asymmetric stretch mode (2970 cm^{-1}) to the CH_3 symmetric stretch mode (2870 cm^{-1}) for isopropanol using the united atom model. The rotational angle, ϕ, is listed in the legend. The ratios obtained by experiment are given by the thick blue horizontal lines. Left: the ratio using Fresnel factors for the gas phase system. Right: the ratio using Fresnel factors for the liquid system. 106
8.6 Orientation maps showing the orientations of the isopropyl group of IPA which would have a methyl asymmetric/methyl symmetric intensity ratio within 20% of the data obtained by SFG. On the left, the possible range of orientation in the gas phase is colored in blue. On the right, the orientations obtained from the liquid phase data are plotted. 106
8.7 Graphical depictions of the orientation of the isopropyl group of IPA in the gas and liquid phase. The cartoons are plotted to depict orientations from the encircled regions in Figure 8.6. 107

9.1 SFG spectrum of d_8PS/PBS interface before (black squares) and after (red circles) addition of phenylalanine (5 mg/mL). The vibrational modes at 2875 and 2939 cm^{-1} are attributed to CH_2 symmetric and a CH combination band/Fermi resonance, respectively. The peak at 2991 cm^{-1} is identified as a CH combination band or a CH_2 asymmetric stretch. Finally, the largest peak at 3049 cm^{-1} is indicative of the aromatic CH $\nu 2$ stretch of the amino acid phenyl side chain. 112
9.2 SFG spectrum of the d_8PS/PBS interface before (black squares) and after (red circles) the addition of leucine (5 mg/mL). The vibrational mode at 2874 cm^{-1} is attributed to either a CH_3 symmetric stretch from the terminal methyl groups or a CH_2 symmetric stretching mode. The larger peak at 2942 cm^{-1} is indicative of a CH_3 Fermi resonance or a CH_2 asymmetric stretch. The vibrational mode fit in the spectrum at 3056 cm^{-1} may be due to a highly perturbed $CH_2(as)$, NH dimer, or NH stretching vibrational mode. 113
9.3 SFG spectrum of the d_8PS/PBS interface before (black squares) and after (red circles) the addition of glycine (100 mg/mL). The vibrational mode at 2873 cm^{-1} is attributed to a CH_2 symmetric stretching mode, and the larger peak at 2939 cm^{-1} is identified as originating from a CH_2 asymmetric stretch. 114
9.4 SFG spectrum of the d_8PS/PBS interface before (black squares) and after (red circles) the addition of lysine (15 mg/mL). The vibrational mode at 2874 cm^{-1} is attributed to a CH_2 symmetric stretch and a larger peak at 2942 cm^{-1} is indicative of a CH_2 asymmetric stretch from the lysine side chain. The dramatic increase in signal upon the addition of l-lysine is attributed to a change in the net orientation of interfacial water as well as possible contributions from NH stretching modes of the acid's terminal amine group or backbone. 115
9.5 SFG spectrum of the d_8PS/PBS interface before (black squares) and after (red circles) the addition of arginine (15 mg/mL). The vibrational mode at 2880 cm^{-1} is attributed to a CH_2 symmetric stretch and a larger peak at 2935 cm^{-1} is indicative of a CH_2 asymmetric stretch. Another peak centered at 2977 cm^{-1} was fit to the spectrum and is attributed to the formation of a cyclic dimer species forming between two neighboring arginine molecules on the hydrophobic surface. The dramatic increase in signal near 3100 cm^{-1} upon the addition of arginine is attributed to change in the net orientation of interfacial water as well as NH stretching modes of the amino acid's terminal guanidino group or backbone. 116
9.6 SFG spectrum of the d_8PS/PBS interface before (black squares) and after (red circles) the addition of cysteine (25 mg/mL). The vibrational mode at 2872 cm^{-1} is attributed to a CH_2 symmetric stretching mode, and the peak at 2935 cm^{-1} is identified as originating from a CH_2 asymmetric stretch. A third CH vibrational mode is observed at 2993 cm^{-1} and is assigned as either a perturbed $CH_{2,as}$ mode, or a combination band of the $CH_{2,ss}$ and CH stretches of solvated cysteine molecules. 117

9.7 SFG spectrum of the d_8PS/PBS interface before (black squares) and after (red circles) the addition of proline (15 mg/mL). The vibrational mode at 2875 cm^{-1} is attributed to a combination of $C_\beta H_2$ (s), $C_\gamma H_2$ (s), and $C_\delta H_2$ (s) modes. The peak at 2934 cm^{-1} is identified as combination mode from $C_\beta H_2$ (s) and $C_\gamma H_2$ (s) vibrations. Finally, the combination mode at 2984 cm^{-1} originates from $C_\beta H_2$ (as) and $C_\gamma H_2$ (as) vibrations. The broad increase of SFG signal in the region 3000-3400 cm^{-1} upon the addition of proline is attributed to change in the net orientation of interfacial water as well as NH stretches of the heterocyclic amino acid. 118
9.8 SFG spectrum of the d_8PS/PBS interface before (black squares) and after (red circles) the addition ofalanine (40 mg/mL). No CH vibrational modes are observed, and the water signal is unperturbed after the adsorption of amino acid. 119
9.9 SFG spectrum of PBS/SiO_2 interface before (black squares) and after (red circles) addition of leucine (5 mg/mL). No hydrocarbon vibrational modes are observed, but an enhancement in the broad spectral features at 3200 and 3400 cm^{-1} occurs upon the addition of leucine. This result suggests that the presence of the hydrophobic amino acid can cause a change in the net orientation of interfacial water at the SiO_2/PBS interface. 120
9.10 SFG spectrum of PBS/SiO_2 interface before (black squares) and after (red circles) addition of arginine (15 mg/mL). No hydrocarbon vibrational modes are observed upon the addition of arginine, but an enhancement and substantial peak broadening occurs in the spectral features at 3200 and 3400 cm^{-1}. This result suggests that the presence of the arginine can cause a change in the net orientation of interfacial water at the SiO_2/PBS interface. 121
9.11 SFG spectrum of PBS/SiO_2 interface before (black squares) and after (red circles) addition of (15 mg/mL). No hydrocarbon vibrational modes are observed upon the addition of arginine. However, similar to the SFG spectrum of l-arginine at the SiO_2/PBS interface, this spectrum shows a significant enhancement and peak broadening occurring in the spectral features at 3200 and 3400 cm^{-1}. This result suggests that the presence of the lysine amino acid molecules causes a change in the net orientation of interfacial water at the SiO_2/PBS interface. 122
9.12 SFG spectrum of the SiO_2/PBS interface before (black squares) and after (red circles) the addition of glycine (100 mg/mL). SFG signals at 3200 and 3400 cm^{-1} are reduced upon addition of the amino acid. 123
9.13 SFG spectrum of the SiO_2/PBS interface before (black squares) and after (red circles) the addition of l-cysteine (25 mg/mL). SFG signals at 3200 and 3400 cm^{-1} are reduced upon addition of the amino acid. 123
9.14 SFG spectrum of the SiO_2/PBS interface before (black squares) and after (red circles) the addition of alanine (40 mg/mL). SFG signal at 3200 and 3400 cm^{-1} are reduced upon addition of the amino acid. 124
9.15 SFG spectrum of PBS/SiO_2 interface before (black squares) and after (red circles) addition of phenylalanine (5 mg/mL). No changes in water signal at 3200 or 3400 cm^{-1} are observed upon the addition of amino acid. 125

9.16 SFG spectrum of the SiO_2/PBS interface before (black squares) and after (red circles) the addition of proline (15 mg/mL). No changes in water signal at 3200 or 3400 cm^{-1} are observed upon the addition of amino acid. 125

List of Tables

5.1 Fitting parameters for pure ethanol on platinum. These values correspond to the red line in Figure 5.5 52

5.2 Fitting parameters for SFG peaks of ethanol/water mixtures (x_{EtOH}= 0, 0.02, 0.25, 0.5, 1.0) on platinum. These values correspond to the spectra in Figure 5.6. Parameters for resonant features varied in the fits were the oscillator strength (A), center frequency (ω_0), the peak width (Γ). The background susceptibility was modeled as a linear function in frequency with parameter for the slope and intercept. These parameters are not shown. 54

7.1 IR spectral assignments for the 4th genereration poly(amidoamine) dendrimer (G4OH) 82

9.1 Adsorbed mass at the aqueous liquid-solid interface determined by QCM . . 111

Acknowledgements

I would like to express my thanks to Prof. Gabor Somorjai, who has provided me the opportunity, the means, and the guidance to complete this project. I am very grateful for his mentorship and insight along the way and also for his strong support of me now, as I move on to my next project.

I am grateful to all the people I have met at Berkeley in my time here. Rob Onorato and George Holinga were my teachers and friends in the lab, to whom I owe special thanks for teaching me to be a successful researcher. I'm also thankful to the many other good friends I've met at Berkeley, all of whom have taught me much. I would especially like to thank Inger Coble, the one Somorjai group member without whom I definitely could not have been successful in my research. In addition, I'd like to thank Prof. Miquel Salmeron, Dr. Lin-Wang Wang and Prof. Paul Weiss for their support.

Every day I see more of my mom and dad in myself. The patience, confidence, ambition and curiosity that brought me here comes from them. I am thankful to them and my sister, Colleen, for their love and encouragement.

I am grateful to have Julia Perriello with me on this road, too. Through her love, wisdom and humor, I've grown so much more in the past five years than I could have on my own, and I'm excited for that to continue in our life together.

This work is funded by the Director, Office of Science, Office of Basic Energy Sciences, Division of Materials Sciences and Engineering, of the U.S. Department of Energy under Contract No. DE-AC02-05CH11231.

Chapter 1

Introduction

Compared to many branches of chemistry, the molecular level study of catalytically active surfaces is young. Only with the invention of ultrahigh vacuum technology in the past half century has it been possible to carry out experiments that yield useful molecular information about the reactive occurrences at a surface. The reason is two-fold: low pressure is necessary to keep a surface clean for an amount of time long enough to perform an experiment, and most atomic scale techniques that are surface specific (x-ray photoelectron spectroscopy, electron energy loss spectroscopy, Auger electron spectroscopy, etc.) cannot be used at ambient pressures, because electrons, which act as chemical probes in these techniques, are easily scattered by molecules. Sum-frequency generation (SFG) vibrational spectroscopy is one technique that *can* provide molecular level information from the surface without the necessity for high vacuum.

Since the advent of SFG as a surface spectroscopic tool it has proved its worth in the studies of surface catalyzed reactions in the gas phase, with numerous reactions in the gas phase having been investigated on a multitude of surfaces. However, *in situ* SFG characterization of catalysis at the solid-liquid interface has yet to be thoroughly pursued despite the broad interest in the use of heterogeneous catalysts in the liquid phase as replacements for homogeneous counterparts. This work describes an attempt to move in that direction, applying SFG to study the solid-liquid interface under conditions of catalytic alcohol oxidation on platinum.

Chapter 2 discusses the background theory of sum-frequency generation. The important characteristics of the spectroscopy, including the origin of its surface specificity, momentum and energy conservation and some experimental considerations are covered.

Chapter 3 discusses the design of a new catalytic reactor system specially built for the liquid phase alcohol oxidations studies with capabilities for *in situ* SFG spectroscopy. The home built system contains many features tailored to this work.

Chapter 4 discusses the partial oxidation of isopropanol to acetone in aqueous conditions as studied using SFG in the aforementioned reaction cell. The SFG spectra obtained across the full range of alcohol concentration in aqueous mixtures were collected and show correlation with the reaction kinetics of isopropanol oxidation to acetone.

Chapter 5 discusses the partial oxidation of ethanol to acetaldehyde under similar conditions as isopropanol. The trends in ethanol oxidation and isopropanol oxidation are compared.

Chapter 6 examines the induction period in ethanol oxidation. A relatively uncommon use of the non-resonant SFG signal is applied to show that the surface of platinum becomes

oxygen covered at the end of the induction period. A kinetic model for the induction period is proposed, and the results of the model are compared with experiment.

Chapter 7 discusses a spectroscopic study of the Pt- and Rh- poly(amidoamine) dendrimer system. A unique stabilization of platinum ions in the dendrimer is identified using UV-vis spectroscopy, resonance Raman spectroscopy and FTIR spectroscopy. A bonding scheme is proposed in which platinum complexation with multiple amide groups keeps it stable toward reduction. Ultraviolet light irradiation is found to be an effective way to release the platinum ions from this coordination environment and form nanoparticles. From this we formulate a new synthetic method for dendrimer-mediated platinum nanoparticle synthesis.

Chapter 8 is a study of the difference between gas and liquid phase alcohol oxidation on platinum nanoparticles. Kinetic studies show that particles possess different catalytic properties in the gas and liquid phase. Sum-frequency generation orientational analysis is applied to show that isopropanol adopts different orientations on the surface in the two systems, and we expect that this different bonding environment changes the activity of the catalyst.

Chapter 9 is an example of the study of another type of molecule at the solid/liquid interface, namely the amino acid. Amino acids serve as model compounds for protein adsorption on materials in the human body. The effect of these molecules' adsorption on the ordering and/or concentration of water at the surface of SiO_2 and d_8-polystyrene is shown to be profound and to depend on the identity of the amino acid.

Chapter 2

Theory of sum-frequency generation vibrational spectroscopy

This chapter discusses the background and theory of sum-frequency generation (SFG) vibrational spectroscopy. SFG allows the vibrational signatures from molecules at an interface to be probed without interference from the bulk. Herein the history and current uses of SFG are discussed, and the theory underlying the process is laid out. The selection rules and characteristics of SFG are introduced, some basic description of SFG experimental considerations are given and the use of SFG to determine the orientation of molecules at the interface is discussed. The topics considered in this chapter are relevant to the studies discussed later in this work.

Introduction

Sum-frequency generation (SFG) vibrational spectroscopy is a tool utilized to give surface-specific information about molecular species at an interface. As a vibrational spectroscopy, SFG yields molecular information similar to that given by Raman scattering spectroscopy and infrared absorption spectroscopy. Based on a second order optical phenomenon, SFG gives information predominantly from a region of broken inversion symmetry[1–4]. The combination of these two properties means that SFG can serve as a probe for chemical bonding in specifically those molecules that are located at an interface. Moreover, in contrast with many other surface characterization tools, SFG does not require vacuum conditions, and it can be used *in situ* in almost any system, which makes it an extremely powerful tool for studying the surface of metal catalysts.

The study of clean surfaces was originally made possible by the development of modern vacuum technology, which allowed researchers to conduct experiments at pressures as low as 10^{-10} Torr (10^{-13} Pa)[5]. At these pressures the quantity of gas molecules impinging on a surface is less than 1 monolayer ($\sim 10^{15}$ molecules) per hour - a rate slow enough to allow for experiments on a clean surface to be performed. The conditions required for maintaining a clean surface conveniently coincide with the conditions required for atomic-level surface specific (mostly electron-based) techniques, including X-ray photoelectron spectroscopy (XPS), Auger electron spectroscopy (AES), and low-energy electron diffraction (LEED). However, it has since become quite clear with the invention of "ambient pressure" techniques that the lessons learned from vacuum studies cannot always be extrapolated to real world conditions. At this time, while instrumentation exists to study surfaces under limited high pressure conditions in the gas phase, the molecular level study of interfaces at atmospheric pressure or in condensed systems remains a frontier in science. Sum-frequency generation vibrational

spectroscopy remains a very unique tool in the repertoire of surface scientists to directly probe the interface of two condensed media without interference from the bulk.

Sum-frequency generation history

The application of SFG as a surface-specific spectroscopy was pioneered by Ron Shen at UC Berkeley in the 1980s[6–9]. Some of the first works investigating the vibrations of surface species were carried out on the silica/water and water/air interface. Since then, numerous studies have been carried out at the gas/solid, gas/liquid, liquid/liquid, solid/solid and solid/liquid interfaces. A fast glance at the SFG literature would include the study of surface species at electrochemical electrode and catalyst surfaces[10,11], the organization of small molecules at interfaces[12–15], self-assembly of alkanethiolate monolayers on metals, polymer interfaces[16],the organization of water at various solid and liquid surfaces, biomolecule adsorption[17–19], and molecules at the surface of atmospheric aerosols[20,21].

The use of SFG to investigate the surface of catalytic metals dates back to 1996 when members of the Somorjai group used the technique to identify the surface species of olefin hydrogenation on platinum[22]. Since then Somorjai and others have correlated SFG spectra with reaction data to explain trends in catalytic activity and selectivity - first on single crystal model catalysts, then on nanoparticles. These include identification of the intermediates of gas-phase platinum catalyzed hydrogenation of ethylene, propylene, pyridine and benzene[22–26] and the hydrogenation of furan, 2-methylfuran and 2,5-dimethylfuran[27,28].

SFG studies of reactive surfaces in the liquid phase have also been performed - mostly on electrochemical electrodes. These include the study of carbon monoxide on platinum electrodes[29] and alcohol electrooxidation on platinum single crystals and carbon supported platinum[30–33].

These studies are good indicators that SFG is a useful tool for studying the catalytic interface and make its application in liquid phase heterogeneous catalysis studies attractive. The use of nanoparticle catalysts in the liquid phase catalyzed reactions has been the subject of study for some time now[34–36] and is attractive for the application of heterogeneous catalysts to the synthesis of finer chemicals such as pharmaceuticals, since these molecules are too large and complex to be put into the gas phase without destroying their properties. While SFG has served as a complement to a number of physical chemistry techniques that were useful for catalytic characterization in the gas phase, the introduction of a second condensed phase at the interface rules out most other techniques, and SFG remains as one of very few ways to specifically probe the surface species *in situ*[37–41].

Theory of sum-frequency generation

The sum-frequency process and its surface specificity

The interaction of an electromagnetic field with matter induces a polarization in the material that can be described as a power series in the field strength, E;

$$P = P^{(0)} + \epsilon_0(\chi^{(1)}E + \chi^{(2)}E^2 + \chi^{(3)}E^3...) \tag{2.1}$$

where P represents the polarization in the material, $P^{(0)}$ is the permanent polarization, ϵ_0 the permittivity of free space, and the $\chi^{(n)}$ represent the nth order optical susceptibility. The oscillating polarization of the material acts as a source of an emitted electromagnetic wave. Linear phenomena, such as absorption, are described by the first order term in equation 2.1.

It is apparent from equation 2.1 that the higher order effects rely on a high field strength, which explains why under ordinary conditions, they are not observed. When a single field frequency is present, the second order non-linear susceptibility, $\chi^{(2)}$, describes second harmonic generation (SHG) where the polarization oscillates at a frequency twice that of the incident field. When two frequencies are present $\chi^{(2)}$ encapsulates multiple ways in which the fields are coupled, which can result in a third field at the sum of the two incident frequencies – called sum-frequency generation (SFG) - or the difference – called difference-frequency generation. A typical value for $\chi^{(2)}$ in resonance is 10^{-14} esu[7].

The intensity of SFG signal, I_{SFG}, from a sample surface can be written in terms of the intensities of the incident light, I_1 and I_2, the second order non-linear susceptibility, and the local field factors, L, which depend on the experimental geometry and the indices of refraction of the materials under investigation. In equation 2.2 the subscripts, i, j and k represent the polarizations (x, y or z) of the fields.

$$I_{SFG} = |L_{ii}L_{jj}L_{kk}\chi^{(2)}_{ijk}|^2 I_1 I_2 \tag{2.2}$$

Because $\chi^{(2)}$ involves the coupling of three fields in a 3-dimensional frame, it must be represented by a third rank tensor with 27 elements. Each element, $\chi^{(2)}_{ijk}$, is the susceptibility for a field polarization combination in order of descending energy (as will be discussed later, for SFG, which is usually performed with one visible incident field and one infrared, this means SFG, visible, IR). The inherent symmetry of $\chi^{(2)}$ is such that under inversion its sign must change. This can be understood by considering that an inversion operation is equivalent to the flipping of all three polarizations in equation 2.2. This is is equivalent to multiplying the term by $(-1)^3$. Thus an inversion process should result in the negation of $\chi^{(2)}$. Moreover, the symmetry of the material should be reflected its optical properties, so in environmentsthat possess inversion symmetry – such as in bulk solid materials with common metal crystal lattices - $\chi^{(2)}$ must be symmetric. The only value of $\chi^{(2)}$ that satisfies both of these conditions is zero, so the susceptibility is zero in centrosymmeric media. Wherever centrosymmetry is broken, e.g. at an interface, this rule no longer holds, and $\chi^{(2)}$ may be non-zero.

In the case of an interface possessing C_∞ symmetry, seven of the 27 tensor elements are non-zero, and only four are unique. These are

$$\chi^{(2)}_{zzz},\ \chi^{(2)}_{xxz} = \chi^{(2)}_{yyz},\ \chi^{(2)}_{xzx} = \chi^{(2)}_{yzy},\ and\ \chi^{(2)}_{zxx} = \chi^{(2)}_{zyy} \tag{2.3}$$

The sum-frequency generation spectroscopy experiment

In a typical SFG experiment, two laser pulses are overlapped spatially and temporally at a surface of interest. For vibrational spectroscopy one pulse must be in the mid-IR region, between 800 and 4000 cm^{-1} and this pulse must be tunable (in the case of narrowband spectroscopy) or broadband. The other pulse is held fixed usually in the visible range of the

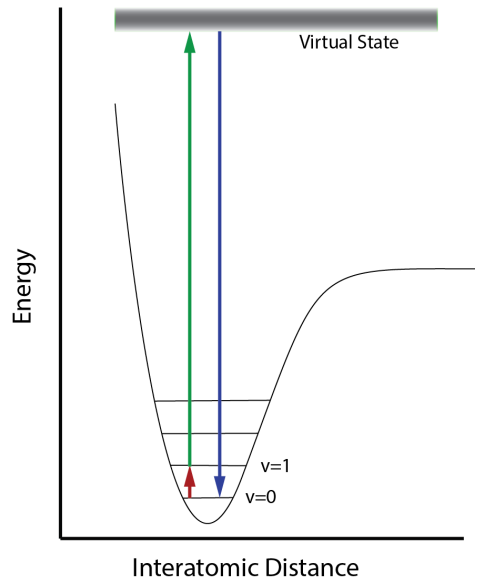

Figure 2.1: A diagram of the SFG from the perspective of the process as sequential IR absorption and anti-Stokes scattering events. Within the electronic potential, vibrational energy levels exist, which are represented by the horizontal lines labeled "v=0", "v=1", etc. An IR photon (red) can excite a vibrational mode to the v=1 level and a second photon (green) can be inelastically scattered. The energy from the vibrational mode is transfered to the second photon producing a photon (blue) with the energy, $E_{SFG} = E_{IR} + E_{Vis}$.

spectrum, which serves to "up-convert" the IR pulse to a frequency which can be detected most sensitively. This pulse must always be narrow ($\Delta\lambda$ <1 nm), and its frequency is usually that which can be generated easiest from the pump laser, either 532 nm by second harmonic generation of a Nd:YAG laser output or 800 nm for a Ti:Sapphire laser.

Resonant SFG spectroscopy

One picture of resonant SFG is that of a combination of IR absorption and anti-Stokes Raman scattering (Figure 2.1). In molecular systems, $\chi^{(2)}$ can be broken down to a sum of the contributions of all the vibrational modes, q, in the system.

$$\chi^{(2)}_{ijk}(\omega) = \sum \frac{M_{ij,q} A_{k,q} \sqrt{\Gamma_q}}{(\omega - \omega_{0,q}) + i\Gamma_q} f_q(\theta, \phi, \psi) \tag{2.4}$$

where ω is the IR frequency used, M_{ij} is the Raman polarizabilty matrix, A_k is the IR transition dipole moment, $\omega_{0,q}$ is the center frequency of a vibrational resonance of mode and Γ_q is the transition width. f_q is the orientational parameter arising from the coherent nature of SFG which will be discussed later. One major selection rule of SFG is immediately discernable from equation 2.4; i.e. the requirement for a mode to be both Raman and IR active in order for SFG signal to be generated. IR absorption has the selection shown in equation 2.5 and Raman scattering that shown in equation 2.6.

$$A = \frac{d\mu}{dq} \neq 0 \tag{2.5}$$

$$M = \frac{d\alpha}{dq} \neq 0 \tag{2.6}$$

From the 'rule of mutual exclusion' of vibrational spectroscopy, which states that the vibrations of any centrosymmetric molecule cannot be both IR and Raman active, it is evident that centrosymmetric molecules should not be SFG active. One common manifestation of this rule is in the spectra of self-assembled alkanethiolate monolayers. In a highly ordered state, the spectra of these monolayers exhibit no signal from the methylene groups of the alkane chain, because the (CH_2-CH_2) group possesses inversion symmetry.

Unlike IR absorption and Raman scattering, SFG is coherent. This means that the phase of the emitted sum-frequency field is preserved, and the signals from individual molecules can constructively or destructively interfere. It can be said that when a functional group of two molecules (or two moieties of the same molecule) are oriented exactly opposite one another, the phase of the signals will be offset by π and will destructively interfere. From this arises the orientational parameter in equation 2.4, which is a function of the angular orientation of each individual mode in the ensemble. When the modes in the system are perfectly aligned, the overall measured signal is maximum. When they are completely disordered, the overall measured signal will be zero. The absence of SFG signal from bulk liquids comes from this consideration.

During an SFG process, no energy or momentum is transferred to the interacting medium. Energy is conserved according to the equation,

$$\omega_{SFG} = \omega_{vis} + \omega_{IR} \tag{2.7}$$

The photons in the SFG process also obey conservation of momentum, which is known as phase matching conditions, according to

$$\mathbf{k}_{SFG} = \mathbf{k}_{vis} + \mathbf{k}_{IR} \tag{2.8}$$

In equation 2.8 the $\mathbf{k}$ represent the momentum vectors of the light (momentum is conserved separately in each direction). This has the effect of making the SFG signal directional. The angle of exit for co-planar co-propagating incident beams can be easily calculated using equation 2.9, where θ is the angle relative to a plane perpendicular to the plane formed by the IR and visible beams.

$$\frac{n_{SFG}}{\lambda_{SFG}} sin(\theta_{SFG}) = \frac{n_{vis}}{\lambda_{vis}} sin(\theta_{vis}) + \frac{n_{IR}}{\lambda_{IR}} sin(\theta_{IR}) \tag{2.9}$$

This equation is relevant for the forward propagating system, but in the case of probing a surface in internal reflection mode, the angle must be reflected. This consideration is of practical importance in aligning the detector in the experiment.

Non-resonant SFG from surfaces

While molecules at an interface can generate resonant features in the SFG spectrum, certain materials have a non-linear susceptibility that is non-resonant. This makes it necessary to consider even those materials without resonant vibrational modes in interpreting the spectrum. Dielectric materials such as polymers are considered to have zero non-resonant susceptibility, but metals and semiconductors with electron motion allowing for stronger interaction with the incident fields can have a strong susceptibility. Gold is the best known non-resonant metal, and its high non-resonant signal can easily overwhelm the signal of molecules near its surface. It is a somewhat exceptional case though, because the cause of its high non-resonant signal is a plasmon resonance around 500 nm which is close to the wavelength of the visible beam used in many SFG experiments. Silver and platinum have also been shown to have non-resonant signals, but in most experiments their susceptibility is far lower than that of gold, because they lack the plasmon resonance in the relevant wavelength region. In the case of non-resonant backgrounds, one major consideration is that the non-resonant signal of metals may be out of phase with the resonant signals of molecules at the surface. This can cause distortions of the peak shapes which may be minor – as in the case of platinum – or major - as in the case of gold.

The experimental geometry in sum-frequency generation

A number of experimental geometries exist for sum-frequency generation vibrational spectroscopy. Geometric parameters, such as beam polarization, incident angle, and probing mode can be selected to maximize signal, minimize spectral complexity, and reduce experimental artifacts. It was mentioned previously that the qualitative nature of the non-linear susceptibility is dependent on the electric field orientation. For experimental purposes, where the beams are directed at the surface of interest at an angle off normal, xyz coordinates are less relevant and it is more practical to choose polarizations parallel or perpendicular to the surface, referred to as s and p polarized, respectively. Each polarization combination in the s/p notation can be expressed in terms of the xyz notation. The only non-zero susceptibility elements for these polarization combinations in a system of C_N symmetry are χ_{ppp} ,χ_{ssp},χ_{pss} and χ_{sps}, and these can be expressed as a combination of the susceptibilities in the xyz coordinates as follows:

$$\begin{aligned}\chi_{ppp} = &-cos\theta_{SFG}cos\theta_{vis}sin\theta_{IR}\chi_{xxz} - cos\theta_{SFG}sin\theta_{vis}cos\theta_{IR}\chi_{xzx} \\ &+sin\theta_{SFG}cos\theta_{vis}cos\theta_{IR}\chi_{zxx} + sin\theta_{SFG}sin\theta_{vis}sin\theta_{IR}\chi_{zzz}\end{aligned} \tag{2.10}$$

$$\chi_{pss} = -sin\theta_{SFG}\chi_{zyy} \tag{2.11}$$

$$\chi_{sps} = -sin\theta_{vis}\chi_{yzy} \tag{2.12}$$

$$\chi_{ssp} = -sin\theta_{IR}\chi_{yyz} \tag{2.13}$$

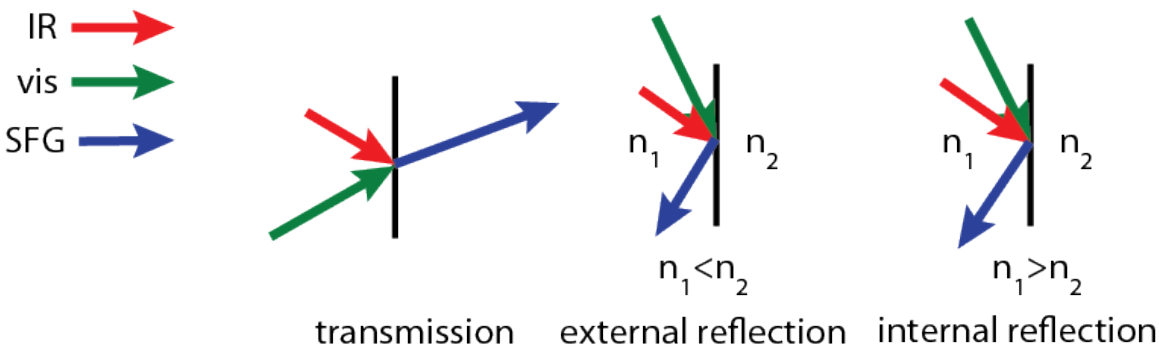

Figure 2.2: Experimental geometries for SFG experiments. In transmission mode, the SFG in the transmitted direction is detected. In reflection modes the reflected SFG is detected. The distinction between internal and external reflection is in the indices of refraction of the materials on either side of the interface.

where the θ are the angles of incidence (for IR and visible) or reflection or refraction (for SFG) relative to the surface normal.

Figure 2 illustrates the most commonly used probing geometries in SFG experiments. Of these, the most basic is the transmission mode, in which the SFG transmitted across the interface is collected. In reflection mode, the SFG which is reflected at the interface is collected. The reflection geometry where the beams travel through the medium of lower refractive index is called external reflection mode. This is often used for self-assembled monolayers on gold surfaces, where the low-index medium is non-absorbing in the region of interest or only weakly so. In the case of liquids, which are usually highly absorbing in wide regions of the mid-IR, absorption can be minimized by decreasing the liquid thickness to less than 100 microns. However, this mode functions poorly for simultaneous catalytic studies, because mass diffusion can become an issue. To eliminate diffusion constraints with stirring, it is necessary to use the internal reflection mode, where light travels through a medium of high refractive index and low absorptivity. The reflected light is maximized by increasing the difference of refractive indices, but the infrared light does not travel through a liquid. In this way, no artifacts of IR absorption are introduced into the SFG spectra.

In using the internal reflection mode, it is necessary to consider the reflected local field factors, L, because these can vary greatly with certain experimental parameters. The electric field amplitude at the interface is a function not only of the input intensity, but also of the indices of refraction of the media and the angles of incidence of the SFG, visible and IR pulses.

In SFG studies a thin layer model is often used, where light is moving from a material with refractive index, n_1, through a very thin (much less than the wavelength of light) layer at the interface, to a material with index n_2 at the angle to the normal θ_1. In this case, L can be expressed

$$L_{xx} = \frac{2n_1 cos\theta_2}{n_1 cos\theta_2 + n_2 cos\theta_1} \tag{2.14}$$

$$L_{yy} = \frac{2n_1 cos\theta_1}{n_1 cos\theta_1 + n_2 cos\theta_2} \tag{2.15}$$

$$L_{zz} = \frac{2n_1 cos\theta_1}{n_1 cos\theta_2 + n_2 cos\theta_1} \cdot (\frac{n_1}{n_{interface}})^2 \tag{2.16}$$

The subscripts on the L refer to the polarization and θ_2 is the refracted angle, which is obtained by Snell's Law. Including these in equation 2.2 shows that the intensity of SFG will vary if the refractive index is changed or if the angle of incidence is changed. Figure 2.3 shows the dependence of the L on the incident angle, showing clearly that the signal intensity increases dramatically as the incident angle reaches the critical angle, θ_c , defined by equation 2.17.

$$\theta_c = sin^{-1}(\frac{n_1}{n_2}) \tag{2.17}$$

This would suggest that the best experimental geometry is one where all beams are incident at the critical angle. However, in practice this often becomes problematic, for, in scanning SFG systems where the IR pulse is tuned by rotating the crystals used for frequency conversion, the beam path and hence the incident angle, may vary with frequency. It is apparent in Figure 2.3 that near the critical angle the effect of this variation is an extreme change in the signal intensity. It is advantageous in some situations to work off of the critical angle to avoid such an effect.

The angle of incidence can also be chosen in order to minimize the change of local field factor with changes in the index of refraction of the second material. This consideration can come into play in studies of solid/liquid interface when the liquid may be changing over the course of the experiment. Figure 2.4 shows how the local field factors vary with refractive index for three incident angles. Again, the slope is steepest when working near the critical angle.

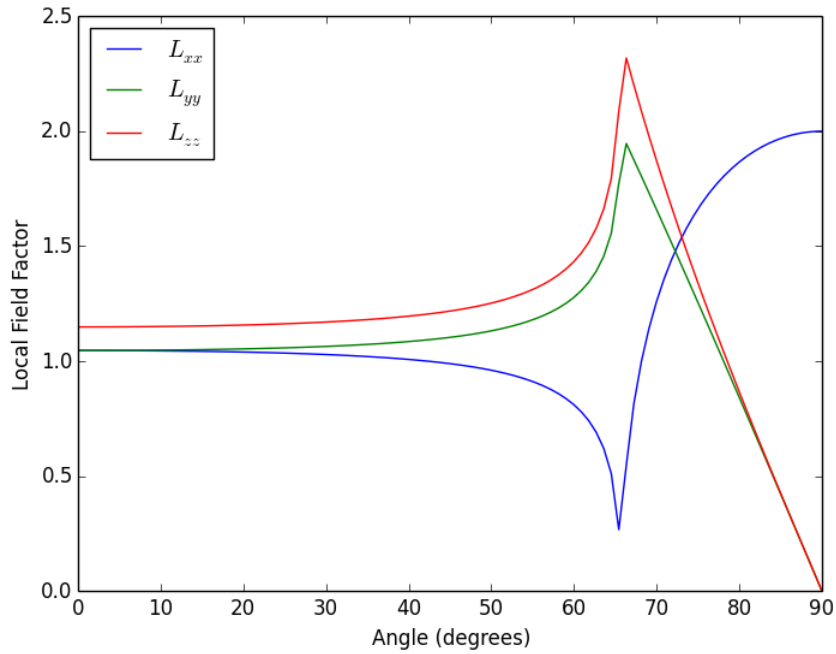

Figure 2.3: The real part of the local field factors for the quartz/water interface (n_{quartz} = 1.46, n_{water} = 1.33, $n_{interface}$ = 1.33) as a function of the incident angle using the thin layer model. The L here are most representative of those for the visible and SFG pulse in SFG experiments.

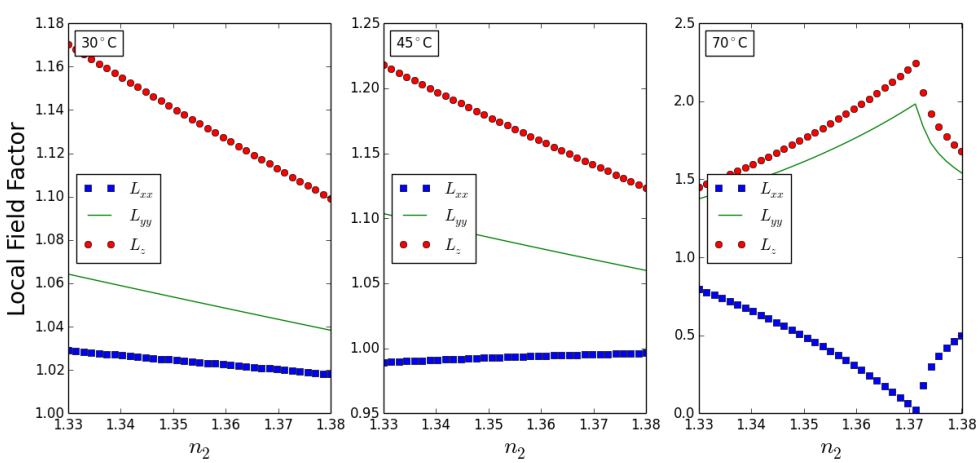

Figure 2.4: The real part of the local field factors calculated for the quartz/liquid interface. The three plots show the dependence of the L on the index of refraction of the liquid for incident angles 30°, 45° and 70°. (n_{quartz} = 1.46, $n_{interface}$ = n_{liquid}). At 70° total internal reflection conditions are reached at $n_2 \sim 1.37$.

Orientational analysis with SFG

The polarized light source used in SFG and its coherent nature give it a unique capability over linear vibrational spectroscopy in that the orientation of molecules can be extracted from SFG spectra. A very thorough examination of orientational analysis has been presented by Wang and co-workers[42]. In the simplest case of a single stretching vibrational mode, the directional nature of the IR transition dipole moment and the Raman polarizability matrix combine to give the amplitude of the molecular hyperpolarizability, β, a strong orientation dependence. This is demonstrated simply using the IR transition dipole moment of a heteronuclear diatomic molecule, μ, which is directed parallel to the bond axis. On a molecular level, infrared light with its electric field oriented perpendicular to μ is incapable of interacting with the stretching mode. As the orientation of the electric field is turned toward the bond axis direction, the intensity of the transition will increase with the component of the electric field which is parallel to μ. The Raman polarizability matrix has two polarization directions, the incident polarization and the measured polarization. β, being the product of these two values, has the directionality of both.

In vibrational spectroscopy single molecular bond vibrations are rarely considered, because diatomic vibrations of similar frequencies will couple to form group modes. Common examples are the symmetric and asymmetric stretches of the CH_2 mode and the CH_3 mode. These groups have their own μ and α.

In order to extract all the unique elements of $\chi^{(2)}$ it is necessary to collect spectra in all four allowed polarizations: *ssp*, *sps*,*pss* and *ppp*. This requirement is evident from equations 2.10 - 2.13. While the measured intensity of the SFG signal is related to the value of $\chi^{(2)}$ in a complicated way, which includes the number of molecules at the interface, laser intensity, beam overlap, detection efficiency, etc., using the *ratio* of a single resonant feature in two polarization combinations is an effective way to eliminate the effect of such complications. For some molecules the same information can be even gained with a single spectrum by comparing more than one mode (with prior knowledge of the amplitudes of their individual hyperpolarizabilites).

A good example to consider for orientational analysis is the methyl (CH_3) group. Many organic molecules contain at least one methyl group, so orientational analyses are often based on this moiety. The CH_3 group possesses C_{3v} symmetry and can often be considered freely rotating around the primary axis of symmetry (the c-axis). From its symmetry it can be shown that the non-zero components of the hyperpolarizability are the β_{ccc} and β_{aac} (note here that the (a,b,c) are used as coordinates in the molecular frame with c aligned along the principle axis, and (x,y,z) are used to refer to the lab frame with z pointing perpendicular to the experiment interface)[43].

Because the surface possesses C_∞ symmetry, it is often assumed that molecules will also orient randomly with respect to rotation around the z axis. This is a reasonable simplification, except for systems where long range order in the xy plane is expected such as self assembled alkanethiolate monolayers, which have correlated tilt direction over very large crystal domains. If xy isotropy is assumed, then the orientation of an ensemble of methyl group can be totally described by the average angle of tilt from the surface normal, θ, and the width of the distribution around that average, d.

Figure 2.5 shows the calculated intensity of the methyl symmetric stretch as a function

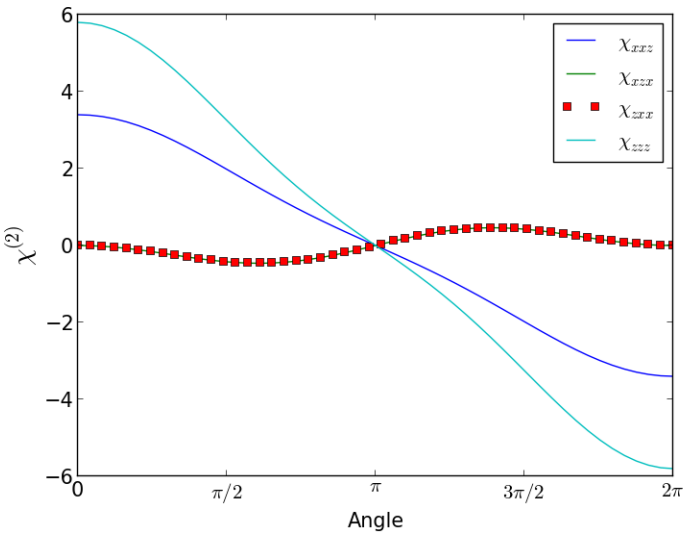

Figure 2.5: The magnitude of $\chi^{(2)}_{xxz}$,$\chi^{(2)}_{xzx}$,$\chi^{(2)}_{zxx}$ and $\chi^{(2)}_{zzz}$ of a methyl symmetric stretch mode as a function of its tilt angle with respect to the surface normal. It is worth noting that the xzx and zxx components of $\chi^{(2)}$ are equal for the methyl group and their contributions to the overall SFG intensity become distinct only in the difference in the z and x components of the electric field strength and the Fresnel factor difference.

of its tilt angle with all the Fresnel factors set to unity, and assuming a uniform distribution of rotational angles.

The distribution parameter, d is important to consider, because it can considerably change the calculated intensity. In the case of a non-zero d, the SFG signal can be considered simply the weighted average of the signal from each the methyl groups at their respective tilt angles. Figure 2.6 shows the spread of tilt angles with their weights for an assumed Gaussian distribution of tilts.

Evident from equations 2.10 - 2.13 is that the the Fresnel factors must be carefully calculated. In practice this can be quite difficult and introduce significant error into the calculation. Especially problematic is the knowledege of the interfacial refractive index $n_{interface}$ in the definition of L_{zz}. Some literature uses the average of the refractive indices of the two infinite media and some have used Shen's method of calculation, but the most effective method remains undetermined.

In practical terms, the precise calculations of the local field correction factors and the lack of knowledge about the molecular distribution leave much to be desired in the calculation of the orientation of molecules at the interface. In addition, even were that trivial, the accurate fitting of SFG data can sometimes be challenging, especially in spectra with many overlapping peaks or where the feature of interest is difficult to resolve above the noise. A different method has been developed which can significantly improve the accuracy of measurement, called the polarization null angle (PNA) approach[15,44], and it ingeniously utilizes the possibility for the canceling of elements of $\chi^{(2)}$ in a "mixed" polarization experiment (usually where the visible pulse is set halfway between s and p polarization). The SFG po-

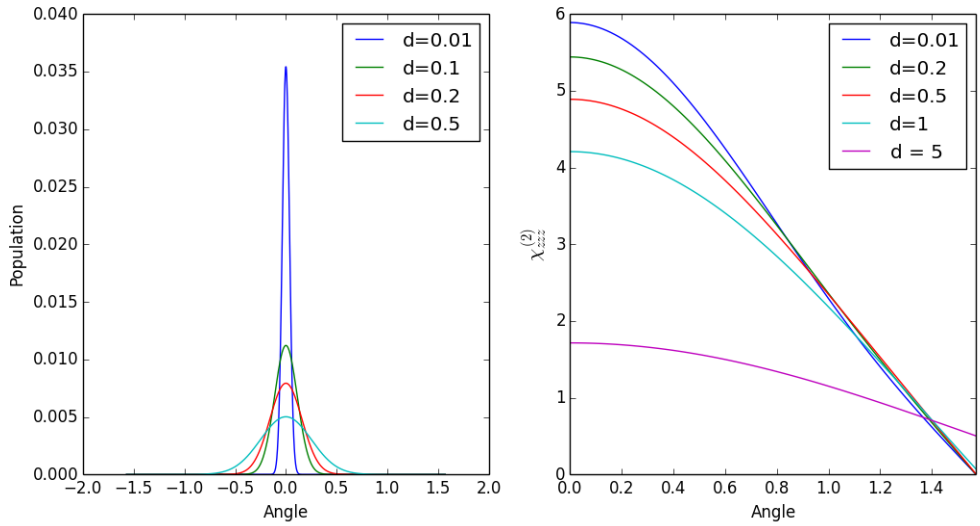

Figure 2.6: A graphical depiction of the effect of parameter d. Top left: graph of the distributions of the tilt angle around the average for d = 0, d= 0.1 radians and d = 0.5 radians. Top Right: the amplitude of $\chi^{(2)}_{zzz}$ for the methyl stretching transition with varying d values. Notice that as the system becomes more isotropic (as d increases) the value of χ tends toward a constant.

larization can be swept between 0 and π and the orientation of a peak determined from the SFG polarization at which a resonant feature disappears from the spectrum. This method is only slightly more complicated than the traditional approach and can yield a much more accurate result.

Conclusions

Sum-frequency generation vibrational spectroscopy is a unique tool with high sensitivity and surface-selectivity, the major strength of which is its ability to investigate the molecules at an interface without spectral information from the bulk material. SFG has been applied to numerous interfaces, and its specific application to catalyst surfaces has yielded information on the mechanism of surface catalyzed reactions. SFG spectroscopy is similar to IR and Raman spectroscopy but differs in its selection rules as well as its coherent nature. A special feature of SFG is the ability to use its polarization dependence to determine the orientation of an ensemble of molecules at a surface. SFG is a technique with the ability to address as yet unanswered questions about the chemistry of surfaces.

References

[1] Boyd, R. *Nonlinear Optics*; Elsevier Inc., 2008.

[2] Shen, Y. *Principles of Nonlinear Optics*; John Wiley and Sons, Inc., 2003.

[3] Shen, Y. *Surface Science* **1994**, *299*, 551–562.

[4] Lambert, A.; Davies, P.; Neivandt, D. *Appl. Spectrosc. Rev.* **2005**, 103.

[5] Somorjai, G.; Li, Y. *Introduction to Surface Chemistry and Catalysis*; John Wiley and Sons Inc., 2010.

[6] Shen, Y. *Nature* **1989**, *337*, 519–525.

[7] Zhu, X.; Suhr, H.; Shen, Y. *Physical Review B* **1987**, *35*, 3047–3050.

[8] Guyotsionnest, P.; Hunt, J.; Shen, Y. *Physical Review Letters* **1987**, *59*, 1597–1600.

[9] Hunt, J.; Guyotsionnest, P.; Shen, Y. *Chemical Physics Letters* **1987**, *133*, 189–192.

[10] Su, X.; Kung, K.; Lahtinen, J.; Shen, Y.; Somorjai, G. *Journal Of Molecular Catalysis A-Chemical* **1999**, *141*, 9–19.

[11] Baldelli, S.; Eppler, A.; Anderson, E.; Shen, Y.; Somorjai, G. *Journal Of Chemical Physics* **2000**, *113*, 5432–5438.

[12] Miranda, P.; Pflumio, V.; Saijo, H.; Shen, Y. *Journal Of The American Chemical Society* **1998**, *120*, 12092–12099.

[13] Stanners, C.; Du, Q.; Chin, R.; Cremer, P.; Somorjai, G.; Shen, Y. *Chemical Physics Letters* **1995**, *232*, 407–413.

[14] Lu, R.; Gan, W.; Wu, B.; Zhang, Z.; Guo, Y.; Wang, H. *Journal Of Physical Chemistry B* **2005**, *109*, 14118–14129.

[15] Chen, H.; Gan, W.; Wu, B.; Wu, D.; Zhang, Z.; Wang, H. *Chemical Physics Letters* **2005**, *408*, 284–289.

[16] Chen, Z.; Shen, Y.; Somorjai, G. *Annual Review Of Physical Chemistry* **2002**, *53*, 437–465.

[17] Onorato, R.; Yoon, A.; Lin, J.; Somorjai, G. *J. Phys. Chem. C* **2012**, 9947.

[18] Holinga, G.; York, R.; Onorato, R.; Thompson, C.; Webb, N.; Yoon, A.; Somorjai, G. *J. Am. Chem. Soc.* **2011**, 6243.

[19] York, R.; Holinga, G.; Somorjai, G. *Langmuir* **2009**, 9369.

[20] Ebben, C. J.; Ault, A. P.; Ruppel, M. J.; Ryder, O. S.; Bertram, T. H.; Grassian, V. H.; Prather, K. A.; Geiger, F. M. *Journal Of Physical Chemistry A* **2013**, *117*, 6589–6601.

[21] Shrestha, M.; Zhang, Y.; Ebben, C. J.; Martin, S. T.; Geiger, F. M. *Journal Of Physical Chemistry A* **2013**, *117*, 8427–8436.

[22] Cremer, P.; Su, X.; Shen, Y.; Somorjai, G. *Journal Of The American Chemical Society* **1996**, *118*, 2942–2949.

[23] Lee, K. B. H.; Komvopolous, K.; Yang, P.; Somorjai, G. *Nano Letters* **2007**, *7*, 3097–3101.

[24] Bratlie, K.; Komvopolous, K.; Somorjai, G. *Journal of Physical Chemistry C* **2008**, *112*, 11865–11868.

[25] Cremer, P.; Su, X.; Shen, Y.; Somorjai, G. *Journal Of Physical Chemistry B* **1997**, *101*, 6474–6478.

[26] Cremer, P.; Su, X.; Somorjai, G.; Shen, Y. *Journal Of Molecular Catalysis A-Chemical* **1998**, *131*, 225–241.

[27] Aliaga, C.; Tsung, C.-K.; Alayoglu, S.; Komvopoulos, K.; Yang, P.; Somorjai, G. A. *Journal Of Physical Chemistry C* **2011**, *115*, 8104–8109.

[28] Kliewer, C. J.; Aliaga, C.; Bieri, M.; Huang, W.; Tsung, C.-K.; Wood, J. B.; Komvopoulos, K.; Somorjai, G. A. *Journal Of The American Chemical Society* **2010**, *132*, 13088–13095.

[29] Baldelli, S.; Markovic, N.; Ross, P.; Shen, Y.; Somorjai, G. *Journal of Physical Chemistry B* **1999**, *103*, 8920–8925.

[30] Bozzini, B.; De Gaudenzi, G. P.; Busson, B.; Humbert, C.; Six, C.; Gayral, A.; Tadjeddine, A. *Journal Of Power Sources* **2010**, *195*, 4119–4123.

[31] Bozzini, B.; Abyaneh, M.; Busson, B.; De, G.; Gregoratti, L.; Humbert, C.; Amati, M.; Mele, C.; Tadjeddine, A. *J. Power Sources* **2013**, 6.

[32] Vidal, F.; Tadjeddine, A.; Humbert, C.; Dreesen, L.; Peremans, A.; Thiry, P. A.; Busson, B. *Journal Of Electroanalytical Chemistry* **2012**, *672*, 1–6.

[33] Humbert, C.; Busson, B.; Six, C.; Gayral, A.; Gruselle, M.; Villain, F.; Tadjeddine, A. *Journal Of Electroanalytical Chemistry* **2008**, *621*, 314–321.

[34] Boronat, M.; Corma, A. *Journal Of Catalysis* **2011**, *284*, 138–147.

[35] Casanova, O.; Iborra, S.; Corma, A. *Chemsuschem* **2009**, *2*, 1138–1144.

[36] Climent, M. J.; Corma, A.; Iborra, S.; Mifsud, M. *Journal Of Catalysis* **2007**, *247*, 223–230.

[37] Richmond, G. *Chem. Rev.* **2002**, 2693.

[38] Eisenthal, K. *Chem. Rev.* **1996**, 1343.

[39] Bain, C. *J. Chem. Soc., Faraday Trans* **1995**, 1281.

[40] Miranda, P.; Shen, Y. *J. Phys. Chem. B* **1999**, 3292.

[41] Du, Q.; Freysz, E.; Shen, Y. *Physical Review Letters* **1994**, *72*, 238–241.

[42] Wang, H.; Gan, W.; Lu, R.; Rao, Y.; Wu, B. *International Reviews In Physical Chemistry* **2005**, *24*, 191–256.

[43] Chiaki, H.; Akamatsu, N.; Domen, K. *Applied Spectroscopy* **1992**, *46*.

[44] Lu, R.; Gan, W.; Wu, B.; Chen, H.; Wang, H. *Journal Of Physical Chemistry B* **2004**, *108*, 7297–7306.

Chapter 3

Experimental apparatus for sum-frequency generation spectroscopy and reaction rate studies

The requirements of a system to carry out SFG and reaction rate measurements in liquid-phase reactions catalyzed by heterogeneous catalysts are different from those required of a system to work in the gas phase. This chapter describes the design and construction of a flow reactor system in which the variables of liquid flow rate, reactant concentrations, temperature, and stir speed are controlled. The chapter also describes the incorporation of *in situ* SFG measurement in the internal reflection mode, which is accomplished by using an electron beam evaporated thin film metal as the catalyst. This system is used in the later chapters of this work in order to study aqueous alcohol oxidation on platinum catalysts.

Introduction

The Somorjai group has a long history of studying gas phase catalyzed reactions using sum-frequency generation. Since 1996, our group has characterized the intermediates on catalyst surfaces, first on single crystals, then using nanoparticles as model catalysts. In this way, the group began by studying the simplest system possible and then increased the experimental complexity. Moving to the solid/liquid interface can be considered a further step in complexity. One main challenge for performing SFG in the liquid phase is the strong absorption of the mid-infrared light used for SFG by the liquid. In addition, the enormous density increase (approximately one-thousand-fold) of the liquid phase compared to the gas means that the interfacial environment is always dominated by molecular liquid not bonded to the surface and therefore not participating in the reaction. Finally, the use a complex catalyst like a monolayer of nanoparticles on a support becomes much more difficult because of the existence of *two* interfaces - the nanoparticle/liquid and the support/liquid. One cannot accept that the main driving force for molecules to stay near the surface (and to order strongly enough to produce an SFG signal) is their chemical bond with an active metal. There are certain differences on the kinetics side as well, since the reactions in the liquid phase tend to be far slower than those we have studied in the gas phase, and some reactants (such as oxygen) are significantly limited in their solubility in liquids. Finally, the instrumentation for product measurement should be re-evaluated, since the commonest one for gas phase reactions, gas chromatography, is not perfectly suited for analysis of all liquid solutions.

This chapter describes the system that was designed and built as part of this work to allow us to study the liquid-phase alcohol oxidation reaction. Some of the desired properties

of the system were the ability to work in the flow mode (as opposed to the batch mode), the capability for *in situ* SFG measurements and minimization of SFG signal from the interfaces not of interest. The result was a flow mode liquid phase reactor optimized for studies of alcohol oxidation reactions and built to allow *in situ* SFG measurement, in which it is possible to study electron beam evaporated catalysts as well as any metal catalyst which can be anchored onto a glass slide.

Literature review: Studies of the solid/liquid interface with sum-frequency generation

The SFG literature is rich with examples of the utilization of sum-frequency generation vibrational spectroscopy to study the interface at the boundaries of one liquid and one solid. This includes the study of the adsorption of biomolecules (proteins and amino acids) on polymers[1,2], electrochemical reactions[3,4], the arrangement of water at the solid/liquid interface[5,6] surfactant and alkane monolayers[7] and the adsorption of ions on minerals[8]. The use of SFG in these circumstances is complicated by the factors listed in the introduction. While the spectroscopy setups used for most of these experiments are similar, two main strategies emerge, shown in Figure 3.1 - one where the infrared light passes through the liquid medium, and the other, which probes the surface via internal reflection.

The thin-layer analysis configuration, where light passes through a very thin layer of liquid, has been used by several groups. This configuration addresses the issue of IR absorption by the liquid by reducing the path length of the light through the liquid to a thin (100 μm or less) liquid layer between a transparent medium and the surface of interest. The minimization of artifacts from the liquid requires the thinnest layer possible, and reproducible spectra require precision in the layer thickness. Verreault *et al.* found that the sensitivity in a setup as described above was good enough to detect the CH stretching modes of a 1:99 non-deuterated:deuterated self-assembled monolayer on a gold surface[9]. Creatively, they were able to address diffusion issues in electrochemical studies by coating the transparent window with indium tin oxide and using that as a counterelectrode. Baldelli *et al.* investigated the species of carbon monoxide bound to a Pt(111) single crystal using a system of similar design[10]. Clearly, the advantage of the thin-layer analysis is that is can be used to study any flat interface. The major disadvantage, assuming that IR absorption artifacts are sufficiently small, is that the restricted bulk transport of molecules in the thin liquid layer makes this technique inappropriate for experiments requiring free flow of the liquid. Also, the separation of signal from the top interface (prism/liquid) and the bottom interface

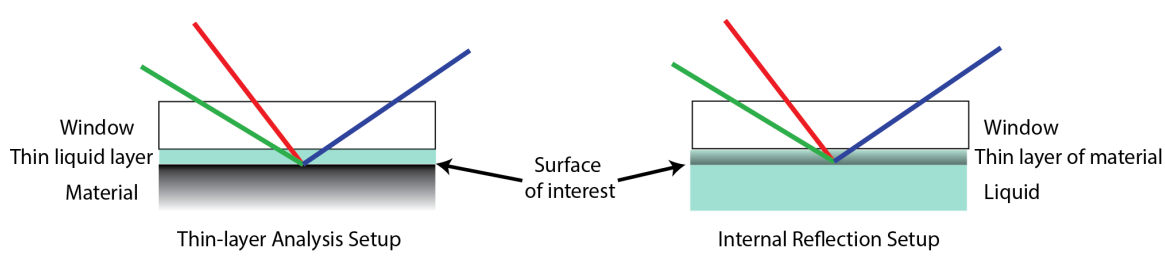

Figure 3.1: Schematic of the thin-layer analysis mode and the internal reflection mode for SFG of the solid-liquid interface.

(liquid/sample) has not been thoroughly investigated.

The internal reflection configuration has been used many times. It can be easily applied in situations where the material of study is transparent. For materials like silica or CaF_2 this can be the reflective surface of a window or prism. For other materials it is possible to coat a prism with a thin layer (1 nm - 1μm) of the material either by solution deposition (spin coating or drop casting) or by thermal or electron-beam evaporation in the case of non-soluble materials. A particularly good example of this is experiments studying polymer interfaces. Many researchers have used thin layers of polymer coated on a prism or window[1,2,11,12]. The polymers are inherently transparent to SFG and visible light, and they can be made transparent to infrared light in certain ranges of IR frequencies by deuterating them. In this case, the internal reflection mode has a major advantage in that none of the light need travel through an absorbing medium. In addition, total internal reflection can greatly enhance the SFG signal due to a huge increase in the Fresnel factors (the amplitude of the electric field at the interface). The internal reflection geometry has been used to study the surface of absorbing media as well, by coating the prism with a thin layer of metal[13–15]. Stein and co-workers showed that it was possible to obtain a spectrum of alkanethiolate monolayers through a 10 nm gold film. Similarly, Williams and co-workers reported their spectra of octadecanethiol and thiocyanate on 5 nm gold layers in the internal reflection mode. However, the signal decays quickly with film thickness due to adsorption and they were unable to see any signal from the opposite side of 20 nm films. Interestingly, in a number of reports comparing these internal reflection with external reflection geometries, the interference of resonant features from adsorbates with the background of the metal can be quite different[13,14,16]. It appears that a phase shift of the non-resonant background may exist in the thin film geometry relative to the external reflection mode. Especially important for catalytic studies, compared to using the thin-film analysis geometry, the study of metal surfaces by internal reflection mode is superior in cases where diffusion in the liquid is important, but sensitivity may be compromised due to absorption by the metal film.

In-situ SFG flow reactor for liquid-phase catalysis

The system described herein was inspired by current designs in the Somorjai group, with some important modifications to make the system suitable for liquid phase studies. This chapter will discuss the entire setup - the laser and non-linear frequency conversion element, the specially designed SFG reactor flow cell, the home-made index matching setup for the use of flat samples in a prism geometry, sensitive detection of products using gas chromatography.

Flow cell reactor

The experimental setup used for simultaneous reaction rate measurement and sum frequency generation spectroscopy centers around a home-built flow mode reaction cell. The flow cell consists of a central Teflon piece containing the reaction reservoir, liquid inlet and outlet ports, and thermocouple port. This piece rests in an aluminum block, which has threaded holes for the attachment of tubing, an internal magnet for the magnetic stirring of the liquid in situ and also contains the heating element used to maintain temperature. This aluminum block is attached at the bottom to a translation stage which allows for precise alignment on

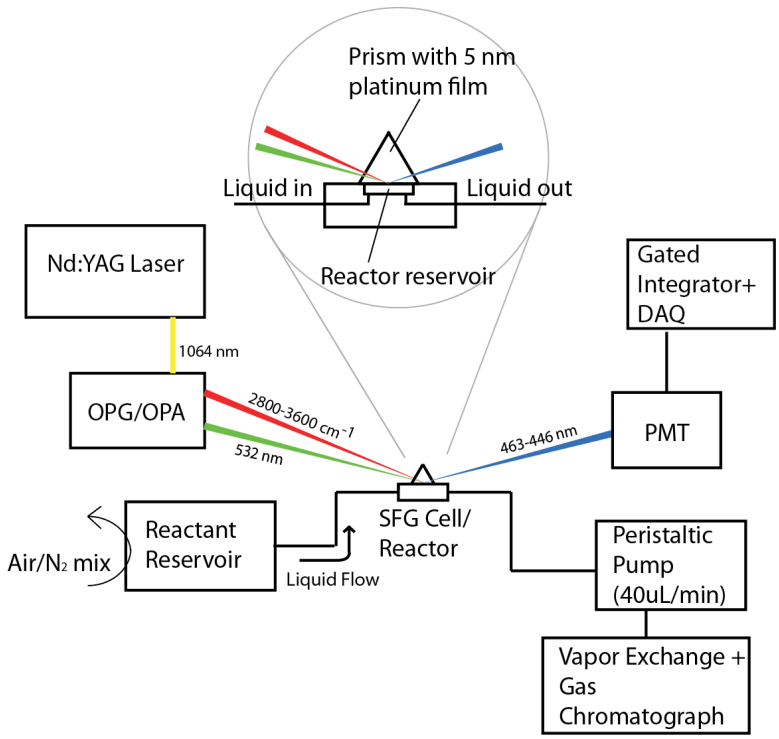

Figure 3.2: Schematic of the setup for integrated SFG and reaction studies.

the sample for spectroscopic purposes.

The Teflon reaction cell

The reaction well was machined from Teflon. Teflon was chosen for the insert material because of its high level of chemical inertness. The alcohol oxidation reaction is known to occur on many metals and some oxides, so a polymer was chosen over an inorganic material. Teflon's inertness also makes it amenable to harsh cleaning by piranha (H_2O_2:H_2SO_4 1:3 v/v) which is critical for the SFG experiments. The measurements of the insert are shown in Figure 3.2. The reaction well has a volume of 770 μL. In the Teflon piece the well has only three walls and is finally sealed with the glass slide onto which the platinum catalyst has been deposited. A thermocouple embedded inside the flow cell, but out of contact with the liquid, allows for temperature control with an external heating unit with PID feedback.

Aluminum housing block

While Teflon has many properties that are desirable in its use as a flow cell reactor, it also has some limitations; namely Teflon has a low thermal conductivity and low hardness, especially at temperatures above 100 °C. This means that it is not suitable to be in contact with high temperature elements and that threaded holes are easily degraded over time. This drawback was addressed by an aluminum housing block in which the insert sits. The block contains the threaded holes for the tube fittings and a heating pad is wrapped around the block. Thus heat is transferred more evenly to the entire insert. The block also contains an

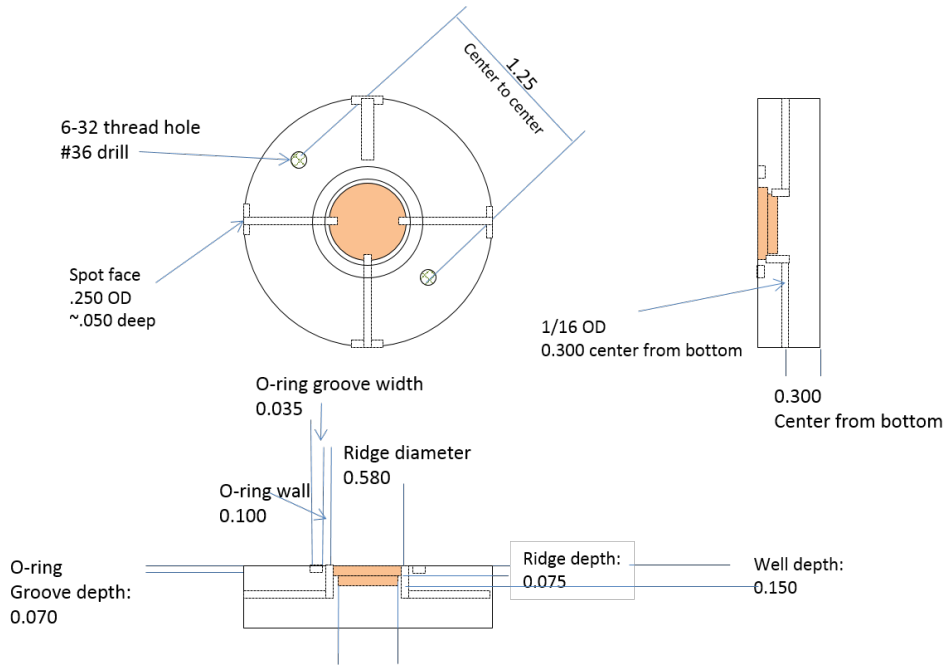

Figure 3.3: The design of the Teflon flow cell used for in situ SFG spectroscopy and reaction rate measurements. Units are in inches.

integrated magnetic stirring apparatus, since the whole setup must fit in the 3"x3" space for the spectroscopy and available stir plates are not sufficiently small. The integrated stirring setup allows the liquid inside the cell to be stirred using a magnetic stir bar at 600 rpm.

Flow control

The flow of liquid was driven and controlled by a peristaltic pump (Watson-Marlow 120U) using silicone tubing with inner diameter of 0.060 in. The peristaltic pump is capable of flow rates down to 20 μL/min, and is usually run at 40-80 μL/min, such that the reactant conversion is less than 25%.

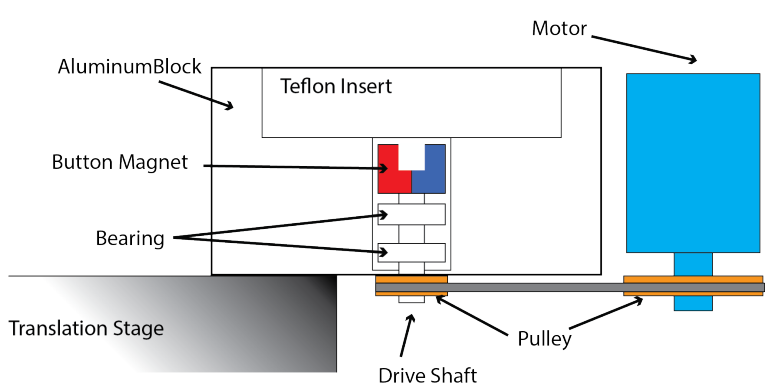

Figure 3.4: Side view of the aluminum block with integrated magnetic stirring.

Oxygen concentration control

In batch mode reactors for reactions where one of the reactants is a gas (such as H_2 or O_2), the dissolved concentration of the gaseous reactant is controlled by the partial pressure of the gas in the space above the liquid. The concentration of a gas dissolved in a liquid follows Henry's law, which states for O_2,

$$k_H \cdot [O_2]_{dissolved} = p_{O_2} \tag{3.1}$$

This principle was applied here by bubbling reactant liquid (the alcohol containing solution) with a gas with a mixture of air and nitrogen whose fractions were controlled by calibrated mass flow controllers. The mole fraction of oxygen in air is 0.18, so the partial pressure of oxygen is calculated by,

$$p_{O_2} = (v_{air} \cdot 0.18)/(v_{air} + v_{N_2}) \tag{3.2}$$

where v is the flow rate. The concentration of oxygen in solution was maintained during the flow to the cell by using stainless steel tubes and the peristaltic pump used to pump the liquid was placed after the cell, because silicone tubing (used for the pump) is highly permeable to gases. Henry's law constants were taken from the literature[17,18].

Product detection by gas chromatography

Gas chromatography (GC) is commonly used to detect the composition of gas phase mixtures. The main principle behind GC is the partitioning of molecules between gaseous and adsorbed states. Separation is effected by passing a mixture of components through a column - packed or capillary - in which is deposited a material, the stationary phase, the surface of which is chemically tailored to interact strongly with the compounds of interest. Molecules driven through the column by a mobile phase, also known as carrier gas, which is usually helium or hydrogen, are in a dynamic equilibrium between being carried by the mobile phase and adsorbed on the surface of the stationary phase. The components of the mixture are separated by their equilibrium constants for this phase exchange, known as the partition coefficients.

Detection of the small molecule products at concentrations as low as one ppm was carried out using a home-built dynamic liquid-vapor exchange column coupled with gas chromatography. Nitrogen gas was flown at 2.67 mL/min up through a glass tube held at 18 °C while the product mixture was dripped down the tube. For the residence time of the gas in the tube, the vapor of the product was transferred to the N_2 gas, which could be sampled by GC. Compared to the reactant (alcohol) and solvent (water), the vapor pressure of the product (aldehyde or ketone) is high, so that it can be detected with increased sensitivity relative to the other components of the mixture, which are at many orders of magnitude greater concentration. It was found empirically that the response of this system was highly linear, but changed with alcohol concentration, so a separate calibration was always carried out for each alcohol concentration used. The time response was fast and less than the time required for the GC to finish a run (15 min). The flow rate of N_2 proved low enough that the peak area of product in the GC was not highly sensitive to this.

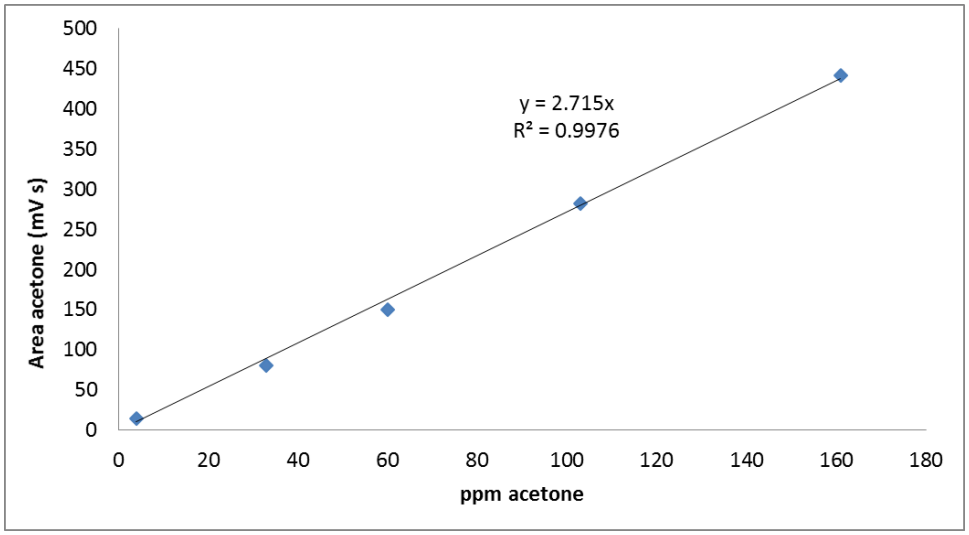

Figure 3.5: Example of a calibration curve for the liquid-vapor exchange system. The signal of acetone was integrated to obtain the area in units of mV·s. The calibration proved to be highly linear over the range of interest.

In a flow system, the reaction rate is proportional to the amount of product in the reacted mixture. The reaction rate,k, in mol/s can be calculated as

$$k = ([P] \cdot V_{cell})/t = [P]\, v \tag{3.3}$$

where [P] is the concentration of product in the product mixture in mol/L, V_{cell} is the volume of the cell where the reactant mixture makes contact with the catalyst, and t is the residence time in the cell. Dividing V_{cell} by t simply gives r, the flow rate. A turnover frequency is calculable directly from k by

$$TOF = k/N_{Pt} \tag{3.4}$$

where N_{Pt} is the number of accessible active sites on the surface. The site density for Pt(111) (1.52 x 10^{15} cm^{-2}) can be used as an estimate when the macroscopic catalyst surface area is known.

Sum-frequency generation spectroscopy setup

Laser and frequency conversion components

The heart of the SFG setup used in the experiment described in this work is a picosecond neodymium:yttrium aluminum garnet (Nd:YAG) laser. The laser produces 20 ps pulses of 15-30 mJ at 1064 nm using a combination of active and passive mode-locking. The Nd:YAG laser pumps a non-linear system for generation of visible (532 nm) and tunable mid-IR (2700-4000 cm^{-1}) shown in Figure 3.6. The 532 nm is produced by second harmonic generation of the 1064 nm pump in a beta barium oxide (BBO) crystal. Part of this 532 nm pulse is split off to pump two potassium titanyl phosphate (KTP) crystals for optical parametric

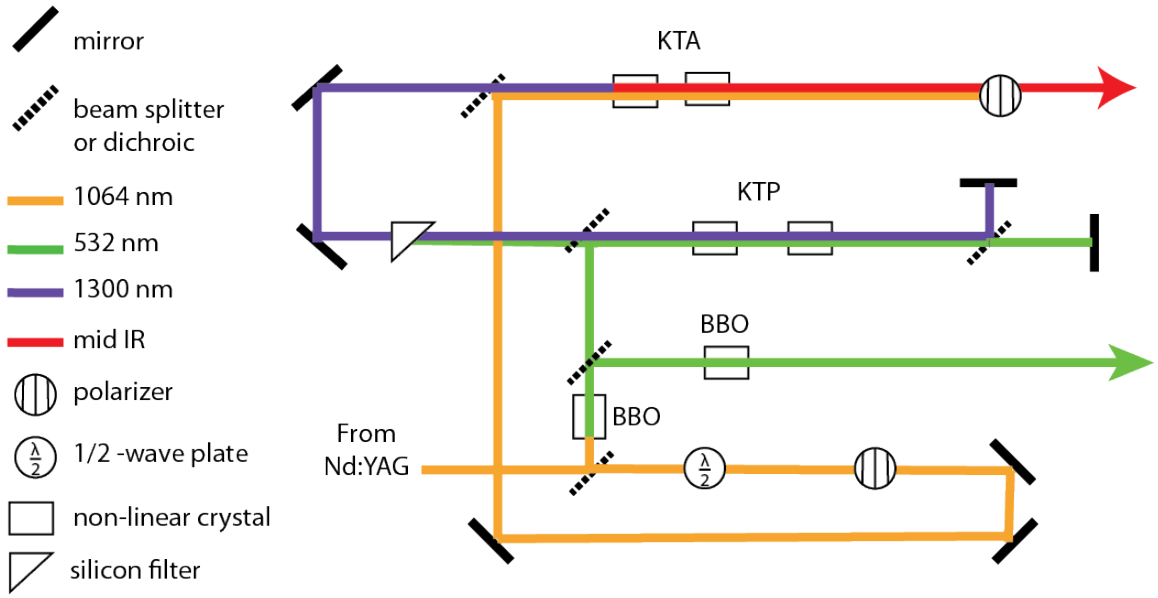

Figure 3.6: Diagram of the non-linear system for conversion of the Nd:YAG output to visible (532 nm) and tunable infrared (2700-4000 cm^{-1}).

generation (OPG) where one photon of 532 nm produces two photons of ∼1300 nm and ∼800 nm. These frequencies are then amplified on a second pass through the KTP crystals. The specific energies of the photons produced in the OPG/OPA stage is controlled by utilizing the angle dependent index of refraction of the KTP, which changes the frequencies that satisfy the phase matching requirements for this process. The idler from this stage (1300 nm) can be used as the signal for a difference frequency generation (DFG) stage, pumped by 1064 nm from the Nd:YAG laser. In this stage, the difference frequency is generated in two potassium titanyl arsenate (KTA) crystals, which are rotated to optimize the phase matching conditions. This DFG stage results in a pulse in the mid-IR region.

Sample and detection system

Following the OPG/OPA system, the visible and mid-IR pulses are polarization adjusted and directed toward the sample surface at the angles desired for SFG – 62° for the green and 45° for the IR. The incident angles were chosen near the critical angle, but far enough off of the critical angle that the signal was not highly dependent on refractive index or incident angle. Figure 3.7 shows the incident angles and the SFG angle as used in the experiments described in this report.

The temporal overlap is optimized using a delay stage of approximately two meters for the green pulse. The SFG light exiting the prism is directed into a photomultiplier tube and the PMT signal was integrated using a gated integrator system with 100 ns gate time.

Thin films of catalysts are necessary for enough transmission of incident and exiting light. Electron beam evaporation is a method of controllably depositing thin films of metals that are spatially homogeneous and clean of organics which can contaminate the SFG spectrum.

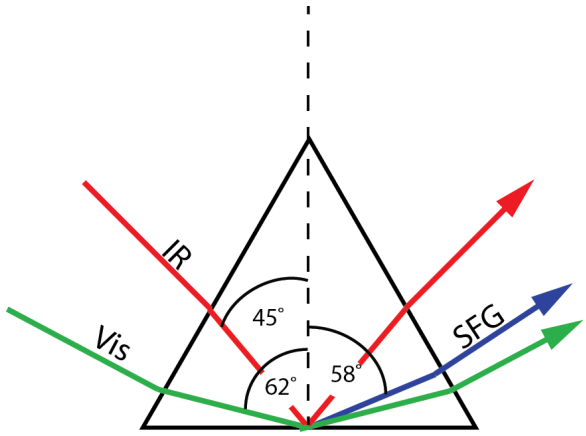

Figure 3.7: The angles of incidence for visible and IR pulses on the prism used in SFG experiments. The visible light is incident at 62° to the normal, while the IR pulse is incident at 45°. The direction of the SFG is determined by the conservation of momentum, and it exits the prism at an angle slightly lower angle than the visible, allowing for the spatial separation of the two.

It was found that a nominal 5 nm thickness of platinum provides a continuous film, as measured by XPS while being thin enough to be transmissive. A 2 nm titanium adhesion layer improves the film stability with respect to delamination and laser ablation. These films were also seen to be stable up to 500 °C.

In the case of SFG on of a thin layer sandwiched between two infinite media, SFG is generated at both interface with intensities determined by the Fresnel coefficients of each interface. These have been calculated previously[19]. It is important to consider these coefficients when the thin film is of a material with a non-zero non-resonant susceptibility as for some metals, like platinum. The six Fresnel factors, three for the quartz/platinum interface (interface 1) and three for the platinum/water interface (interface 2), are plotted in Figure 3.8 for the quartz/platinum/water system and the quartz/platinum/isopropanol system, taking $n_{quartz} = 1.46, n_{water} = 1.337, n_{platinum} = 2.078 + 3.629i$ and $n_{isopropanol} = 1.38$. At 60° the major contributions come from the $L_{xx,2}$, $L_{zz,2}$ and $L_{xx,1}$ factors.

The catalysts must be on a flat transparent surface such as glass or CaF_2. CaF_2 is preferable, because it is totally transparent to the mid-IR, but quartz was used instead, because it is transparent to visible and mostly transparent to mid-IR, thermally stable up to high temperatures, inactive as a catalyst, resistant to any solvent, and inexpensive. In order to maximize the transmission to and away from the sample, a prism is necessary. CaF_2 is used here because of its high transmission in the IR. In some laboratories catalysts are deposited directly on the prism. The separation of the quartz sample support from the prism allows for greater ease in sample preparation and greater flexibility in sample pretreatment. However the problem of light transmission between the bottom of the prism and the glass slide must be overcome. To this end a special, IR-transparent index matching gel was developed in the laboratory.

Since the transmission efficiency across an interface depends on the nearness of the indices of refraction of the materials, organic molecules are fairly well suited to compose the index

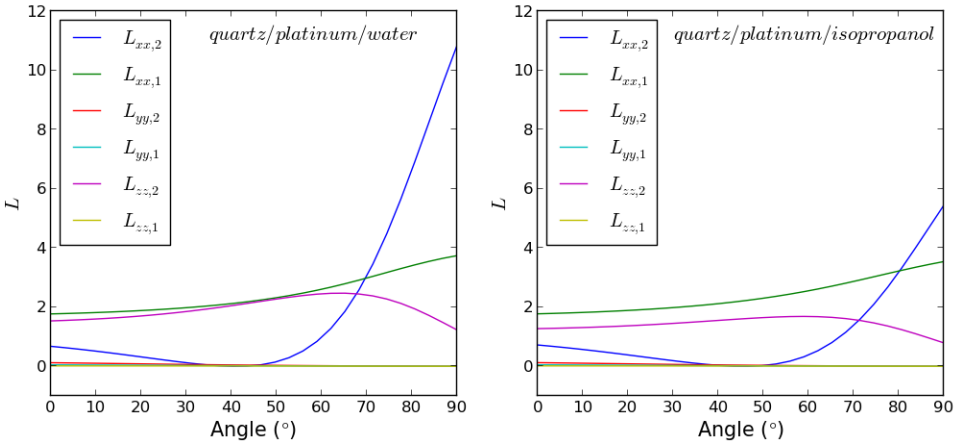

Figure 3.8: The calculated Fresnel factors for (left) the quartz/platinum/water system and (right) the quartz/platinum/isopropanol system. L_1 is the Fresnel factor for the quartz/platinum interface and L_2 the factor for the platinum/liquid interface.

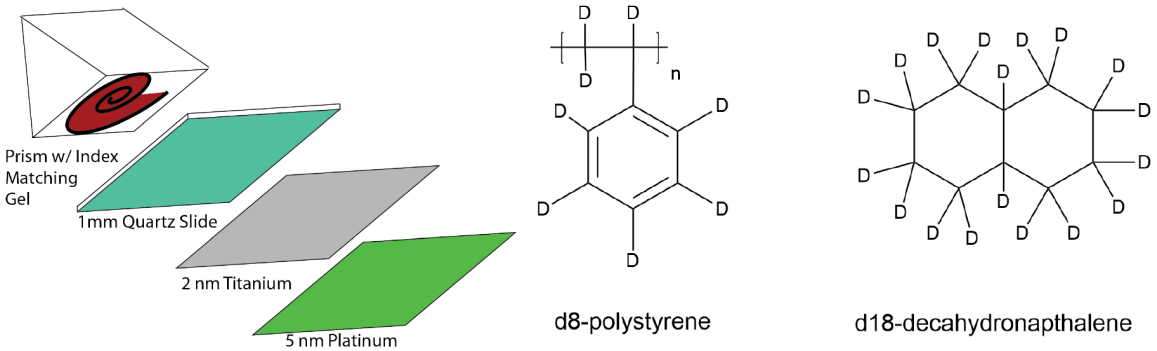

Figure 3.9: Left: Schematic of the catalyst used for SFG and reaction studies coupled with a CaF_2 prism using the custom index matching gel. A 2 nm adhesion layer is evaporated onto a glass slide, followed by 5 nm of platinum metal. The glass slide is index matched to a CaF_2 prism using a homemade index matching gel. Right: Molecular structure of the components of the index matching gel.

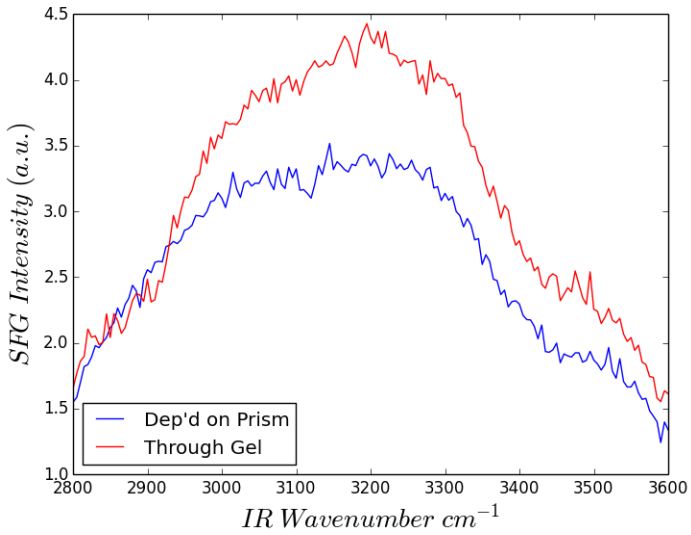

Figure 3.10: Reference spectra of gold (blue) deposited directly on to a SiO_2 prism, and (red) deposited onto a glass slide and then index matched to a CaF_2 prism with the home-made index matching gel.

matching gel. Additionally, the gel must be transparent to IR so fully deuterated organics are necessary. The ideal mixture was found to be a 1:6 mixture by weight of d_8-polystyrene and d_{18}-decahydronaphthalene. The primary measure of efficacy of the index matching gel is the transmission of light across the CaF_2/gel and gel/SiO_2 interfaces. This can be measured simply by comparing the SFG of a thin film of gold using the prism/gel/slide combination with that of a thin film of gold evaporated directly onto a prism. The result of this experiment is shown in Figure 3.10. The index matching gel apparently delivers most of the incident light across the two interfaces and does not introduce major artifacts into the spectrum. The most important region between 2800 and 3100 cm^{-1} is highly comparable between these two samples. The slight increase in SFG signal can be attributed to the lower absorption of IR light in this region by the CaF_2 prism compared to the silica prism used as the control.

Conclusions

Sum-frequency generation studies of heterogeneous catalyst surfaces in the liquid phase require a reactor system optimized for liquid phase reactions. A flow cell reactor with *in situ* SFG capabilities has been herein constructed and characterized. The main reaction parameters controllable in this system are liquid flow rate, reactant concentration, reaction temperature and mass transport. The spectroscopic setup was optimized for the particular studies described in this work with respect to catalyst film thickness, catalyst surface coverage and incident angles. In the following chapters the work described utilizes this *in situ* SFG reactor system.

References

[1] Holinga, G.; York, R.; Onorato, R.; Thompson, C.; Webb, N.; Yoon, A.; Somorjai, G. *J. Am. Chem. Soc.* **2011**, 6243.

[2] Chen, Z.; Shen, Y.; Somorjai, G. *Annual Review Of Physical Chemistry* **2002**, *53*, 437–465.

[3] Tadjeddine, A.; Le Rille, A.; Pluchery, O.; Vidal, F.; Zheng, W.; Peremans, A. *Physica Status Solidi A-Applied Research* **1999**, *175*, 89–107.

[4] Gomes, J.; Bergamaski, K.; Pinto, M. S.; Miranda, P. *J. Catal.* **2013**, 67.

[5] Richmond, G. *Chem. Rev.* **2002**, 2693.

[6] Du, Q.; Freysz, E.; Shen, Y. *Physical Review Letters* **1994**, *72*, 238–241.

[7] Miranda, P.; Pflumio, V.; Saijo, H.; Shen, Y. *Journal Of The American Chemical Society* **1998**, *120*, 12092–12099.

[8] Jordan, S. S. D.; Troiano, J.; Geiger, F. *Abstracts Of Papers Of The American Chemical Society* **2013**, *245*.

[9] Verreault, D.; Kurz, V.; Howell, C.; Koelsch, P. *Rev. Sci. Instrum.* **2010**, 063111.

[10] Baldelli, S.; Markovic, N.; Ross, P.; Shen, Y.; Somorjai, G. *Journal Of Physical Chemistry B* **1999**, *103*, 8920–8925.

[11] York, R.; Holinga, G.; Somorjai, G. *Langmuir* **2009**, 9369.

[12] Onorato, R.; Yoon, A.; Lin, J.; Somorjai, G. *J. Phys. Chem. C* **2012**, 9947.

[13] Stein, M. J.; Weidner, T.; Mccrea, K.; Castner, D. G.; Ratner, B. D. *Journal Of Physical Chemistry B* **2009**, *113*, 11550–11556.

[14] Williams, C.; Yang, Y.; Bain, C. *Langmuir* **2000**, *16*, 2343–2350.

[15] Thompson, C.; Carl, L.; Somorjai, G. *Journal Of Physical Chemistry C* **2013**, *49*, 26077–26083.

[16] Bain, C. *J. Chem. Soc., Faraday Trans* **1995**, 1281.

[17] Battino, R.; Rettich, T.; Tominaga, T. *J. Phys. Chem. Ref. Data* **1983**, *12*, 163–178.

[18] Tokunaga, J. *J. Chem. Eng. Data* **1975**, 41.

[19] Shen, Y. *Nature* **1989**, *337*, 519–525.

Chapter 4

Isopropanol oxidation on platinum catalysts studied using SFG and reaction rate measurements

Sum-frequency generation (SFG) vibrational spectroscopy was applied to study the solid-liquid interface in the heterogeneously catalyzed oxidation of isopropanol to acetone in aqueous solution on platinum. The mole fraction of alcohol was varied from 0 to 1. At isopropanol mole fractions less than 0.14 and above 0.23 the turnover frequency for acetone is approximately 20 hr^{-1}. A three-fold increase in the reaction rate is seen when isopropanol is present with concentrations in this intermediate range (x_{IPA} 0.14 – 0.23). SFG spectra indicate that in aqueous mixtures of isopropanol the solid-liquid interface is dominated by the alcohol, even at mole fractions of alcohol less than 0.3. At isopropanol concentrations where the highest reaction rates are observed, SFG shows the presence of water and alcohol at the catalyst interface, whereas, above and below these concentrations, either water or isopropanol is not detectable at the surface. We attribute this correlation to a dependence of the reaction rate on both alcohol and water. These results demonstrate the importance of monitoring the interfacial concentration in liquid phase heterogeneous catalysts and provide evidence for the effect of water as a solvent stabilizer in the reaction.

Introduction

The catalytic action of metals on alcohol oxidation was described first by J. W. Döbereiner in 1823 on platinum[1]. Since that time the dehydrogenative oxidation of alcohols to their respective ketones, aldehydes, and acids has been studied on all the platinum metals, copper, silver, – even gold - in the gas and liquid phases, with simple alcohols as substrates and large polyols[2–8]. The reaction is usually studied under mild conditions; at room temperature or slightly above. The pH is usually neutral or basic as the reaction rate increases with pH. The dissolved oxygen concentration can be controlled by controlling the oxygen partial pressure above the liquid. The platinum catalyst most commonly used is in the form of small particles deposited on a carbon support.

This chapter discusses the oxidation of isopropanol (IPA) on thin film platinum catalysts in aqueous conditions[9]. Although the dehydrogenative oxidation of alcohols has been studied in detail, it is still not known what the roles certain species, i.e. asdsorbed oxygen species and water, play in the reaction. In the work presented here SFG is used to investigate the interfacial environment, which is significantly different from the bulk liquid in terms of local component concentrations and this information is correlated with the catalytic activity measured simultaneously. The SFG spectra reveal a range of bulk alcohol concentration in

which both water and alcohol are detectable in the interfacial region, and it is shown that the platinum catalyst has increased activity in this concentration range. The experiments in this chapter were originally intended to investigate the role of oxygen, but ended up demonstrating the importance of water in the reaction instead by pinpointing the concentration regimes in which competitive occupation of the interfacial region plays a role in determining the catalytic reaction rates. Unexpectedly, the trends in the SFG spectra did not correlate to the trends in activity with their relation to the oxygen concentration, which is a good indication that the molecule which are SFG active are not the active intermediates. The results are at once a perfect example of the value of microscopic information of molecules at the surface – something only obtained by surface-specific techniques - as well as a demonstration of the complexity of the solid/liquid interface compared to the solid/gas because of the high concentration of non-adsorbed species.

Experimental details

Catalyst preparation

Thin-film platinum catalyst samples were deposited onto quartz prisms using electron beam evaporation on top of a 2 nm titanium adhesion layer. Base pressure for evaporation was less than 10^{-5} Torr.

The thickness of platinum was measured to be 5 nm by a quartz crystal microbalance calibrated to the platinum density and the distance of the sample from the crucible. A similarly prepared film on a silicon TEM grid with a native silicon oxide layer was used for imaging purposes. Figure 4.1 shows a TEM image of the 5 nm platinum sample on such a TEM grid.

Reaction rate measurements

Reaction kinetics and SFG were performed in a Teflon flow cell with volume 770 μL equipped with magnetic stirring as described in the experimental chapter. The mole fraction of isopropanol was varied between 0 and 1 in mixtures with ultrahigh purity 18 MΩ water. The liquid pH was not adjusted. Liquid flow rate was controlled by a peristaltic pump at 40 μL/min. Catalysts were reduced *in situ* prior to reaction in pure hydrogen for one hour at 80 °C. The dissolved O_2 concentration in the reactant mixture was controlled between 0 and 300 μM by bubbling the liquid with mixtures of nitrogen and air. The O_2 concentration was then calculated using the solubilities from Tokunga and coworkers (see Figure 4.2)[10]. During a reaction run the cell was held at 30 °C and the concentration of oxygen was increased stepwise at intervals of approximately 2 hours beginning at 0 μM. The reaction rate was allowed to come to steady state before moving on to the next oxygen concentration. Product concentration was determined by analysis of the effluent vapors via and in-line gas chromatograph equipped with a packed Hayasep-T column and a photoionization detector.

SFG measurements

In order to carry out SFG measurements, the flow reactor described above was incorporated into the SFG system, which has been described in detail previously[11]. In these experiments,

Figure 4.1: HR-TEM image of 5 nm electron beam deposited platinum on an ultra-thin silicon substrate. It is expected that platinum deposited on quartz forms islands similar to those imaged.

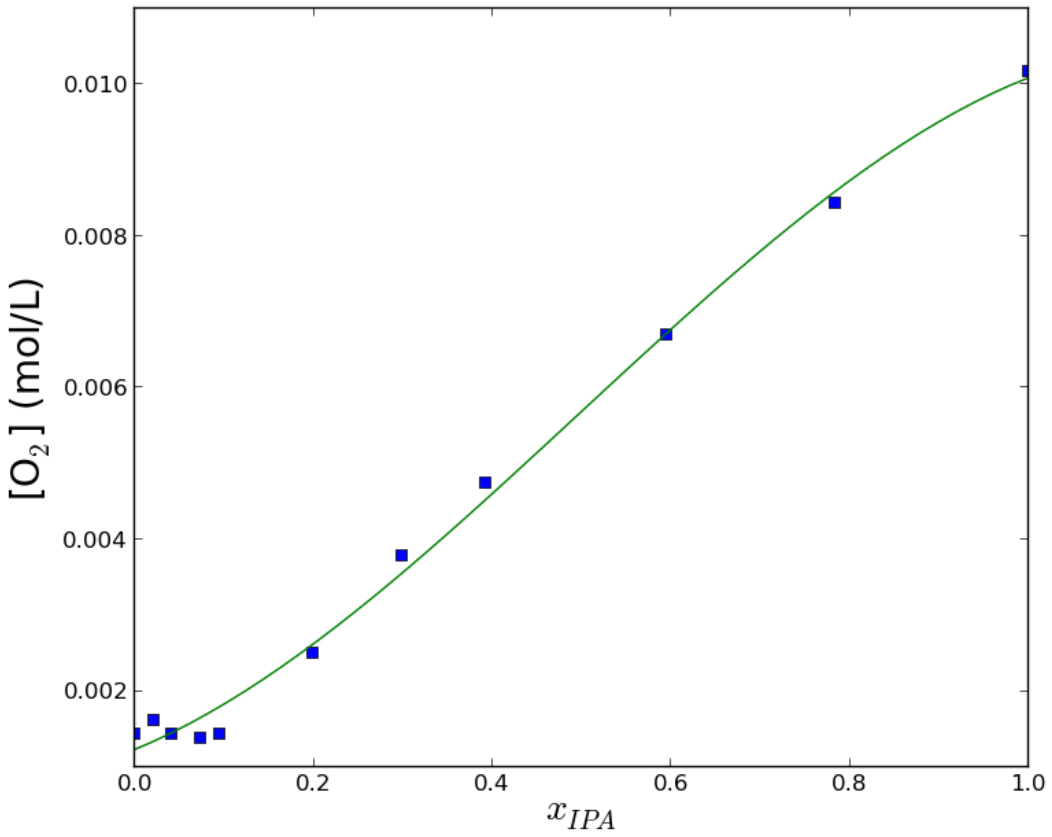

Figure 4.2: Oxygen solubility in isopropanol/water mixtures from the work by Tokunaga et al. (squares). Polynomial fit used for the calculation of solubilities at intermediate concentration is shown (solid line).

the infrared frequency was scanned from 2800-3600 cm^{-1} and its energy was approximately 100 μJ. The visible wavelength used was 532 nm (40 μJ). Sum-frequency light was detected by a photomultiplier connected to a gated integrator. The polarization combination used in the experiment was *ppp*, which refers to perpendicular polarization for all beams relative to the sample surface. The data points in spectra shown in this paper typically are an average of 400-1000 individual measurements.

Results and discussion

Reaction rates for isopropanol oxidation

The overall stoichiometry of the oxidation of isopropanol is described by the equation 4.1,

$$(CH_3)_2CHOH + \frac{1}{2}O_2 \rightarrow (CH_3)_2CO + H_2O \tag{4.1}$$

Acetone is the primary product and the only one detected in all our reactions. It is widely accepted that the reaction proceeds via dehydrogenation of the alcohol, leading to hydrogen build-up on the platinum surface. Oxygen is believed to react only secondarily with adsorbed hydrogen to form water, though it may play an important role in removing certain products of peripheral reactions which poison the surface. It has been previously demonstrated that under steady state conditions, the platinum catalyst surface is hydrogen covered[7]. A high surface concentration of oxygen can reversibly poison platinum catalysts in the alcohol oxidation reaction, presumably by blocking surface sites for adsorption of molecular alcohol.

As shown in Figure 4.3, our measurements of the rate of production of acetone with respect to increasing oxygen concentration reveal two distinct regimes delineated by the reaction order in oxygen. Below a threshold oxygen concentration, which was approximately 100 μM, the reaction rate increased as the oxygen concentration increased. Above this critical oxygen concentration the rate did not depend strongly on oxygen concentration. In this range the catalyst slowly deactivated over a period of hours. We believe that below 100 μM O_2 the reaction rate is limited by the oxygen adsorption step. We therefore assign the regions below and above the turning point in our kinetic data to oxygen-limited (0 – 100 μM) and oxygen-independent (greater than 100 μM) conditions. Figure 4.4 shows the peak activity measured for platinum catalysts at each alcohol concentration. For this plot, we take the maximum acetone production rate at the in the oxygen-independent range, because it should represent the rate of the rate limiting step on the surface without oxygen diffusion limitations as well as minimal oxygen poisoning.

In order to determine the effect of alcohol concentration on catalysis the isopropanol mole fraction was varied from zero to one. Upon increasing the mole fraction of alcohol in solution, the reaction rate is maximized at intermediate concentrations of alcohol. The highest reaction rates were obtained between 0.14 and 0.23 mole fraction of isopropanol (Figure 4.4), where the maximum turnover frequency was 64 hr^{-1}. Outside of this concentration range, the reaction rate reached only 20 hr^{-1}.

Prior publications of the dehydrogenation of alcohol on platinum have reported zero-order dependence of the reaction rate on alcohol concentration[7,8]. This is due to the fact

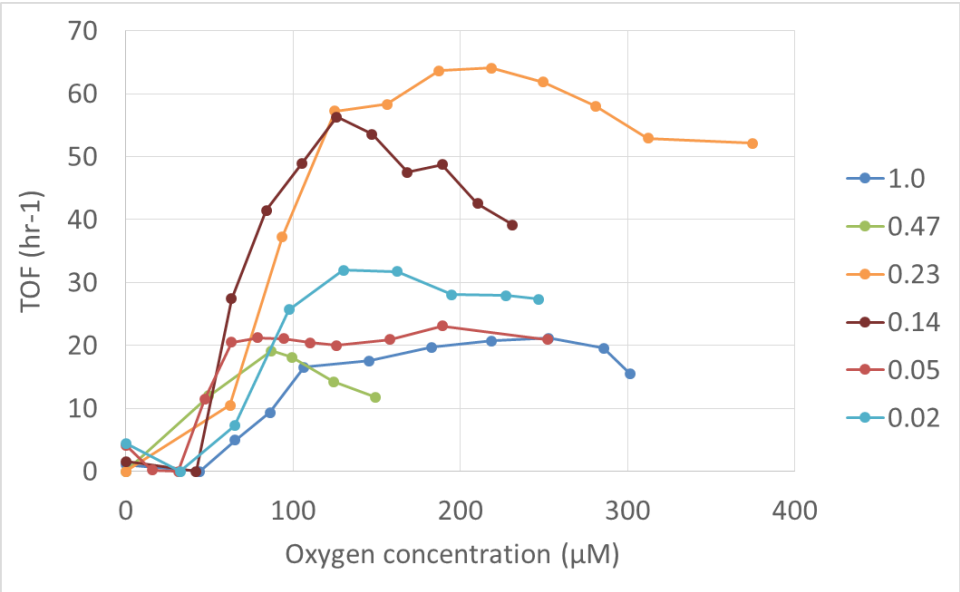

Figure 4.3: Oxygen concentration dependence of acetone production for increasing alcohol concentrations. The legend above the graph gives the mole fraction of alcohol used.

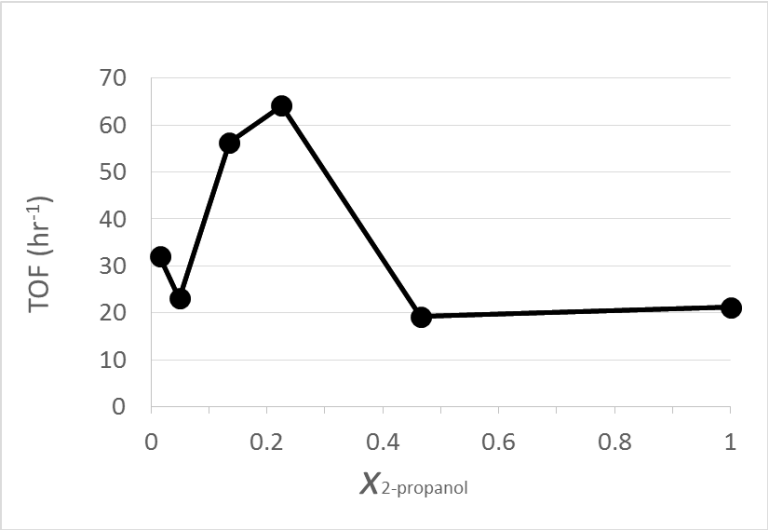

Figure 4.4: Maximum rates achieved in the oxygen-independent range for aqueous alcohol mixtures. These rates represent the rate limiting step on the surface.

that these studies were done under conditions of oxygen diffusion limitation, where the rate is controlled by the oxygen adsorption step. The data here suggest that the peak rates in this Figure 4.3 are taken beyond the oxygen-limited regime but before appreciable oxygen poisoning occurs. In contrast with previous studies however, the concentrations of alcohol used here are far higher, so that alcohol plays the role of solvent as well as reactant, and the effect we observe comes not only from a reaction order but from a change in the surface environment from water-dominated to alcohol-dominated, as we discuss below.

Sum-frequency generation of aqueous isopropanol mixtures on platinum

To illuminate the difference between the regions of low and high reaction rate in the alcohol oxidation reaction, SFG was used to characterize the conditions at the solid-liquid interface. Due to the selection rules of SFG, which preclude its occurrence in centrosymmetric and isotropic environments, SFG signal is considered to originate purely from the interfacial region[12–15]. The intensity of the sum-frequency light, can be expressed

$$I_i(\omega) \propto |\chi^{(2)}_{ijk}(\omega)|^2 I_j I_k \tag{4.2}$$

where I_j and I_k are the intensities of incident visible and infrared light, and $\chi^{(2)}_{ijk}$ is the non-linear susceptibility matrix element for the polarization directions of the incident fields. The subscripts, i, j and k denote the polarization of the SFG, visible, and IR light, respectively. The $chi^{(2)}_{ijk}$ can be further expanded as

$$\chi^{(2)}(\omega) = \frac{A_q\sqrt{\Gamma_q}}{(\omega - \omega_{0,q}) + i\Gamma_q} \tag{4.3}$$

where q represents a vibrational mode of a molecule at the interface, A_q the oscillator strength of the SFG transition, ω the frequency of the IR field, ω_0 the center frequency of a vibrational transition, Γ the width of the transition.

In the SFG experiment, as the frequency of the incident mid-IR laser pulse is tuned over a vibrational resonance of a molecule at the interface, the measured SFG intensity increases. This allows for the collection of a surface specific vibrational spectrum. Because sum-frequency generation is a coherent phenomenon, an ensemble of molecules must possess a net orientation in order to generate SFG which allows the technique to discriminate against isotropic liquids in favor of molecules interacting strongly enough with a surface to cause their organization.

The spectrum of 100% isopropanol on platinum is shown in Figure 4.5. Fitting procedures revealed the presence of four features in the SFG spectra in the region between 2850 and 3100 cm^{-1}, centered at 2863, 2921, 2955 and 2981 cm^{-1}. It is important to mention here that the mutual interference of overlapping resonances as well as interference of resonances with a non-resonant background results in features that have an "s-like" profile, rather than a Lorentzian profile (this effect is due to the change in sign in the denominator in the summed terms of equation 4.3 and is nicely summarized by Bain[16]). Therefore the center frequencies of CH_x stretching modes marked in Figure 4.5 do not correspond with a maximum or minimum in the SFG spectrum. Assignment of peaks in the SFG spectra of molecular isopropanol has been done previously[17]. Molecular isopropanol has four SFG

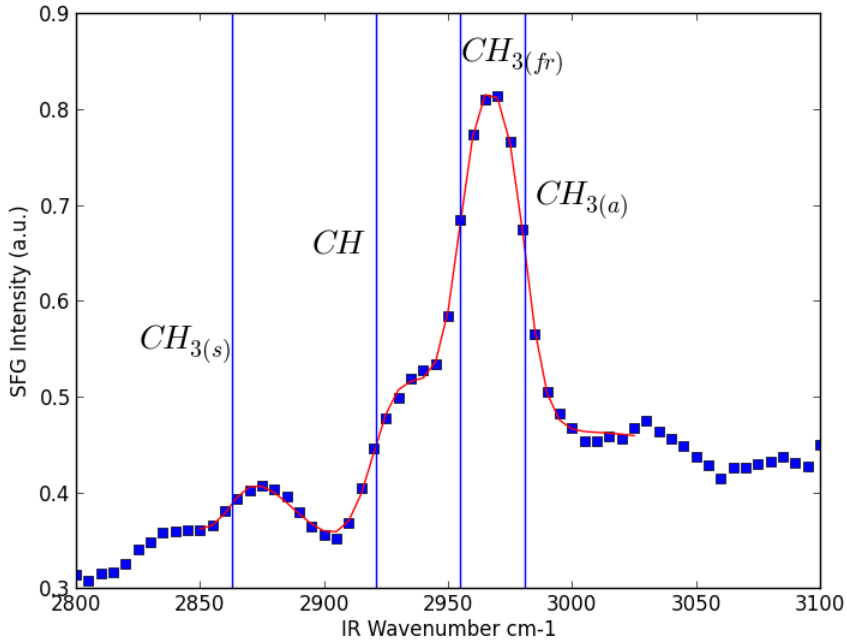

Figure 4.5: SFG spectra of pure isopropanol at the liquid/platinum interface. Fit is shown in red. The modes assigned are the CH_3 symmetric stretch (2863 cm^{-1}), CH stretch (2921 cm^{-1}), CH_3 fermi resonance (2955 cm^{-1}) and CH_3 asymmetric stretch (2981 cm $^{-1}$).

peaks centered at 2880 cm^{-1} ($CH_{3,ss}$), 2915 cm^{-1} (CH), 2941 cm^{-1} ($CH_{3,fr}$), and 2975 cm^{-1} ($CH_{3,as}$). We assign the peak at 2863, 2921, 2955 and 2981 cm^{-1} to the $CH_{3,ss}$, CH, $CH_{3,fr}$) and $CH_{3,as}$ respectively. Some shifting in the frequencies may be due to interaction with the platinum surface.

Figure 4.6 shows reference spectra of water and D_2O at the platinum surface. Due to the larger mass of the deuterium atoms in D_2O compared to H_2O, the SFG signals for this molecule are red shifted outside of the range of our instrument. The signal in the D_2O spectrum therefore reflects only the non-resonant signal from platinum. It is clear from comparing this spectrum with that of Pt/H_2O spectra that the broad dip between 3100 and 3450 cm^{-1} is from the OH stretching mode of water interfering destructively with the non-resonant background. Fitting of these spectra to equation 4.6 revealed that these dips can be deconvoluted into two broad features centered at approximately 3150 and 3450 cm^{-1}. These assignments agree well with the ice-like (3150 cm^{-1}) and liquid-like (3450 cm^{-1}) water features, which have been identified previously in spectra of water on platinum and at other interfaces[13,18–21].

While many SFG studies are used to identify surface adsorbed species on catalyst surfaces, we ascribe the CH_x resonances seen in these spectra to molecular isopropanol at the solid-liquid interface. Many studies of liquid-gas and liquid-solid interfaces have demonstrated that a covalent bond to the surface is not necessary for the high extent of ordering among molecules required to produce a non-zero SFG signal[20,22–25]. This conclusion is mainly supported by the fact that no change is observed in the spectra with oxygen concentration,

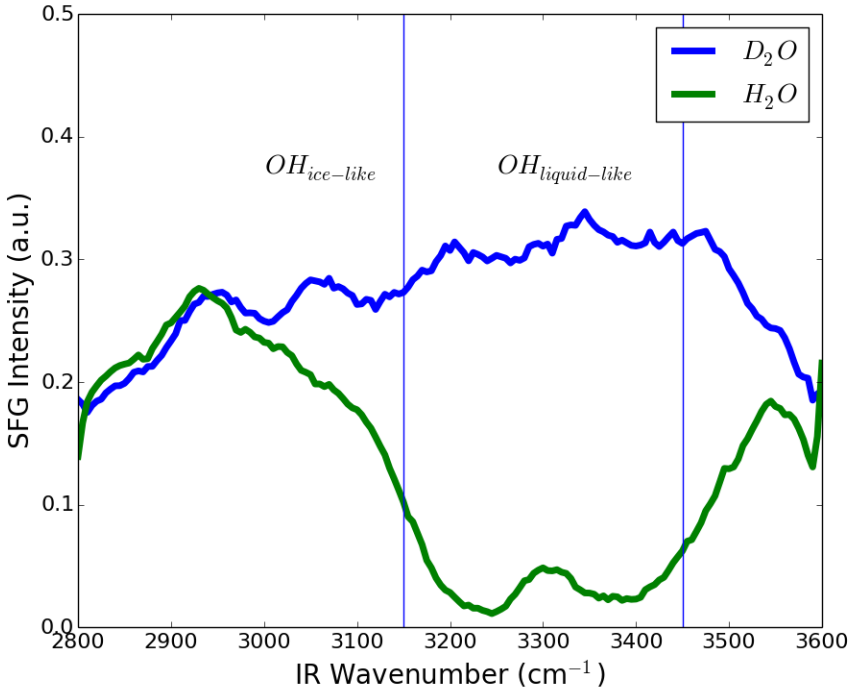

Figure 4.6: Spectra of H_2O and D_2O. The spectrum of D_2O is the background from the platinum metal, while two dips from the OH stretching modes are present in the H_2O spectrum.

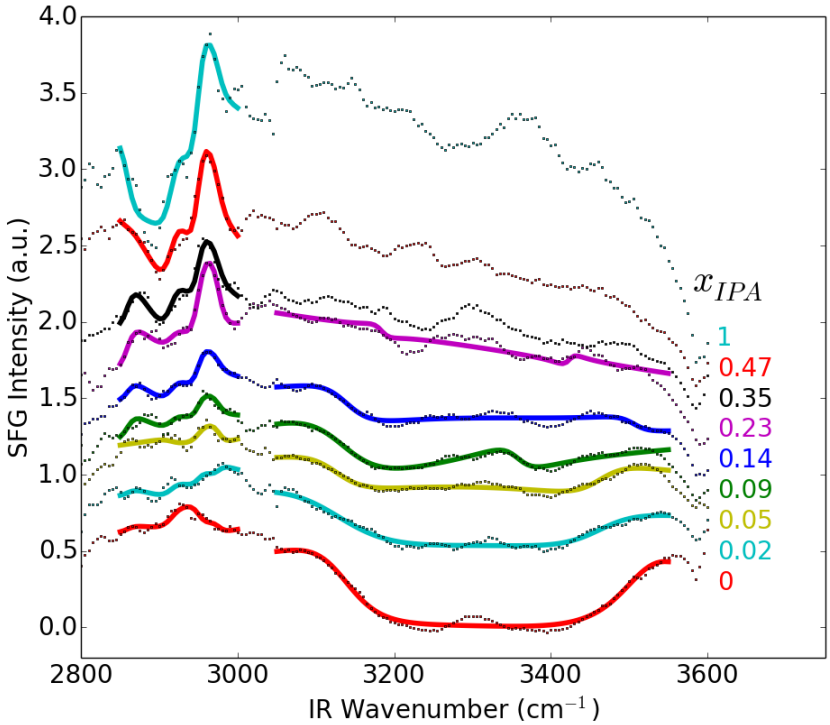

Figure 4.7: SFG spectra of the interfacial layer at varying alcohol concentration with mole fraction of isopropanol varying from 0 to 1. Thick lines are the results of the fitting procedures, which were done separately in the OH region and CH region.

despite the strong dependence of the catalyst activity on [O_2]. Also, as will be discussed below, the CH_x peaks do not show up in spectra at low alcohol concentrations although the catalyst exhibits activity.

Figure 4.7 shows SFG spectra at increasing mole fractions of isopropanol. For pure water, peaks for alcohol are absent and the features of water are intense. Upon addition of just 0.05 mole fraction isopropanol to the solution the signal from water is significantly decreased. The change in the spectra suggest that the presence of alcohol is strongly modifying the surface environment. This may be due to a decreased number density of water molecules at the surface, a lowering of the molecular orientational ordering at the interface, or both. Interestingly, the CH_x stretching modes of alcohol itself do not appear, again due to low number density or orientational order. From reaction rate measurements though, it is clear that intermediates of the oxidation reaction are present on the platinum surface. The absence of SFG spectra of these intermediates may be caused by the low surface coverage of intermediate species. Alternatively, the image dipole selection rule may render these species SFG inactive, if the transition dipole moments of their vibrational modes lie parallel to the metal surface.

At moderate concentrations of isopropanol (0.14 - 0.23 mole fraction), where the reaction rates are highest, CH_x modes become visible in the SFG spectra. The appearance of these modes reflects an increased concentration and/or ordering of IPA molecules at the platinum

surface. It is also apparent that water, though beginning to be displaced, is still present. Finally, increasing the mole fraction of isopropanol above 0.23 results in the total exclusion of water, and this threshold for total water exclusion is also the point at which the reaction rate drops.

Figure 4.8 shows A for isopropanol and water as determined by peak fitting. SFG theory states that the oscillator strength, A, is proportional to the number density of molecules at the interface (assuming a constant orientational parameter). Therefore we can use the peak intensities to gain information about the environment at the surface. While A may be positive or negative, it is the absolute value that is indicative of the number density. For isopropanol, the other fitting parameters (Γ) and (ω_0) were held constant during these fits.

Immediately apparent from Figure 4.8 is the fact that the bulk concentrations of alcohol and water do not reflect the surface environment. This result is logical considering that the surface energy of water is high compared to less polar molecules, such as isopropanol. Although our SFG spectra cannot directly identify the mechanism for the enhancement in catalyst activity between 0.14 and 0.23 mole fraction of alcohol, the coincidence of the high activity with the presence of both alcohol and water signals the importance of both molecules at the interface. It has been described in many previous publications that the surface state of platinum catalysts during alcohol oxidation by oxygen is determined by a rather delicate balance of alcohol dehydrogenation and oxygen dissociation, where some oxygen is necessary for continuous activity, but too much results in poisoning[26,27]. Thus the increase in activity seen above 0.14 mole fraction of isopropanol can be explained by the increased ability of the alcohol adsorption step to compete with O_2 adsorption kinetically. The requirement we observe for water in the first molecular layers may be due to a stabilizing effect of water on an intermediate or transition state such as is seen in some homogeneous reactions. Results similar to ours have been reported for ethanol oxidation and were explained by the increase in the adsorption energy of the reaction intermediate in water's presence[28]. A solvent effect of water in stabilization of the intermediate in aldehyde hydrogenation (the reverse reaction) was described in a previous report and investigated by computational work[29]. Alternatively, the reaction of water with adsorbed oxygen atoms to form surface hydroxyl groups may enhance the reaction rate, as the favorability of the hydroxyl form of surface oxygen (as opposed atomic oxygen or subsurface oxygen) for high activity in this reaction has already been discussed. While our data does not specifically support any one explanation, it is clear that surface concentrations of water and alcohol are crucial to obtaining the higher steady state reaction rate.

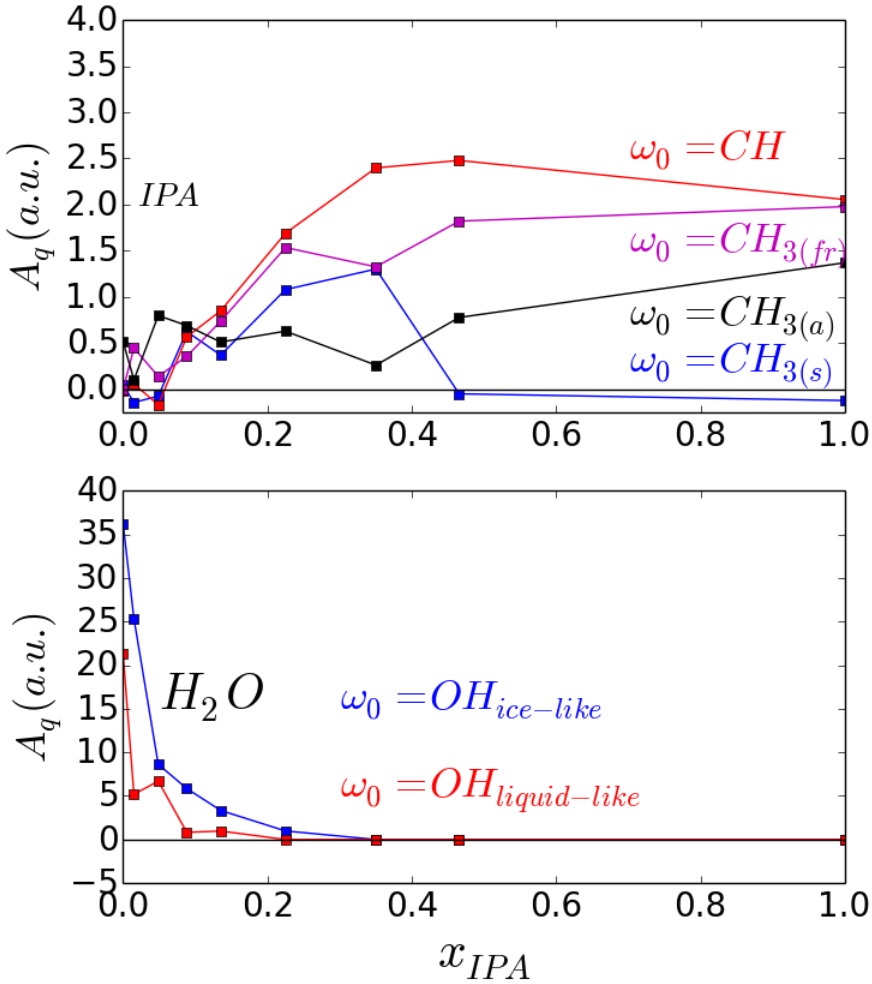

Figure 4.8: Oscillator strengths (A_q) determined for peaks of isopropanol and H_2O. The peaks in the SFG spectra were fit to equation 4.3, using four peaks for the CH region and two for the OH region. Each colored line corresponds to the vibrational mode whose center frequency (ω_0) is printed in the same color. The spectra suggest that isopropanol reaches saturation at the surface above 0.23 mole fraction and water is completely excluded from the surface.

Conclusions

Herein it is demonstrated that the catalytic activity in the heterogeneously catalyzed oxidation of isopropanol by oxygen on platinum catalysts is increased under conditions of medium alcohol concentration. Sum-frequency generation studies show that alcohol begins to dominate the interfacial region at concentrations greater than 0.14 mole fraction. At medium alcohol concentrations the interfacial region consists of both water and alcohol, and above 0.23 mole fraction, water is excluded from the surface. In both concentration extremes, the reaction rate is decreased by a factor of approximately 3. In general our SFG spectra, combined with reaction kinetics, demonstrate that the solid-liquid interfacial layer in a liquid phase heterogeneously catalyzed reaction may be quite different than suggested by the bulk concentration of the liquid solution can play a critical role in determining the reaction rate.

References

[1] Dobereiner, J. *Annalen Der Physik* **1823**,

[2] Mallat, T.; Baiker, A. *Catalysis Today* **1994**, 247.

[3] Mallat, T.; Baiker, A. *Chem. Rev.* **2004**, 3037.

[4] Besson, M.; Gallezot, P. *Catalysis Today* **2000**, 127.

[5] Gallezot, P. *Catalysis Today* **1995**, 405–418.

[6] Dirkx, J. H.; derH.S. Van, *J. Catalysis* **1981**, 1.

[7] DiCosimo, R.; Whitesides, G. *J. Phys. Chem.* **1989**, 768.

[8] Nicoletti, J.; Whitesides, G. *Journal Of Physical Chemistry* **1989**, 759–767.

[9] Thompson, C.; Carl, L.; Somorjai, G. *Journal Of Physical Chemistry C* **2013**, *49*, 26077–26083.

[10] Tokunaga, J. *J. Chem. Eng. Data* **1975**, 41.

[11] Onorato, R.; Yoon, A.; Lin, J.; Somorjai, G. *J. Phys. Chem. C* **2012**, 9947.

[12] Vogel, V.; Mullin, C.; Shen, Y. *Langmuir* **1991**, 1222.

[13] Du, Q.; Freysz, E.; Shen, Y. *Physical Review Letters* **1994**, *72*, 238–241.

[14] Lambert, A.; Davies, P.; Neivandt, D. *Appl. Spectrosc. Rev.* **2005**, 103.

[15] Shen, Y. *Nature* **1989**, *337*, 519–525.

[16] Bain, C. *J. Chem. Soc., Faraday Trans* **1995**, 1281.

[17] Kataoka, S.; Cremer, P. *J. Am. Chem. Soc.* **2006**, 5516.

[18] Brown, M.; Raymond, E.; Allen, H.; Scatena, L.; Richmond, G. *J. Phys. Chem. A* **2000**, 10220.

[19] Noguchi, H.; Okada, T.; Uosaki, K. *Electrochim. Acta.* **2008**, 6841.

[20] Hopkins, A.; Richmond, G. *App. Spectrosc.* **2013**, 261.

[21] Verreault, D.; Kurz, V.; Howell, C.; Koelsch, P. *Rev. Sci. Instrum.* **2010**, 063111.

[22] Fan, Y.; Fan, Y.; Chen, X.; Yang, L.; Cremer, P.; Gao, Y. *J. Phys. Chem. B* **2009**, 11672.

[23] Eisenthal, K. *Chem. Rev.* **1996**, 1343.

[24] Richmond, G. *Chem. Rev.* **2002**, 2693.

[25] Conboy, J.; Messmer, M.; Richmond, G. *J. Phys. Chem.* **1996**, 7617.

[26] Jelemensky, L.; Kuster, B. M.; Marin, G. *Catalysis Letters* **1995**, 269.

[27] Jelemensky, L.; Kuster, B. M.; Marin, G. *Chem. Eng. Sci.* **1996**, 1767.

[28] Chibani, S.; Michel, C.; Delbecq, F.; Pinel, C.; Besson, M. *Catal. Sci. Technol.* **2013**, 339.

[29] Akpa, B.; D'Agnostino, C.; Gladden, I.; Hindle, K.; Manyard, H.; McGregor, J.; Li, R.; Neurock, M.; Sinha, N.; Stitt, E.; Weber, D.; Zeitler, J.; Rooney, D. *J. Catal.* **2012**, 30.

Chapter 5

Ethanol oxidation on platinum catalysts studied using SFG and reaction rate measurements

This chapter describes the SFG studies of aqueous ethanol oxidation on platinum catalysts. The rate of acetaldehyde production measured as a function of alcohol concentration and oxygen concentration shows a trend similar to that of isopropanol. The rate increases with increasing oxygen concentration and levels off at high concentrations of O_2. The reaction rate is maximized at 0.15 mole fraction of ethanol and decreases above this concentration. The SFG spectra show the resonant peaks from the CH stretching modes of ethanol which increase in intensity as the bulk concentration of alcohol increases. No features from the OH stretching mode of water are seen in the SFG spectra. While the reaction rate data suggest a similarity with isopropanol oxidation, the SFG spectra suggest that alcohol does not dominate the interface as did isopropanol, and that there may be water close to the surface up to very high concentrations of alcohol. We conclude that the water may play different roles for ethanol and isopropanol oxidation or that the much better competition of ethanol with oxygen for adsorption sites could overwhelm the enhancing effect of water in the interfacial region.

Introduction

Even more so than isopropanol, the oxidation of ethanol has been extensively studied[1–5]. As a simple primary alcohol, which is very close to isopropanol (different only by a methyl group), ethanol is a good candidate to extend the studies of isopropanol oxidation presented in Chapter 4. The mechanism proposed for ethanol is analogous to that for isopropanol. However, the reaction tends to be faster for primary alcohols than for secondary ones[6,7].

This chapter discusses the study of ethanol oxidation using sum-frequency generation and reaction rate measurements. We have measured the production rate of acetaldehyde, the primary product of this reaction, as a function of oxygen concentration and ethanol concentration in solution, using the same experimental model as used in the previous chapter. The reaction rate measurements give similar kinetic results to isopropanol with a peak reaction rate achieved at 0.15 mole fraction of alcohol. The reaction rates for ethanol are about 10 times higher than those measured for isopropanol. The SFG spectra show the CH peaks of ethanol at concentrations of 0.25 mole fraction. It is difficult to compare these results with those of isopropanol directly, since the OH peaks of water were not visible in the SFG spectra in this work, and it is not possible to monitor water directly. However, the intensity of the ethanol peaks suggest that water is at the interface up to very high concentration

of ethanol. The correlation seen for isopropanol between the reaction rate decline and the exclusion of water is not as strong for ethanol which suggests a possible difference in the role of water in these two reactions.

Experimental details

Catalyst preparation

The catalyst used was a 5 nm electron-beam evaporated film of platinum on a polycrystalline quartz substrate. Quartz substrates were cleaned using No-Chromix mixture followed by heavy washing with deionized water. During the evaporation, the base pressure of the chamber was $1x10^{-6}$ Torr. A 2 nm adhesion layer of titanium was used to improve wetting by platinum on the quartz surface and increased stability of the film toward delamination and laser ablation. Samples were heated to 300 °C in air to remove carbon monoxide from previous reactions. The sample was then installed in the reaction cell and reduced *in situ* at 80 °C for one hour in pure hydrogen flow. At this point the temperature was reduced to 30 °C, and the cell was filled with liquid reactant without exposing the catalyst to air. The reaction was started by initiating magnetic stirring.

Reaction rate measurements

The setup used for reaction rate studies and sum-frequency generation was the same as that described in the previous chapter on isopropanol oxidation[8]. The reactor cell was a completely enclosed (sealed to air) Teflon reservoir with inlet and outlet tubes of 1/16 inch OD stainless steel tubes. Reactant mixtures of ethanol (Chomasolv HPLC grade non-denatured, used as received without any further purification) and water (triple distilled 18 MΩ) were equilibrated with a mixture of air (or oxygen) and nitrogen by vigorous bubbling of the gas mixture through the liquid. The volume fraction of air(oxygen) with nitrogen was controlled using calibrated mass flow controllers with a total flow rate of 20-40 sccm/min, and the partial pressure of oxygen above the liquid was verified using a Clark electrode. Using the gas solubility for oxygen in aqueous ethanol mixtures and the densities of those mixtures as shown in Figure 5.1 the dissolved oxygen could be calculated[9]. The liquid flow rate was controlled with a peristaltic pump using platinum cured silicone tubing placed after the cell, so as not to allow oxygen transfer through the silicone tubing which has a high gas permeability. The flow rate for ethanol oxidation experiments was kept at 80 μL/minute. The residence time at 80 μL/minute was approximately 9 minutes. The reaction temperature was kept at 30 °C. The concentration of product (acetaldehyde) was measured using calibrated dynamic vapor phase sampling of the liquid and gas chromatography as described in Chapter 3.

In a typical rate experiment, the liquid entering the flow cell initially contained a very low concentration of oxygen (25 μM). The reaction displayed an induction period on the order of 1 hour, after which the catalyst became active. The catalyst activity could be monitored until it was stable for at least 45 minutes, indicating that the reaction had reached a steady state. At this point the oxygen concentration in the liquid was increased at 12.5 μM increments, allowing the reaction to reach steady state between each interval. In the low oxygen regime, this resulted in a stepping up of the reaction rate with agrees with

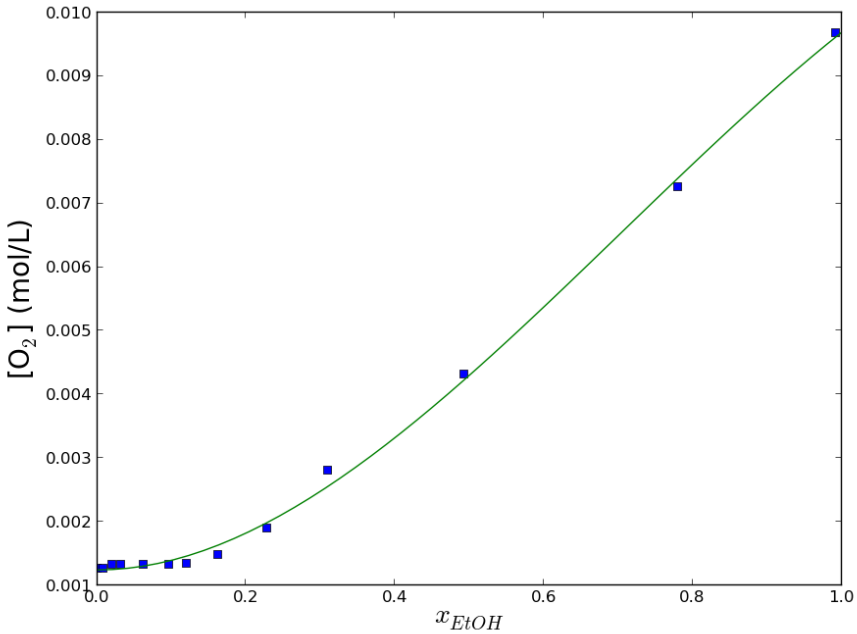

Figure 5.1: Oxygen solubility in ethanol/water mixtures and the fit used to calculate O_2 solubility in this work.

expectations based on theories of diffusion, where the flux to a surface is proportional to the concentration gradient. We should point out that we are not referring to bulk diffusion of oxygen, since the cell was well stirred and no dependence on stirring rate was observed near the applied stir rate, but rather the diffusion of oxygen across the shear layer. At the point where the oxygen adsorption was no longer the rate limiting step, a plateau of the reaction rate was observed. Increases in the oxygen concentration resulted either in no change in the rate or slight deactivation.

SFG measurements

Sum-frequency generation was carried out by optically coupling the quartz slide to a CaF_2 equilateral prism. Mid-IR (2800-3600 cm^{-1}) and visible (532 nm) pulses generated by OPG/OPA and frequency doubling, respectively, pumped with the output of a Nd:YAG laser (Continuum Leopard D10, 20 ps, 20 Hz, 10.3 mJ/pulse), were incident on the platinum surface from the backside at 45° and 62°, respectively. Sum-frequency light was detected in the reflected direction using a photomultiplier tube after filtering of the Rayleigh and Stokes-Raman scattered green light. Triggered gated integration (Stanford Research Systems, 200 ns gate time) was used to increase signal to noise. Data points in these spectra in this chapter are typically the average of 1000 or more measurements.

Results and discussion

Kinetic measurements of ethanol oxidation on platinum

The primary product of ethanol oxidation is acetaldehyde. The overall stoichiometry of the reaction is

$$CH_3CH_2OH + 1/2O_2 \rightarrow CH_3CHO + H_2O \tag{5.1}$$

It has been demonstrated many times that the reaction of alcohol oxidation is susceptible to "over-oxidation", the term used to describe the inhibition of the reaction by too high a surface coverage of oxygen. It is commonly believed that this is due to competitive adsorption of ethanol and oxygen[6,7,10–14]. The reaction is usually run for this reason in the oxygen diffusion limited regime, where the reaction rate is determined by the rate of oxygen molecules reaching the surface. This prevents an accurate determination of the inherent kinetic rate of the reaction. Running the reaction at oxygen concentrations too high, however, results in the poisoning of the surface, which also prevents the accurate determination of the rate. One advantage of using a flow cell reactor (over a using a batch reactor) is the ease with which catalyst deactivation can be detected and measured. In a batch cell, where the reaction rate is extracted as the time derivative of the product concentration, slow, steady decreases in this derivative are difficult to track. In a flow reactor, on the other hand, deactivation is directly seen as a decrease in the product concentration of the effluent mixture, which is easily and instantaneously detected.

The measurement of reaction rates of the oxidation of ethanol to acetaldehyde showed that the reaction of ethanol is very similar to isopropanol qualitatively. After hydrogen pretreatment, the catalyst shows no activity for 60-120 minutes before the oxidation reaction ensues. After this time the reaction rate increases with increasing oxygen concentration. Compared with what was observed in isopropanol oxidation, the catalyst is highly resistant toward oxygen poisoning. Where isopropanol oxidation rates would reach maxima at approximately 100 μM/L ethanol oxidation increases in rate up to 1 mM O_2 - nearly the maximum soluble oxygen concentration in water. This can be justified with the overall higher reaction rates observed (measured as acetaldehyde production), which are about 10 times higher. Either ethanol adsorbs much faster on the interface than isopropanol, or the faster limiting rate causes faster oxygen removal in the form of water. In chapter 6 a reaction mechanism is described in which adsorbed oxygen acts as a hydrogen acceptor from the ethoxy species. The removal of oxygen in this way could have the effect of increasing stability toward oxygen poisoning. In Figure 5.2 the steady state reaction rates for water/ethanol mixtures is shown as a function of oxygen concentration, and Figure 5.3 shows the maximum rates reached for each ethanol concentration.

As seen for isopropanol, ethanol oxidation exhibits a peak in the kinetic reaction rate achieved at a relatively low alcohol concentration. We attributed this to an optimization of two factors, the alcohol concentration at the interface and the amount of water at the interface. Increasing the amount of alcohol increases the adsorption rate of alcohol onto the surface, helping it compete with oxygen adsorption and increasing the amount if reactive intermediate on the surface. This is true, though, only up to a certain point where water is totally excluded from the interface, and the rate decreases due to the lack of stabilization of

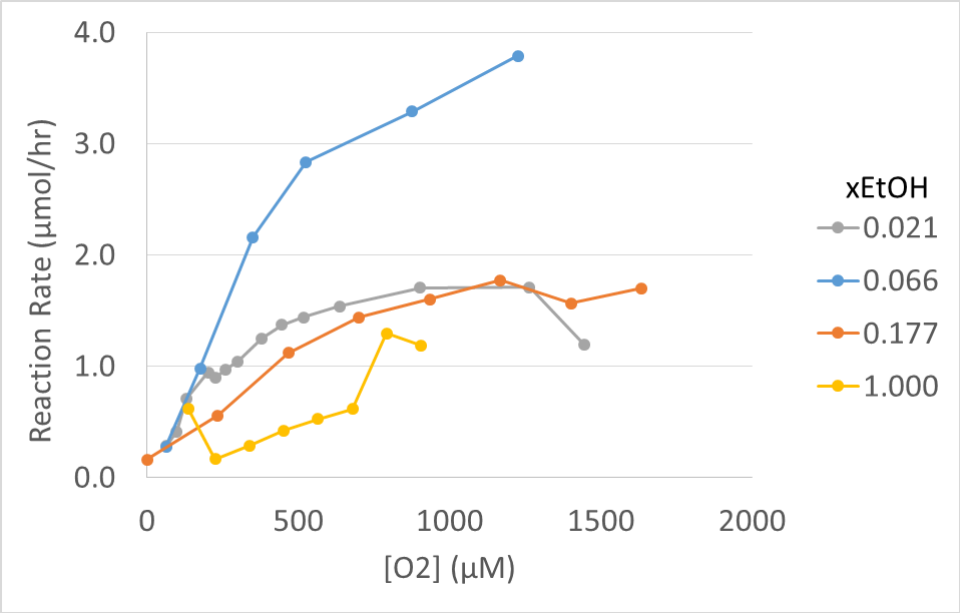

Figure 5.2: Oxygen concentration dependence of acetaldehyde production for increasing alcohol concentrations. The legend gives the mole fraction of alcohol used.

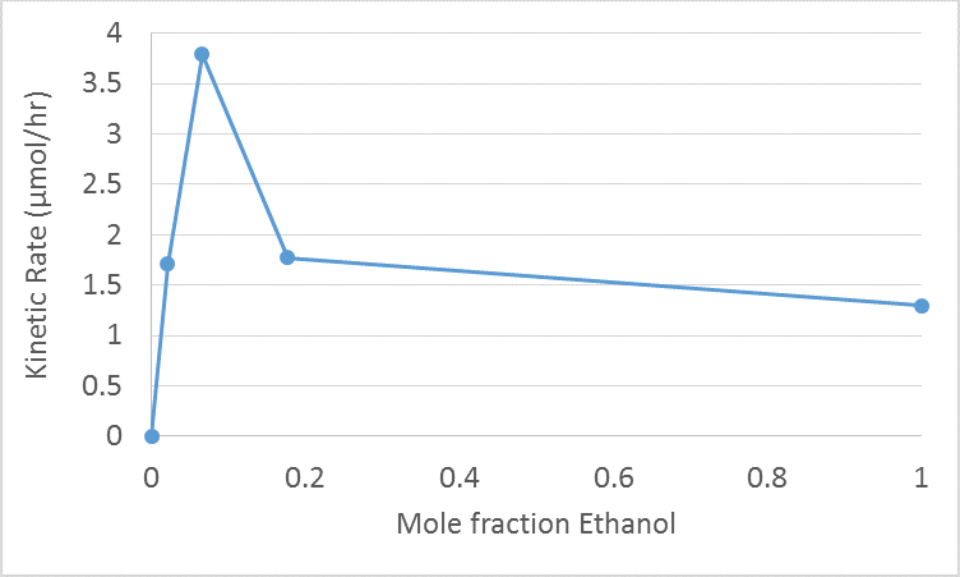

Figure 5.3: Kinetic reaction rate for ethanol oxidation for ethanol concentrations of 0, 0.021, 0.066, 0.177 and 1.0. The maximum rate observed with respect to oxygen concentration corresponds to the true kinetic rate.

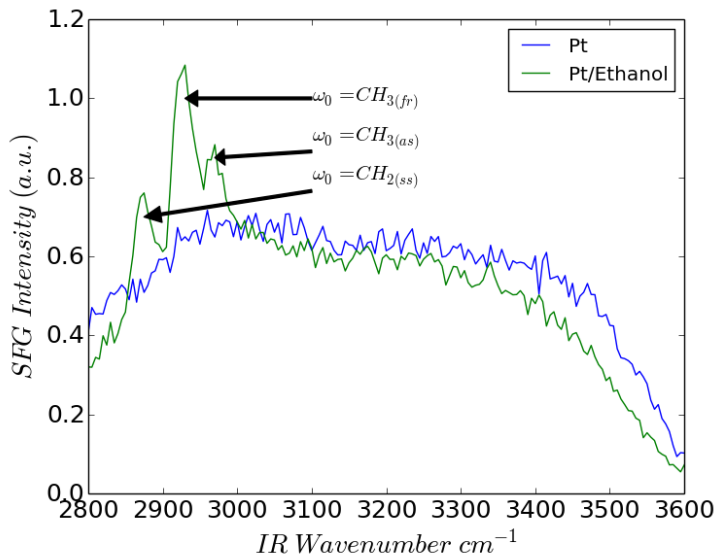

Figure 5.4: SFG spectra of the platinum/H_2 and platinum/ethanol interfaces in the gas phase. The ethanol spectrum shows the resonances assigned to the $CH_{3,fr}$, CH_2 symmetric and CH_3 asymmetric modes.

a transition state or intermediate by water.

SFG of ethanol and aqueous ethanol mixtures on platinum

The spectrum of ethanol on platinum in the gas phase was collected to serve as a reference for the spectra in the liquid phase. Figure 5.4 shows the spectra of clean platinum (in hydrogen) and ethanol on platinum, generated by placing a drop of ethanol in the reactor cell (without contact of the liquid and platinum). The reference spectrum of Pt/H_2 shows that the non-resonant signal from the metal platinum is strong. Upon adsorption of ethanol three major resonant features are observed at 2880 cm^{-1}, 2935 cm^{-1} and 2975 cm^{-1}. These correspond well to the already assigned CH stretching peaks of molecular ethanol by comparing various deuterium substituted ethanols. The peak at 2935 cm^{-1} corresponds to the $CH_{3,fr}$ stretch while the peaks at 2880 cm^{-1} and 2975 cm^{-1} are from the CH_2 symmetric and CH_3 asymmetric stretches.

SFG spectra of pure ethanol liquid at the surface of platinum show similar peaks, but are different in their spectral shapes. Figure 5.5 is the SFG spectrum of pure liquid ethanol on platinum. Again, the non-resonant signal from the platinum thin film is notable in these spectra. Like the resonant features of isopropanol, it is clear that the coherent nature of SFG causes the peaks of ethanol to destructively interfere with the signal of platinum. Careful fitting is necessary to extract proper peak parameters from the data. Peak fitting was performed using the typical Lorentzian peak shape described by

$$\chi^{(2)}(\omega) = \frac{A/\sqrt{\Gamma}}{(\omega - \omega_0) + i\Gamma}$$

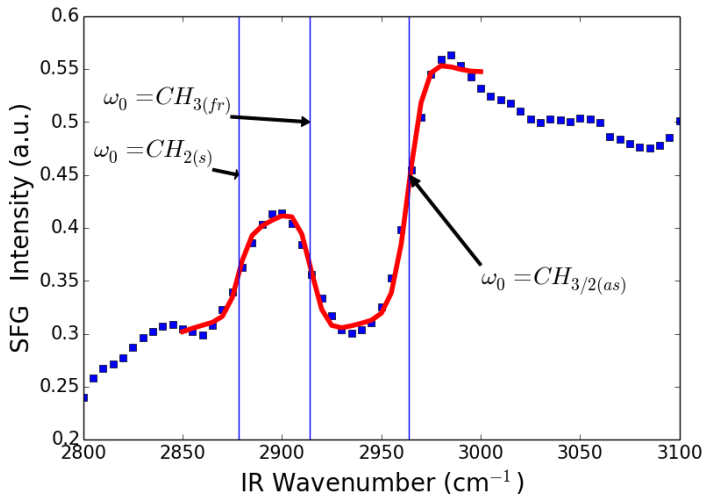

Figure 5.5: Spectrum and overlaid fit of pure ethanol on platinum. The resonant features can be assigned to the CH stretching modes of ethanol.

ω_0	A	Γ
2878	-0.44	9
2914	-1.11	12
2964	1.98	13.8

Table 5.1: Fitting parameters for pure ethanol on platinum. These values correspond to the red line in Figure 5.5

where A represents oscillator strength of the transition, ω_0 the central resonance frequency and Γ the linewidth[15–18]. Fitting of the pure ethanol spectrum gives the centers of three peaks at 2878 cm^{-1}, 2914 cm^{-1} and 2964 cm^{-1}, which agree very well with the spectrum of gaseous ethanol and the literature values[19]. It should be noted here that based on previous work by other groups which indicate that the non-linear response of platinum is purely real we have set its phase to zero[20]. The parameters obtained by fitting of the spectrum of pure alcohol are tabulated in Table 5.1.

Performing SFG under conditions of varying alcohol concentration, the peaks of ethanol can be seen to increase with increasing alcohol mole fraction. Figure 5.6 shows the SFG spectra of aqueous ethanol mixtures from $x_{EtOH} = 0$ to $x_{EtOH} = 1$. At low concentration of ethanol (less than 0.25 mole fraction) no peaks are seen at the surface. Unlike previous studies with isopropanol, the OH peaks from water are not visible at the interface during the ethanol oxidation reaction. This could be due to a stronger interaction between water in solution and the ethanol, which is generally more hydrophilic. Alternatively, the surface of platinum could be rendered more hydrophobic by the adsorption of more organic species on its surface. Hydrophilic surfaces can strongly orient water and it is known that water possesses a much lower overall signal at hydrophobic interfaces than at hydrophilic ones[21,22].

Although the OH peaks are not visible at the platinum surface, the CH peaks of ethanol are present and increase in intensity with the increasing concentration of alcohol. The trends in the spectra seen here show qualitative agreement with the previous studies of isopropanol, where, at very low mole fractions of alcohol, the alcohol molecules are not seen in the SFG spectra, but at a critical concentration, they appear, and continue to grow in amplitude up to 100% ethanol. Analogous to isopropanol, ethanol peaks are not always present even though the catalyst is active according to kinetic measurements, and the SFG peaks do not change with oxygen concentration, despite a changing reaction rate being clearly observed. Therefore we deduce that for ethanol as well as isopropanol, the SFG resonances seen in our spectra do not belong to the active intermediate in the oxidation reaction, but rather to the molecular ethanol in the interfacial region directly near the platinum surface. Another possible assignment for the CH peaks seen in the SFG spectra would be spectator species with both a CH_2 group and CH_3 group, which is inactive in the reaction. We have determined this to be unlikely through experiments demonstrating that the peaks seen in pure alcohol quickly disappear after flushing the reaction cell with water. The short lifetime of the SFG active species at the interface makes them more likely to be a non-bonded species than a long-lived surface spectator.

This point brings up an important distinction between the study by SFG of liquid-phase catalysis and the study of gas phase catalysis. In the gas phase, it is straightforward to attribute the peaks of SFG spectra to adsorbates on the metal surface, because although there may exist gas phase molecules in the vicinity of the surface, the number of those is very small compared to the number of molecules adsorbed to the surface. This is due to the low density of the gas phase and the large difference in the energy of physisorption and chemisorption. In the liquid phase on the other hand, the density of molecules at the interface that are not chemisorbed is very high ($\sim$1000 times higher than in the gas phase), and the molecules may adopt a strongly ordered ensemble orientation in order to lower the total surface energy of the system. Usually this preference is explained as the interaction of a hydrophilic group with the more hydrophilic phase. This type of ordering has been observed in many systems, not limited to the orientation of water and isopropanol at the liquid-gas interface, water at the solid-liquid interface, and the strong ordering of surfactants at surfaces[23,24]. Therefore due to the low sensitivity to reaction conditions of the SFG which have a strong effect on the activity of the catalyst and the lack of observed SFG signal under conditions of high catalytic activity, we ascribe the peaks in the SFG spectra to a highly ordered molecular layer at the solid-liquid interface which is not chemisorbed to the surface.

The oscillator strengths, A, for the CH_3 symmetric and asymmetric stretch modes are plotted in Figure 5.7. According to SFG theory, assuming a constant orientation of the molecules at the surface, the oscillator strength is proportional to,N , the number density of molecules at the surface. The number of ethanol molecules in the interfacial region as inferred from the inensity of SFG peaks increases as the concentration of alcohol in the bulk increases. In the isopropanol SFG spectra, the total exclusion of water from the platinum surface was accompanied by the saturation of the signal from isopropanol, indicating a maximum concentration of alcohol reached at the interface. The SFG spectra of ethanol do not suggest such a saturation; instead the peaks continue to increase in intensity up to pure alcohol. One reason for this may be the higher surface energy of ethanol compared to isopropanol. Ethanol would compete less effectively with water for the surface, making

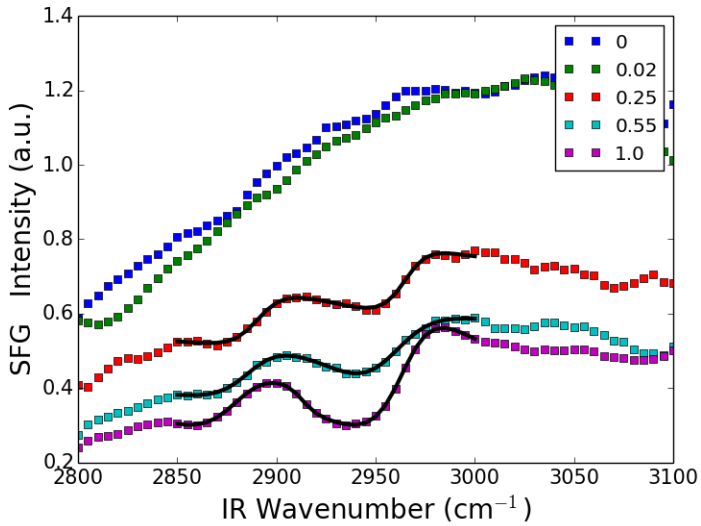

Figure 5.6: SFG spectra of the platinum/liquid interface for increasing concentrations of ethanol in water. The concentrations of ethanol are x_{EtOH} = 0, 0.02, 0.25, 0.55 and 1. Fits are shown in black.

x_{EtOH}	ω_0	A	Γ
0	No peaks found		
0.02	No peaks found		
0.25	2890	-1.56	20
	2965	1.55	18
0.55	2886	-2.09	25
	2937	-2.39	40
	2960	4.18	31
1.0	2880	-3.46	27
	2913	-.45	12
	2965	5.52	24

Table 5.2: Fitting parameters for SFG peaks of ethanol/water mixtures (x_{EtOH}= 0, 0.02, 0.25, 0.5, 1.0) on platinum. These values correspond to the spectra in Figure 5.6. Parameters for resonant features varied in the fits were the oscillator strength (A), center frequency (ω_0), the peak width (Γ). The background susceptibility was modeled as a linear function in frequency with parameter for the slope and intercept. These parameters are not shown.

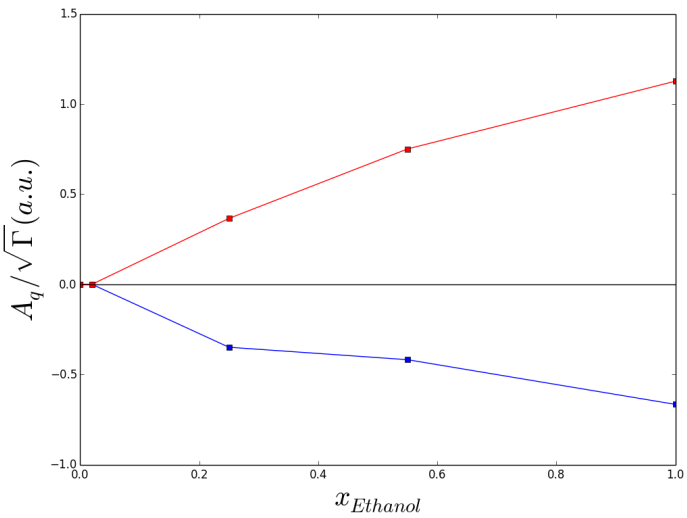

Figure 5.7: Oscillator strengths for the CH_3 group as determined by spectral fitting for mole fractions of ethanol 0, 0.02, 0.25, 0.55, and 1.0. The sign of the oscillator strength is indicative of the phase of the transition.

it unable to displace water at such a low concentration as alcohol. Unfortunately, it is not possible to verify the displacement of water (or lack thereof) due to the absence of the water peaks in the SFG spectra.

As the decline in the rate of ethanol oxidation is seen where water still exists at the interface, the stabilization of a transition state or intermediate that was suggested in the isopropanol studies in the previous chapter may not apply to ethanol oxidation. This could be due to different rate limiting steps in the two reactions, where water helps to enhance the rate limiting step of isopropanol, but not of ethanol. Alternatively, water could enhance the removal of a long lived species on the surface whose formation is faster from ethanol than from isopropanol. In the case of ethanol, which is more active on the catalyst surface, the rate enhancement by water (which was approximately a factor of three) may not be enough to slow surface poisoning by this adsorbate.

Conclusions

The investigation of ethanol oxidation and comparison to isopropanol oxidation reveals that while the kinetics of these reactions display similar patterns - with a maximum rate reached at intermediate alcohol concentrations in water - the SFG measurements yield different results. The reaction rates measured for ethanol oxidation to acetaldehyde are almost a factor of ten higher than those seen for acetone production from IPA. The catalyst is much more robust toward oxygen poisoning and can remain active up to the maximum oxygen concentration in water ($\sim$ 1 mM). The robustness is attributed to a better competition of ethanol with oxygen on the platinum surface (faster adsorption by ethanol). SFG spectra of the platinum/liquid interface under ethanol oxidation conditions do not show the spectral features of water as did the spectra of IPA/water mixtures, which could come from a high amount of alkoxy

species on the surface, causing water to be largely disordered at the surface. The intensities of CH stretching peaks from alcohol increase with alcohol concentration all the way up to pure alcohol suggesting that water may be present at the interface in all conditions up to that point and the connection of total water exclusion with a decline in reaction rate does not appear to be as strong for ethanol as for isopropanol. This may be evidence that ethanol and isopropanol have different rate limiting steps in their oxidation reactions, for only one of which water acts to enhance the rate.

References

[1] Jelemensky, L.; Kuster, B. M.; Marin, G. *Catalysis Letters* **1995**, 269.

[2] Jelemensky, L.; Kuster, B. M.; Marin, G. *Chem. Eng. Sci.* **1996**, 1767.

[3] Bozzini, B.; Abyaneh, M.; Busson, B.; De, G.; Gregoratti, L.; Humbert, C.; Amati, M.; Mele, C.; Tadjeddine, A. *J. Power Sources* **2013**, 6.

[4] van den Tillaart, J.; Kuster, B.; Marin, G. *Applied Catalysis A* **1994**, 127–145.

[5] Gomes, J.; Bergamaski, K.; Pinto, M. S.; Miranda, P. *J. Catal.* **2013**, 67.

[6] Mallat, T.; Baiker, A. *Catalysis Today* **1994**, 247.

[7] Mallat, T.; Baiker, A. *Chem. Rev.* **2004**, 3037.

[8] Thompson, C.; Carl, L.; Somorjai, G. *Journal Of Physical Chemistry C* **2013**, *49*, 26077–26083.

[9] Battino, R.; Rettich, T.; Tominaga, T. *J. Phys. Chem. Ref. Data* **1983**, *12*, 163–178.

[10] Besson, M.; Gallezot, P. *Catalysis Today* **2000**, 127.

[11] Gallezot, P. *Catalysis Today* **1997**, 405–418.

[12] Dirkx, J. H.; derH.S. Van, *J. Catalysis* **1981**, 1.

[13] DiCosimo, R.; Whitesides, G. *J. Phys. Chem.* **1989**, 768.

[14] Nicoletti, J.; Whitesides, G. *Journal Of Physical Chemistry* **1989**, 759–767.

[15] Vogel, V.; Mullin, C.; Shen, Y. *Langmuir* **1991**, 1222.

[16] Du, Q.; Freysz, E.; Shen, Y. *Physical Review Letters* **1994**, *72*, 238–241.

[17] Lambert, A.; Davies, P.; Neivandt, D. *Appl. Spectrosc. Rev.* **2005**, 103.

[18] Shen, Y. *Nature* **1989**, *337*, 519–525.

[19] Yu, Y.; Lin, K.; Zhou, X.; Wang, H.; Liu, S.; Ma, X. *J. Phys. Chem. C* **2007**, 8971–8978.

[20] Tadjeddine, A.; Le Rille, A.; Pluchery, O.; Vidal, F.; Zheng, W.; Peremans, A. *Physica Status Solidi A-Applied Research* **1999**, *175*, 89–107.

[21] Shen, Y. *Surface Science* **1994**, *299*, 551–562.

[22] Holinga, G.; York, R.; Onorato, R.; Thompson, C.; Webb, N.; Yoon, A.; Somorjai, G. *J. Am. Chem. Soc.* **2011**, 6243.

[23] Richmond, G. *Chem. Rev.* **2002**, 2693.

[24] Kataoka, S.; Cremer, P. *J. Am. Chem. Soc.* **2006**, 5516.

Chapter 6

Investigation of induction behavior in ethanol oxidation using non-resonant SFG to monitor oxygen adsorption on the surface

Introduction

This chapter discusses the phenomenon of induction in the alcohol oxidation on platinum, i.e. the switch from an inactive catalyst state to an active state. Single step reactions typically are of positive order in their rate. That is,

$$-\frac{d[A]}{dt} \propto k[A]^n,\ n > 0 \tag{6.1}$$

This can be considered negative feedback, since the production of A via other elementary steps causes the consumption of A to increase. When a reaction (heterogeneously catalyzed or otherwise) has a complex reaction mechanism made of multiple steps, the combination of these may cause positive feedback, which can result in multiple steady-state rates. In heterogeneous catalysis this can be envisioned as a shift from one surface state to another. The textbook case described is that of autocatalysis[1], where a reaction product has the effect of increasing or decreasing the reaction rate. In the reaction,

$$A \rightarrow B$$

where the rate constant, k, has a dependence on $[B]$, such that,

$$k = k' \cdot f([B])$$

an induction period may be observed, where the build-up of a concentration of B is necessary to accomplish a high rate in the conversion of A to B. In heterogeneous catalysis, one concrete example of this type of feedback is the case of Langmuir-Hinshelwood kinetics where free surface sites are made available by the desorption of adsorbed intermediates.

$$A * + B * 2* \rightarrow products + 4* \tag{6.2}$$

Induction periods also can involve the oxidation or reduction of a catalyst which often occurs as a side reaction to the oxidation or reduction of a reactant.

While sum-frequency generation is often applied to study organic molecules by their resonant SFG responses non-resonant SFG can also be produced as a result of the interaction of the incident fields with conduction electrons. In dielectric materials, like silica or calcium fluoride, the non-resonant background is negligible, but if a metal surface is present in the

probing volume the SFG signal can have a large non-resonant feature. The signal comes from the interaction of the electric fields with the surface electrons in the metal, and it can be modified by adsorption of molecules to the surface, which tends to localize those electrons[2,3]. Non-resonant SFG can complement resonant SFG features in serving as a probe of the adsorption of molecules on the surface.

The results of this work shed light on the role of oxygen in the alcohol oxidation reaction as well as the pathway by which the rate limiting step (abstraction the of second hydrogen atom) may be achieved under reaction conditions. Both of these points are not completely understood despite their being fundamental parts of the alcohol oxidation reaction. We show that while the use of SFG to monitor surface oxidation is not frequently reported, it may be a valuable tool for *in situ* liquid-phase studies, where monitoring the oxygen coverage of a surface of a metal with a strong non-resonant SFG signal is of interest[4].

Experimental details

Catalyst preparation

Platinum catalysts were 5 nm thin films deposited on a silica substrate. A 2 nm titanium adhesion layer was deposited to improve the coverage of platinum and the stability of the film toward laser damage and delamination. Before reaction the catalysts were heated for 30 minutes at 300 °C in air to remove carbon monoxide and adventitious surface species. The catalysts would then be installed in the reactor cell and reduced in situ for one hour at 80 °C in pure H_2.

Reaction rate measurements

Reactions were always carried out at 30 °C, flowing at 80 μL/minute with magnetic stirring. After the catalyst pretreatement described above, liquid was flowed through the cell without exposing the catalyst to air unless called for by the experiment.The ethanol concentration used was 217 μM (1% w/w). The liquid was flowed through stainless steel tubing from a reservoir of liquid which was brought to equilibrium with a mixture of air and nitrogen to control the dissolved oxygen concentration. Henry's constants were obtained from Battino *et al.*[5]. Acetaldehyde yield was measured by gas chromatography of the vapors above the effluent liquid with 15 minute runs using a Hayasep-T packed column. The length of the induction period was taken as the difference between the reaction starting time and the last measurement with no detected acetaldehyde.

SFG measurements

SFG was carried out using a Nd:YAG laser (20 ps, 20 Hz,) which pumped a system of non-linear crystals to produce pulsed of 532 nm light and mid-IR light, which was tunable between 2800 and 3600 cm^{-1}. These pulses were overlapped spatially and temporally on the surface and reflected SFG was collected using a photomultiplier tube. Pulse energies used were 130 μJ/pulse (green) and 280 μJ/pulse (IR). The system is described in more detail elsewhere[6].

Kinetic modelling

Kinetic modelling was carried out using a numerical method in the Python programming language. The procedure calculated the change in concentration of surface species with small time steps. The width of the time step was controlled in each step so that changes in the surface concentrations were less than 0.001 monolayer per iteration step, thus avoiding major concentration oscillations.

Results and discussion

Reaction rate results

An induction period for the reaction between 1 and 2 hours was obtained for all concentrations of oxygen between 10 μM and 310 μM. Following this induction period the reaction rate increased over a period of approximately 1 hour until it reached a steady state. A typical reaction run demonstrating the induction time is shown in Figure 6.

The induction time shows a clear inverse dependence on the oxygen concentration which strongly points to an oxidation process occurring in the induction period (Figure 6.2). Futher, flushing the cell before introducing the reaction mixture with a gaseous mixture of helium and oxygen in order to pre-cover the catalyst with oxygen caused the induction period to be eliminated, but fast deactivation (decreasing activity) was then observed. The effect of flushing the catalyst with water containing oxygen and no ethanol was the same. The state of the catalyst surface after the reductive pretreatment immediately preceding the reaction should be oxygen poor. Due to the high ratio of alcohol to oxygen in solution the surface is expected to be covered in alkoxy species and hydrogen, a byproduct of the dehydrogenation. It is well known that oxygen and ethanol compete for adsorption sites on the platinum surface during reaction. "Over-oxidation" is a common cause of reversible poisoning in this reaction, and apparently a high surface coverage of alcohol will also cause low activity.

Although electron microscopy and XPS results indicated that 5 nm of platinum was enough to completely cover the titanium adhesion layer, the same experiment was performed using a very thick (20 nm) platinum film in order to rule out an effect of the titanium adhesion layer on the catalytic activity. At this thickness, SFG experiments were impossible, but the reaction rate measurements revealed an induction period in this sample as well.

Non-resonant SFG results

SFG spectra of the catalyst surface at 1% alcohol are dominated by the non-resonant signal from platinum. For ethanol, CH_x peaks are not observed until the alcohol concentration reaches ∼35% w/w. In previous studies, we observed similar behavior for isopropanol, the resonant features of which were not seen in SFG spectra until the concentration was greater than 15% w/w. The shape of the platinum spectrum approximates the IR intensity spectrum, but more precisely it is a convolution of the non-resonant susceptibility, the incident IR intensity, the beam overlap (in scanning SFG instruments the beam path of the IR is modified slightly with frequency due to the rotation of frequency mixing crystals used to generate the IR), and Fresnel factor effects - all of which are constant from spectrum to spectrum.

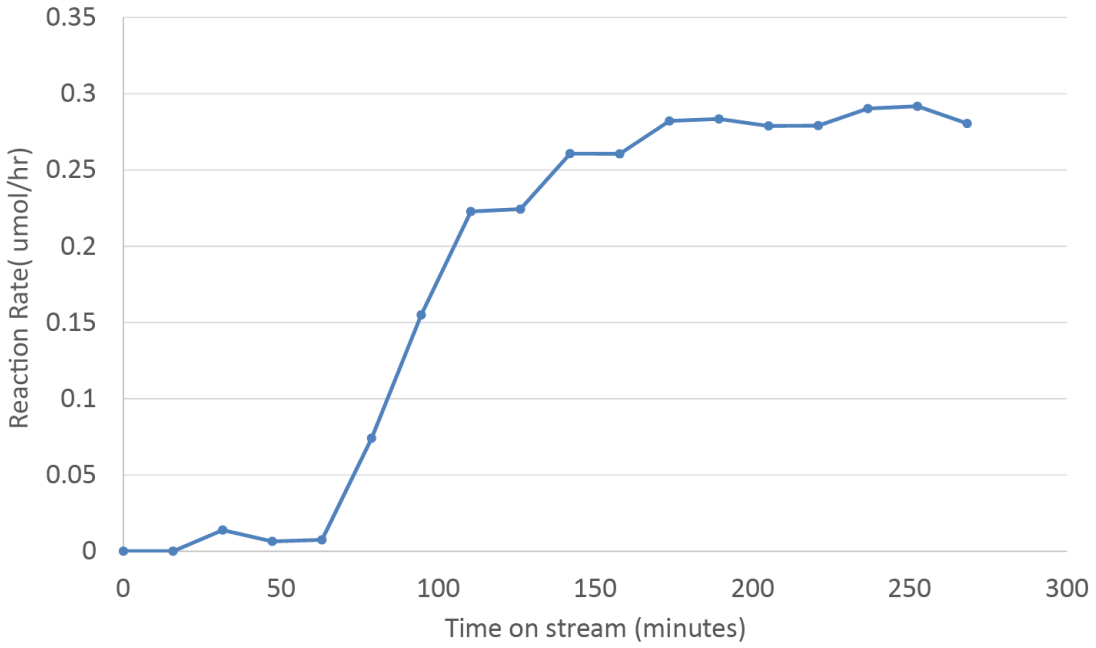

Figure 6.1: Reaction rates for ethanol oxidation to acetaldehyde as measured in the flow mode. The induction period exists in the first 60 minutes of reaction, followed by an increase in the acetaldehyde production rate. Conditions: 217 mM ethanol in water, 160 μM O_2, 30 °C.

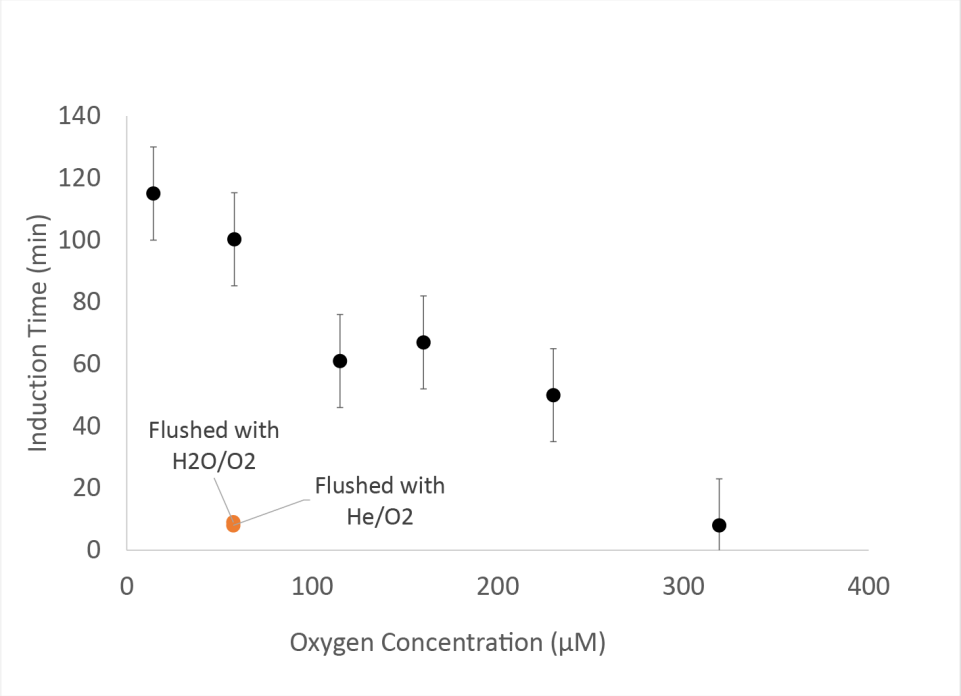

Figure 6.2: The induction time as a function of oxygen concentration in the solution for mixtures of ethanol in water. Arrows point to the experiments where the surface was precovered with oxygen to eliminate the induction period. This was done by exposing the catalyst to gaseous or aqueous oxygen.

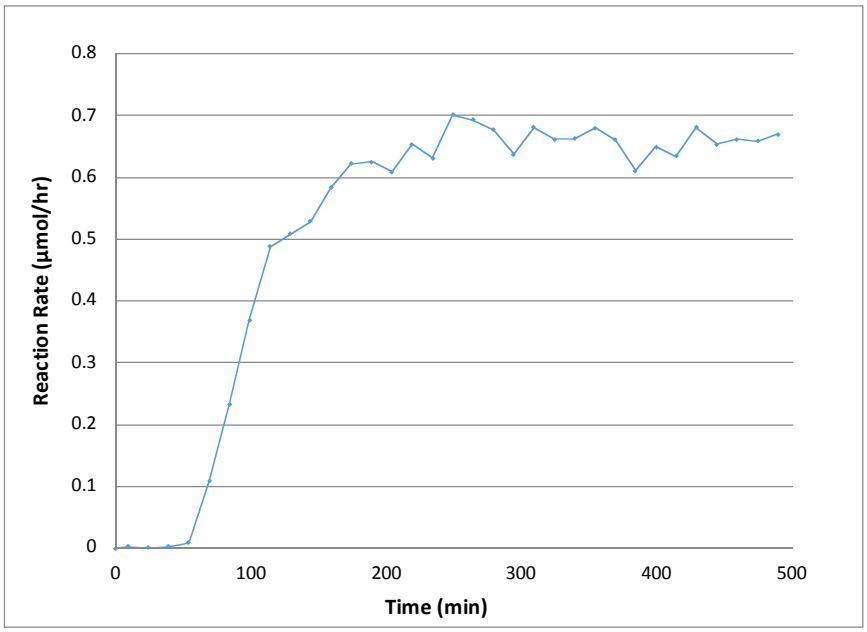

Figure 6.3: Activity of 20 nm thick platinum catalyst showing the induction period for the thick film and ruling out significant effect of the titania underlayer . Conditions: 217 mM ethanol in water, 62 μM O_2, 30°C.

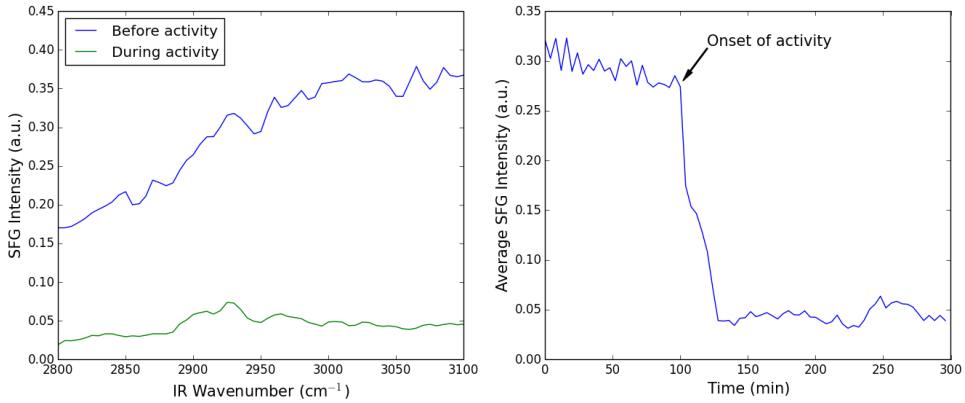

Figure 6.4: The SFG spectrum during the induction period and after the onset of activity. The figure on the left shows the average SFG spectra before and after activity onset. The average of the non-resonant background between 2800 $^{-1}$ and 3600 cm^{-1} as a function of time is shown on the right. Conditions: 217 mM ethanol in water, 30°C.

Under ethanol oxidation reaction conditions, the platinum signal starts high. Upon reaching the end of the induction period, the platinum signal drops within a span of approximately 20 minutes, to a level much lower than intensity, whereafter it remains steady.

The non-resonant component of the non-linear susceptibility is due to the interaction of the electric fields with conduction electrons in the metal at its surface[7–9]. The effect of oxygen and carbon monoxide adsorption on the second harmonic non-resonant SFG from rhodium single crystal has been studied previously, and it has been demonstrated that the non-resonant signal can change with molecular adsorption onto the metal surface due to localization of surface electrons, which dominate the non-resonant response[2,3].

The effect of oxygen on the non-resonant background of the platinum catalysts was tested in the following way: after the normal pretreatments, the platinum surface was exposed to water that had been saturated with hydrogen. Hydrogen has a solubility in water of 900 μM, similar to that of oxygen. Under these conditions the SFG signal of the surface was stable over a period of two hours. Apparently the hydrogen dissolved in the water is enough to keep the surface reduced. After this, the surface was exposed to water with a concentration of 62.5 μM O_2. The exposure to oxygen caused the decrease of the SFG signal from platinum immediately. Figure 6.5 shows the SFG spectra in the presence of H_2 and O_2.

The effect of ethanol on the non-resonant background was tested in an experiment where the catalyst, after usual pretreatment, was exposed to water saturated with hydrogen. Then the liquid was switched to a 217 mM solution of ethanol in water, which had been bubbled with hydrogen. The intensity of the non-resonant background was preserved throughout the introduction of ethanol to the system under hydrogen. The non-resonant intensity was further constant when the hydrogen was replaced with nitrogen. A solution of ethanol with 62.5 μM O_2 also effected no decrease in the non-resonant signal. Finally, adding water only with 62.5 μM O_2 decreased the non-resonant intensity. These results demonstrate that either the adsorption of ethanol has little effect on the non-resonant signal or ethanol, on a

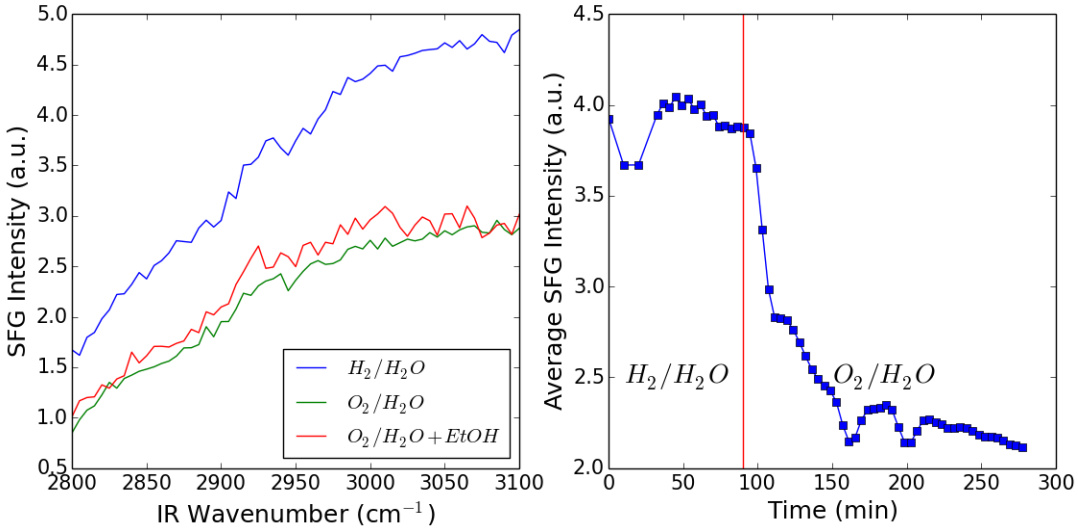

Figure 6.5: Left: Non-resonant SFG spectra of platinum under conditions of H_2/H_2O, O_2/H_2O and O_2/217 mM ethanol in H_2O. Right: The averaged signal for the SFG spectra under aforementioned conditions, showing the abrupt decrease upon adsorption of oxygen on surface.

fully reduced surface, is not capable of altering the non-resonant response of the solid-liquid interface.

Another reason for the observed non-resonant SFG change upon surface oxidation could be the change in the value of the refractive index of the interface. The intensity of measured SFG is dependent on the local field correction factors,L , also known as the Fresnel factors, for the electric fields at the surface. The L are polarization dependent. In the case of an ordered thin layer between two semi-infinite media, the expression for L_{zz} is

$$L_{zz} = \frac{2n_1 cos\theta_1}{n_1 cos\theta_2 + n_2 cos\theta_1} \cdot (\frac{n_1}{n_{interface}})^2 \tag{6.3}$$

The $n_{interface}$ term will change with the nature of the intermediate thin layer. Thus, although resonant features from adsorbed oxygen on platinum are not observable, the effect of the oxygen on the local field factor, L at the platinum/adsorbate interface could be significant. The non-resonant susceptibility for the *ppp* polarization combination is the sum of four terms, of which two are expected to be negligible because of the metal dipole selection rule. The two terms that are significant are the χ_{xxz} and χ_{zzz}. Multiplied by the appropriate field factors, the non-resonant background is written,

$$I_{SFG,ppp} \propto | -L_{SFG,xx} L_{VIS,xx} L_{IR,zz} \chi_{xxz} + L_{SFG,zz} L_{VIS,zz} L_{IR,zz} \chi_{zzz} |^2$$

where multiplicative factors in front of each term involving the angles of incidence are excluded for clarity.

The explicit forms of the local field factors have been derived for a system of a thin film between two media - such as an organic adsorbate at the interface of a metal and a liquid.

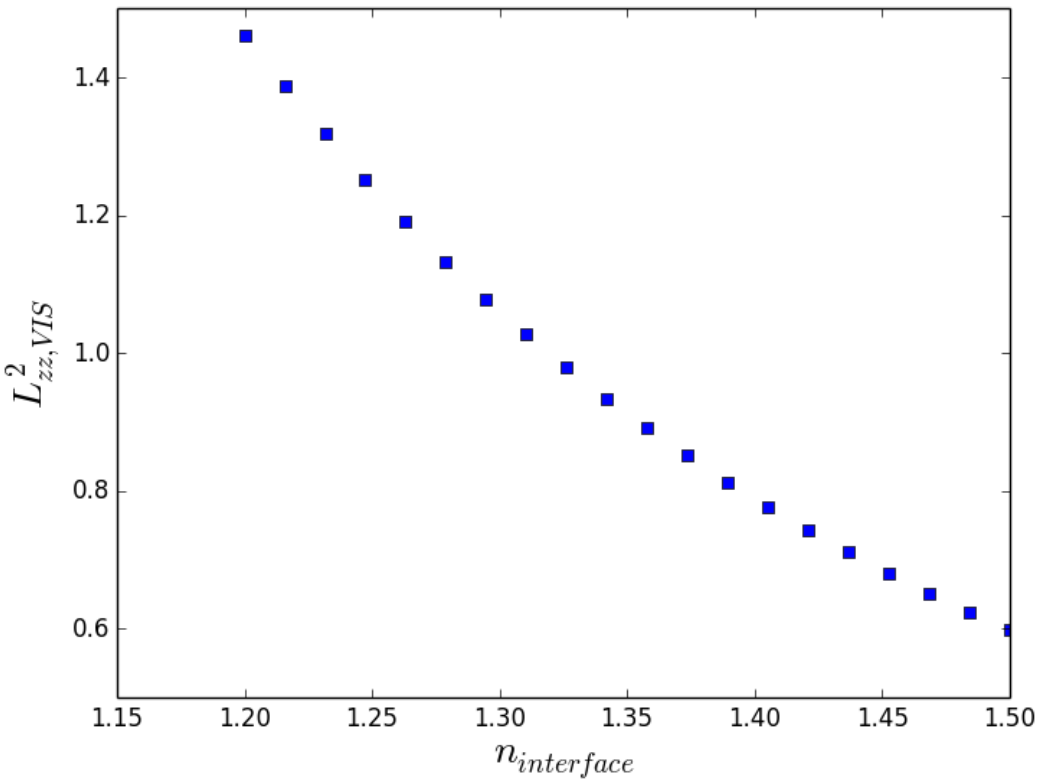

Figure 6.6: The local field factor, L_{zz} as a function of $n_{interface}$ calculated using equation 6.3 for the platinum liquid interface in the systems of platinum/water calculated for $\lambda = 532$ nm. An angle of 62° was used for the incident angle.

We do not consider here the fact that the metal is also a thin film. While this may have an effect on the absolute values of the field factors calculated, we do not expect it will have a major effect on the *changes* in L. Using the known indices of refraction for platinum and water, it is possible to calculate the local field factors for the platinum/liquid interface as function of the interface refractive index at the platinum surface (Figure 6.6).

Modelling the induction period in alcohol oxidation

A kinetic model that explains the induction period should rely on some form of positive feedback. A kinetic model for ethanol oxidation on platinum with a simliar feedback feature was put forward by Jelemensky *et al.*[1,10]. In their work, the authors justified the existence of multiple steady states in alcohol oxidation by the existence of three interconverting oxygen species; OH_{ads},O_{ads} and $O_{subsurface}$ with the reactivity toward dehydrogenation of alcohol decreasing in that order; on the surface. However, our kinetic data indicate that in our case the surface is becoming simultaneously more oxidized and more active, a simple correlation that is not reflected in the model of Jelemensky. We also looked for a model based on simpler elementary steps than those used in the above model.

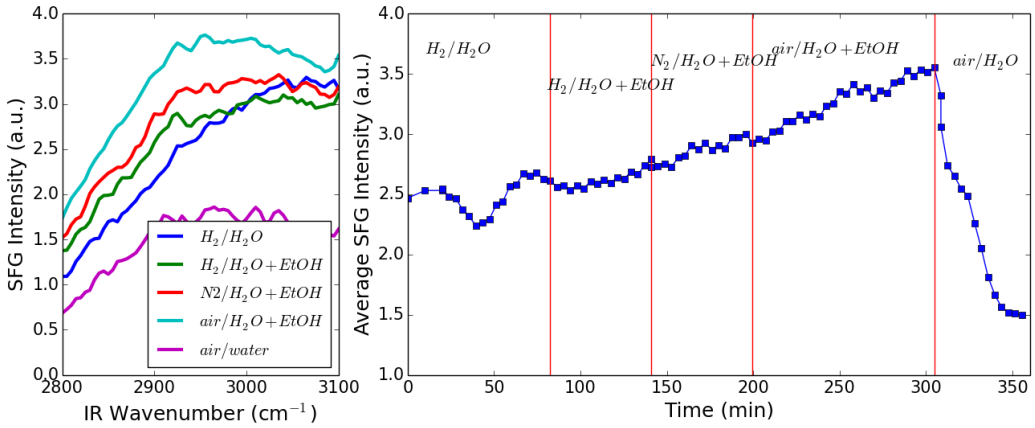

Figure 6.7: Left: Non-resonant SFG spectra of platinum under conditions of H_2/H_2O, H_2/Ethanol, N_2/Ethanol, O_2/Ethanol, and O_2/H_2O. Right: The averaged signal for the SFG spectra under aforementioned conditions. Apparently neither water nor ethanol affects the non-resonant signal, but exposure to oxygen immediately causes the decrease in the signal similar to what is seen under reaction conditions.

Following the equations 6.4, which predict the main feedback mechanism is an increase of free sites, it is possible to propose a mechanism in which the rate limiting step is the second dehydrogenation step (a cleavage of the C-H bond). This step may have different rates when the hydrogen forms a bond with an empty surface site or an adsorbed oxygen species. Our model does not distinguish between adsorbed oxygen atoms and hydroxyl groups, although this may play a critical role in other aspects of the reaction. In the proposed model, where $Ethoxy_{ads}$ is an adsorbed ethoxy (singly dehydrogenated) species and Al_{ads} is the adsorbed aldehyde (doubly dehydrogenated) species, the conversion between $Ethoxy_{ads}$ and Al_{ads} is slow when the hydrogen goes onto an empty surface site and much faster when interacting with an adsorbed oxygen species (OH_{ads} and O_{ads}) (equations 6.4e,f and g). The oxygen species and ethanol compete for surface adsorption sites (Pt). Hydrogen is assumed to adsorb on a different site. Assuming that the surface starts fully covered with ethanol and hydrogen sites are fully occupied as well, the reaction is totally controlled at first by the slow desorption of $Ethoxy_{ads}$ (reaction 6.4b), whereupon alcohol and oxygen in solution compete for the open site generated at the surface. If alcohol adsorbs at this site, the overall net change is zero, but if oxygen adsorbs, then each O_{ads} will consume two hydrogen atoms and desorb (reactions 6.4c and d), leaving the site open for the next competition of oxygen and ethanol. The overall change in this case is the consumption of two hydrogen atoms per oxygen atom which adsorbs until the chain reaction is terminated by ethanol adsorption at the site.

$$2Pt + O_2 \underset{k_{-a}}{\overset{k_a}{\rightleftharpoons}} 2O_{ads} \tag{6.4a}$$

$$2Pt + EtOH \underset{k_{-b}}{\overset{k_b}{\rightleftharpoons}} H_{ads} + Ethoxy_{ads} \tag{6.4b}$$

$$H_{ads} + O_{ads} \xrightarrow{k_c} OH_{ads} \tag{6.4c}$$

$$OH_{ads} + H_{ads} \xrightarrow{k_d} 2Pt + H_2O \tag{6.4d}$$

$$Ethoxy_{ads} + Pt \xrightarrow{k_e} H_{ads} + Al_{ads} \tag{6.4e}$$

$$Ethoxy_{ads} + O_{ads} \xrightarrow{k_f} Al_{ads} + OH_{ads} \tag{6.4f}$$

$$Ethoxy_{ads} + OH_{ads} \xrightarrow{k_g} Al_{ads} + Pt + H_2O \tag{6.4g}$$

$$Al_{ads} \xrightarrow{k_h} Pt + Acetaldehyde \tag{6.4h}$$

$$O_{ads} + H_{ads} \xrightarrow{k_i} OH_{ads} + Pt \tag{6.4i}$$

$$OH_{ads} + H_{ads} \xrightarrow{k_j} 2Pt + H_2O \tag{6.4j}$$

Because the reaction between H_{ads} and O_{ads} is assumed to be very fast, for the period of time in which hydrogen is still present on the surface, nearly all oxygen adsorbed on the surface is removed by its reaction with hydrogen. Despite the very fast reaction between O_{ads} and H_{ads}, the consumption of H_{ads} on the surface is limited by the very slow desorption rate of alcohol; thus the induction period can last thousands of seconds. When the hydrogen on the surface has finally been consumed, oxygen can build up on the surface and the reaction of oxygen with ethoxy species on the surface begins to be significant. At this point the reaction rate increases drastically due to the new open pathway for creation of Al_{ads}, and the surface is rapidly converted to ethoxy-dominated to ethoxy-oxygen mixed. This series of events is shown in Figure 6, which has the onset of activity at about 1000 seconds. The coverages of surface species in monolayers is shown in the upper plot. The lower plot shows the rate of acetaldehyde production which is equal to the concentration of Al_{ads} on the surface multiplied by the rate constant of its desorption.

The model is also capable of describing the positive correlation between oxygen concentration in solution and the reaction rate. Because the concentration of oxygen on the surface is zero during the induction period, varying the rate of oxygen desorption has no effect on the length of the induction period. As oxygen builds up on the surface, however, it has a critical effect in determining the steady state reaction rate.

Implications for alcohol oxidation

Many works in the literature have deduced that the platinum surface must be covered by hydrogen during the reaction[11,12]. Prior work by DiCosimo et al. used open circuit potential measurements to determine the state of the surface under isopropanol reactions conditions[13,14]. These measurements showed that the platinum surface potential was low while in the active state (approximately -0.2 V vs. Ag/AgCl), i.e. the surface was partially covered with hydrogen. Under batch reaction conditions, as the alcohol in the solution was consumed the open circuit potential increased due to increasing coverage of the platinum electrode by oxygen. In contrast to our results, however, in these experiments the open circuit potential varied slowly and smoothly, whereas we see a sudden change in the SFG non-resonant background. Also, our experiments indicate that the fully reduced surface is not active - even in the presence of dissolved oxygen - and even that a certain threshold of surface 'oxidation'

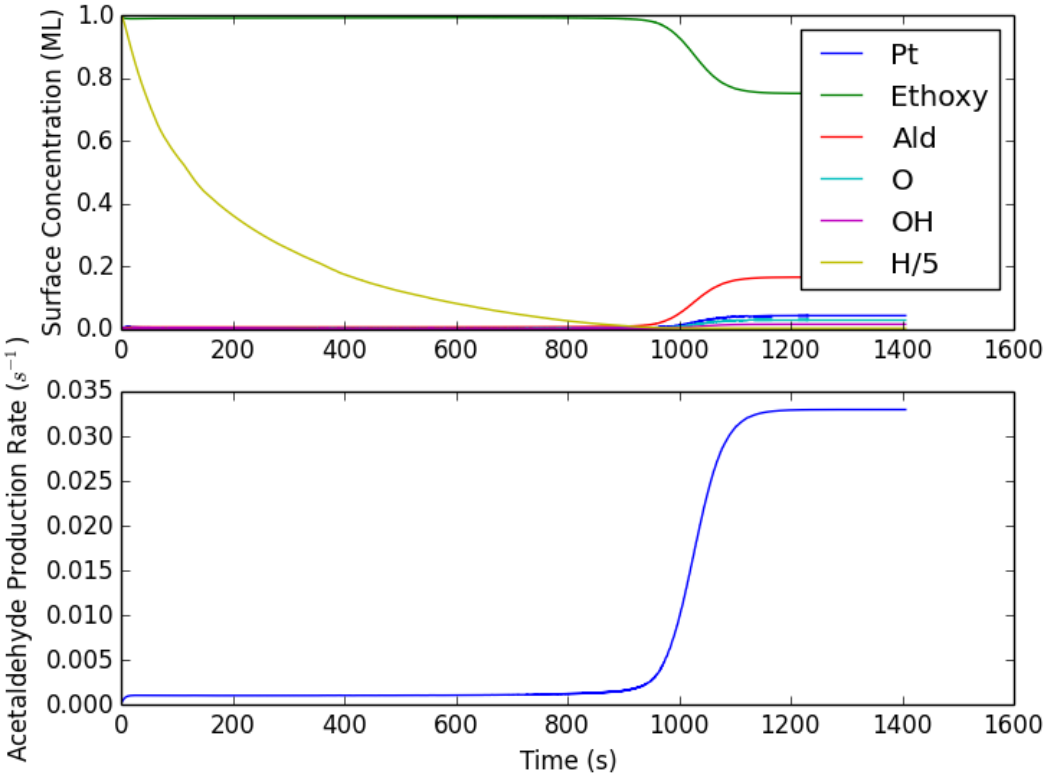

Figure 6.8: Top: Relative coverages (in monolayers) of surface species on platinum catalyst as a function of time during the reaction. The induction period consists of the consumption of surface hydrogen, limited by the slow desorption of alcohol from the surface. The fast increase in oxygen species at the end of the induction period is accompanied by a decrease in ethoxy coverage and an increase in the adsorbed product. The rate directly follows the coverage of the adsorbed product. Bottom: the reaction rate (s^{-1}) as a function of time.

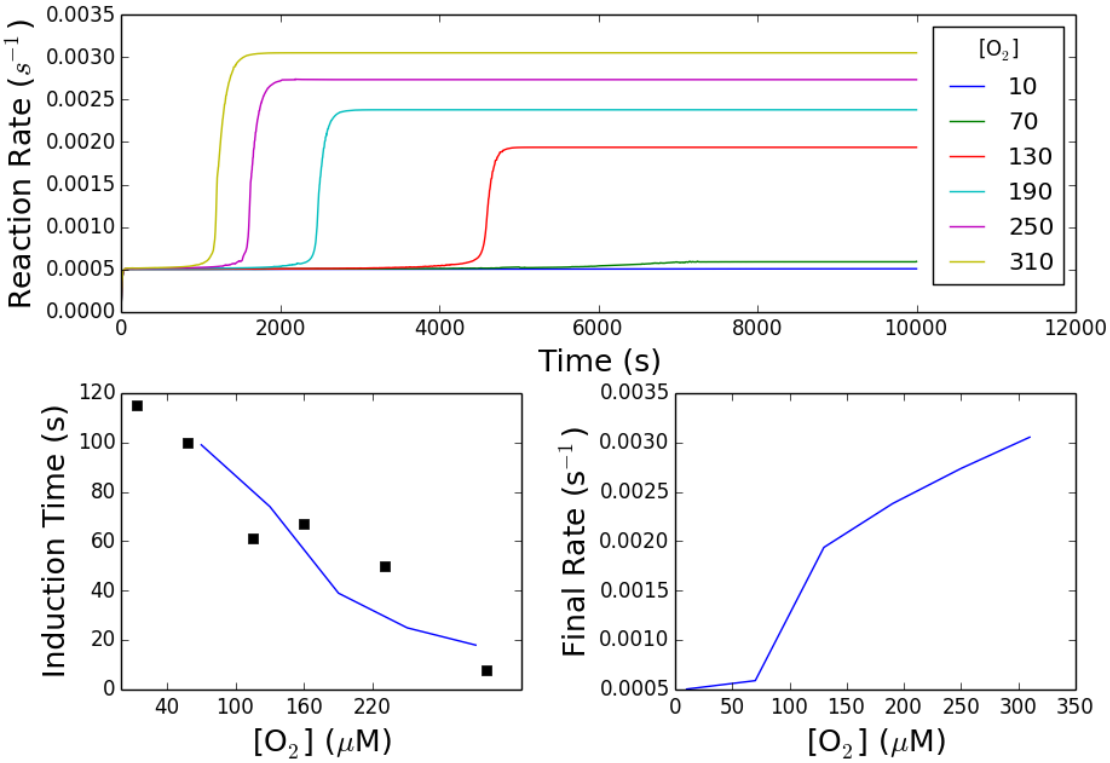

Figure 6.9: Top: the reaction rates as of acetaldehyde production as a function of time for varying oxygen concentrations. The induction period shortens with increased alcohol concentration. Also apparent is the increased rate of oxidation with oxygen concentration. Bottom Left: The induction period length as a function of oxygen concentration. The black dots are the experimental data and the blue line represents the results of the model. Bottom Right: The reaction rate as a function of oxygen concentration. Rate constants used for this figure were $k_a = 1 \times 10^6$;$k_{-a} = 25$;$k_b = 0.35$;$k_{-b} = 5 \times 10^{-4}$; $k_c = k_d = 25$; $k_e = 5 \times 10^{-3}$; $k_f = 0.005$; $k_g = 0.5$; $k_h = 0.1$; $k_i = k_j = 50$.

must be reached before turnover begins. Some differences exist between our experiment and that of DiCosimo et al. Firstly, their experiment was carried out under very acidic (0.1 M H_2SO_4). Also our experiments were carefully conducted well below the oxygen poisoning threshold, so that our results describe precisely the evolution of the surface in steady-state conditions.

It is commonly stated in the literature of alcohol oxidation that empty platinum surface sites are important for the adsorption of alcohol, and that over-oxidation is responsible for the poisoning of the platinum catalyst. The results presented here suggest that oxygen on the surface significantly enhances the reaction rate, and our model suggests that a significant portion of the metal sites may be filled under steady-state conditions. Despite this the catalyst remains active due to the effective competition between oxygen removal and adsorption. We have not been able to reproduce the over-oxidation phenomenon with this model as of yet. This may be accomplished by allowing for the interconversion of OH_{ads} and O_{ads} and a different value for k_f, k_g, k_h and k_i

In addition our experimental results agree with a model that relies on the rate of the elementary step in equation 6.4f to be much faster than that in equation 6.4b. Although this is not a new proposal, our results are further evidence that this may indeed be the case, and that under active conditions, that equation 6.4f is the main reaction pathway. Of course, the true indication of the model is only that the rate limiting step involves some interaction with surface oxygen, and our data does not necessarily implicate C-H bond cleavage.

Conclusions

The results of this chapter demonstrate an uncommon use of sum-frequency generation to investigate the oxidation state of a metal surface at a buried interface during the induction period observed for ethanol oxidation by oxygen in the aqueous phase. The non-resonant background signal of the platinum metal being interrogated is dependent on the extent of oxygen adsorption, and is not affected by hydrogen, ethanol or nitrogen. The SFG results in conjunction with reaction rate data, which show that increasing the oxygen concentration in solution decreases the induction period, strongly suggest that a surface without a non-zero oxygen coverage inactive toward alcohol oxidation. Also, a kinetic model including positive feedback mechanisms in the elementary steps is able to simulate the induction period, as well as the trends seen for oxygen dependence of the induction time and the reaction rate as a function of oxygen. The kinetic model provides credence for the idea that the rate limiting step (possibly the abstraction of the second hydrogen) may be faster via interaction with an adsorbed oxygen species than with a bare platinum surface.

References

[1] Jelemensky, L.; Kuster, B. M.; Marin, G. *Catalysis Letters* **1995**, 269.

[2] Tom, H.; Mate, C.; Zhu, X.; Crowell, J.; Heinz, T.; Somorjai, G.; Shen, Y. *Physical Review Letters* **1984**, *52*, 348–351.

[3] Shen, Y. *Nature* **1989**, *337*, 519–525.

[4] Thompson, C.; Carl, L.; Somorjai, G. *In preparation*

[5] Battino, R.; Rettich, T.; Tominaga, T. *J. Phys. Chem. Ref. Data* **1983**, *12*, 163–178.

[6] Thompson, C.; Carl, L.; Somorjai, G. *Journal Of Physical Chemistry C* **2013**, *49*, 26077–26083.

[7] Petukhov, A. *Physical Review B* **1995**, *52*, 16901–16911.

[8] Liebsch, A. *Physical Review B* **1989**, *40*, 3424–2424.

[9] Liebsch, A. *Applied Physics B* **1999**, 301–304.

[10] Jelemensky, L.; Kuster, B. M.; Marin, G. *Chem. Eng. Sci.* **1996**, 1767.

[11] Mallat, T.; Baiker, A. *Catalysis Today* **1994**, 247.

[12] Mallat, T.; Baiker, A. *Chem. Rev.* **2004**, 3037.

[13] DiCosimo, R.; Whitesides, G. *J. Phys. Chem.* **1989**, 768.

[14] Nicoletti, J.; Whitesides, G. *Journal Of Physical Chemistry* **1989**, 759–767.

Chapter 7

Study of the platinum-poly(amidoamine) dendrimer system and formulation of an ultraviolet light induced synthesis

In this chapter platinum and rhodium nanoparticle formation in the G4OH PAMAM dendrimer system is investigated using various spectroscopic techniques. UV-resonance Raman spectroscopy, temperature programmed FTIR, and UV-vis spectroscopy indicate that platinum ions in the dendrimer are not effectively reduced using the usual reducing agent, sodium borohydride, but instead form linear "platinum blue"-like compounds. Rhodium ions under the same conditions are completely reduced and form metallic nanoparticles. UV-resonance Raman spectra indicate that the platinum ions are coordinated to amide nitrogen atoms within the dendrimer structure which evidently have a strong stabilizing effect on the ions. FTIR spectroscopy of the amide I and amide II modes shows that platinum in turn changes the secondary structure of the dendrimer, likely by coordinating to multiple amide groups. We show that both thermal decomposition of the dendrimer in H_2 and exposure to ultraviolet light are methods for releasing platinum ions from their chelated state and forming nanoparticles.

From these results we propose and test a new method for forming nanoparticles in the dendrimer system. Exposure to UV light at 254 nm in solution causes platinum ions to form nanoparticles within the dendrimer shell. The particle size is independent of the amount of platinum in the PAMAM structure and particles formed are always less than 2 nm in diameter. The proposed method is a new route to platinum nanoparticles in the dendrimer template which appears to proceed through a mechanism different than previously suggested for sodium borohydride reduced particles.

Introduction

While SFG studies of alcohol oxidation are made simpler by using a continuous thin film catalyst, there is a major drawback to the approach. The electron beam evaporated films are notoriously heterogeneous in their structure. Single crystals offer the opposite - a single exposed surface facet - but cannot be probed by SFG without restricting flow of the reactant mixture. Colloidally synthesized nanoparticles offer the best of both worlds: strict control over nanoparticle shape and size yielding a highly uniform catalyst structure with well defined surface facets and the possibility of using the internal reflection mode for SFG. In addition, colloidally synthesized nanoparticles can possess very narrow size distributions making them perfectly suited for size dependent studies.

One common platform for monodisperse metal nanoparticles with a diameter less than 2

nm is colloidal synthesis mediated by the capping agent, the poly(amidoamine) (PAMAM) dendrimer. The dendrimer has already been applied as a capping agent in the synthesis of gold, platinum, rhodium, silver, and palladium nanoparticles[1–4]. It is supposed that the dendrimer offers control of the nanoparticle size by allowing precise control of the local concentration of metal precursor ions inside the dendrimer, which are then reduced to form nanoparticles. As the over-oxidation of platinum-group metals in alcohol is known to be easier for smaller particles, using the dendrimer-based approach for platinum nanoparticle synthesis could be a route to precise studies of this size dependence[5–8]. Also, gold nanoparticles are active in alcohol oxidation *only* below ~ 3 nm in diameter. Highly monodisperse nanoparticles below this size are critical to well-controlled investigations of this size effect.

In this chapter the use of the dendrimer in the synthesis of platinum and rhodium nanoparticles in the PAMAM dendrimer is explored[9]. We find that, while rhodium is easily reduced by sodium borohydride, the dendrimer-mediated synthesis of platinum particles is hindered by the fact that sodium borohydride cannot fully reduce the Pt^{2+} precursor ions complexed to the dendrimer. Instead platinum ions form linear chains of two or more ions, which are similar to "platinum blue" compounds previously synthesized. Some evidence for this was reported in other work[3,10], and we propose that the multiple coordination of platinum to amide nitrogen atoms in the dendrimer is responsible for this stability toward full reduction[9]. Using temperature programmed Fourier transform IR spectroscopy we can monitor the thermal degradation of the dendrimer capping agent, which results in the freeing of the platinum ions from complexation and the formation of metallic nanoparticles.

We also show that platinum particles are formed when the Pt^{2+}/PAMAM complex is exposed to ultraviolet light (254 nm)[9]. It is likely that the absorption of the complex around 250 nm, corresponding to a ligand-metal charge transfer, is the event that initiates bond cleavage and particle formation. We apply this knowledge to the synthesis of dendrimer-capped platinum nanoparticles in solution. Results from UV-Vis, spectroscopy, X-ray photoelectron spectroscopy (XPS), high resolution transmission electron microscopy (HRTEM), and aberration corrected ultra high resolution TEM (UHRTEM) show that the platinum is mainly in the form of monodisperse, metallic, non-crystalline particles which have a diameter of around 1.4 nm. The size of the particles increases with increasing irradiation time, but the diameter is not dependent on the concentration of platinum, indicating that the supposed mechanism of size control commonly described for sodium borohydride reduced particles may not be operating in this synthesis.

Experimental details

Particle synthesis

Particle preparation with $NaBH_4$ was performed using previously reported methods[11]. Briefly, K_2PtCl_4 was allowed to complex with the fourth-generation poly(amidoamine) hydroxyl-terminated dendrimer (G4OH) in water. A dendrimer solution (Dendritech, Midland, MI) with the desired mole equivalent of Pt^{2+} ions was mixed for 10 days at 4 °C. Excess Pt ions were removed by 3 rounds of dialysis. An excess of sodium borohydride was then added while stirring.

For UV synthesized platinum clusters, a similar process was carried out, but instead of

adding sodium borohydride, the solution of Pt^{2+}-PAMAM was loaded into 1 cm diameter fused silica tubing and exposed to 254 nm light from low pressure mercury lamps. The radiation intensity was approximately 25 W/m^2.

Spectroscopic characterization

UV-Raman was performed using a continuous wave intracavity doubled argon ion laser (244 nm). Backscattered light was collected and directed into a Spex 1877C, triple spectrometer optimized for the deep UV region. Spectra were collected with a liquid N_2 cooled UV-enhanced CCD camera (2.1 cm^{-1}/pixel dispersion with typical resolution of 12 cm^{-1}) [12,13]. The sample was rotated and translated to minimize degradation of the sample due to UV irradiation which decreased the average exposure by a factor of 1000 compared to a non-moving sample. Typical collection times were 5-30 min at 3-5 mW.

UV-vis spectroscopy was carried out with a Perkin-Elmer LAMDA 650 with scanning range of 190-900 nm. Aliquots of sample were drawn from solution and placed in fused silica cuvettes for analysis or dropcast on aluminum foil for reflectance measurements using 60 mm integrating sphere coated with Spectralon.

Diffuse reflectance Fourier transform infrared spectra were acquired with a Nicolet-Nexus-6700 spectrophotometer with integrated diffuse reflectance optics (Spectra-Tech Collector II). Samples of dendrimer were deposited on aluminum foil by dropcasting. Each spectrum was the average of 128 or more scans with a resolution of 4 cm^{-1}. The vacuum chamber (Spectra-Tech 0030-101) was used for *in situ* IR meausrements in 10% H_2 (balance Ar), N_2, or O_2.

Transmission electron microscopy

"Normal" High resolution TEM was performed on a JEOL 2100 microscope at 200 kV. Particles were deposited on ultrathin carbon grids. Images were taken in multiple areas to ensure wide sampling. Particles were counted using Gatan Digital Micrograph software using previously performed calibrations.

Aberration corrected transmission electron microscopy was carried out on the TEAM 1 microscope at the National Center for Electron Microscopy. The accelerating voltage used for imaging was 80 kV with a typical electron current of 1 mA/cm^2.

Results and discussion

UV-Vis monitoring of the complexation and reduction of metal ions on G4OH

UV-vis spectroscopy has been used repeatedly to follow the reduction of Pt^{2+} ions in the PAMAM dendrimer. The dendrimer itself absorbs below 240 nm due to $\pi* \leftarrow n$ and $\pi* \leftarrow \pi$ transitions of amide groups. The absorption band of the PtG4OH complex at 250 nm has been attributed to a ligand-to-metal charge transfer (LMCT) transition. Figure 7.1a shows the UV-vis absorption spectra of PtG4OH after reduction by $NaBH_4$. The spectra clearly show that the LMCT peak indicative of the unreduced platinum ions persists even after exposure to excess sodium borohydride. In Figure 7.1b the reduction efficacy of sodium borohydride for PtG4OH and RhG4OH are compared directly, and it is evident that rhodium

does not exhibit the same resistance to reduction that platinum does. Interestingly, the $NaBH_4$ treated PtG4OH samples are not totally unaffected, since their UV-vis absorption spectra show the growth of a new, red-shifted peak at 280 nm. This peak matches well with the signals from Pt clusters (Pt_{2-4}), commonly known as platinum blue[14–17]. This result is surprising, since the reduction of platinum is highly thermodynamically favorable. In spite of many examples of full reduction of platinum in other colloidal nanoparticle syntheses by sodium borohydride, we are not the first to see that platinum resists reduction in this particular system. Similar Pt-Pt low coordination numbers after attempts to synthesize nanoparticles in the PAMAM dendrimer were suggested in previous EXAFS experiments[10].

Reduction in hydrogen gas at high temperature is another possible way to achieve the reduction of metal ions. After drying onto aluminum foil the PtG4OH samples were heated to 150 °C in a 4% hydrogen atmosphere (balance argon) for up to 90 minutes. Diffuse reflectance UV-vis spectra of these samples showed that, while the LMCT band was further decreased under these conditions, full reduction of the platinum was still not achieved. Instead, as shown in Figure 7.2 absorption bands at 266 nm, 302 nm, and eventually 342 nm provided further evidence that platinum was clustering into platinum blue-like compounds within the dendrimer even after such strong reducing treatment.

Characterization of G4OH, PtG4OH, RhG4OH samples by resonance Raman spectroscopy: Identification of the metal complexation site

While UV-vis spectroscopy is useful in quantifying the extent of reduction of metal ions in the dendrimer system, the coordination environment of ions in the dendrimer is better revealed by vibrational spectroscopy. Resonance Raman spectroscopy especially has the ability to establish the coupling of electronic transitions with the vibrations of nuclei. Raman spectroscopy is based on the inelastic scattering of light by molecules. Energy from the incident photon is imparted to the molecule in the form of a vibrational excitation. Any frequency of light can be used in Raman scattering experiments, but when the frequency chosen is nearly resonant with an electronic transition in the molecule, certain vibrational modes will be enhanced in the Raman spectrum. Specifically, if the rearrangement of the nuclei following that electronic transition involves motion along a vibrational mode, then that vibrational mode will be enhanced. In practical terms, the modes that are enhanced will normally be those involving the motions of the atoms closest to the transition center.

Figure 7.3a shows the resonance Raman spectra of G4OH, PtG4OH, and RhG4OH. As the frequency doubled output of an argon ion laser (244 nm) is close to the LMCT band of the Pt^{2+}-dendrimer complex (Figure 7.3b), we see enhancement of the modes of atoms located close to the Pt ions. The effect of the resonance enhancement is seen in the much greater signal to noise ratio for the PtG4OH spectrum (number 2) compared to the G4OH and RhG4OH. G4OH does not have LMCT bands at all, and the LMCT bands of RhG4OH are not as near the excitation wavelength so its enhancement is weak. The G4OH Raman spectra shows modes for the amide I combination band which mostly consists of the C=O stretching mode at 1650 cm^{-1}, the amide II combination mode, which is a combination mode of a C-N stretch and C-N-H bend, at 1580 cm^{-1} and the C_α-C stretch mode at 1440 cm^{-1}[18]. The resonance enhancement for platinum is strongest for the vibrational modes at 1440 and 1580 cm^{-1}. The peaks can be unequivocally assigned to the amide group of

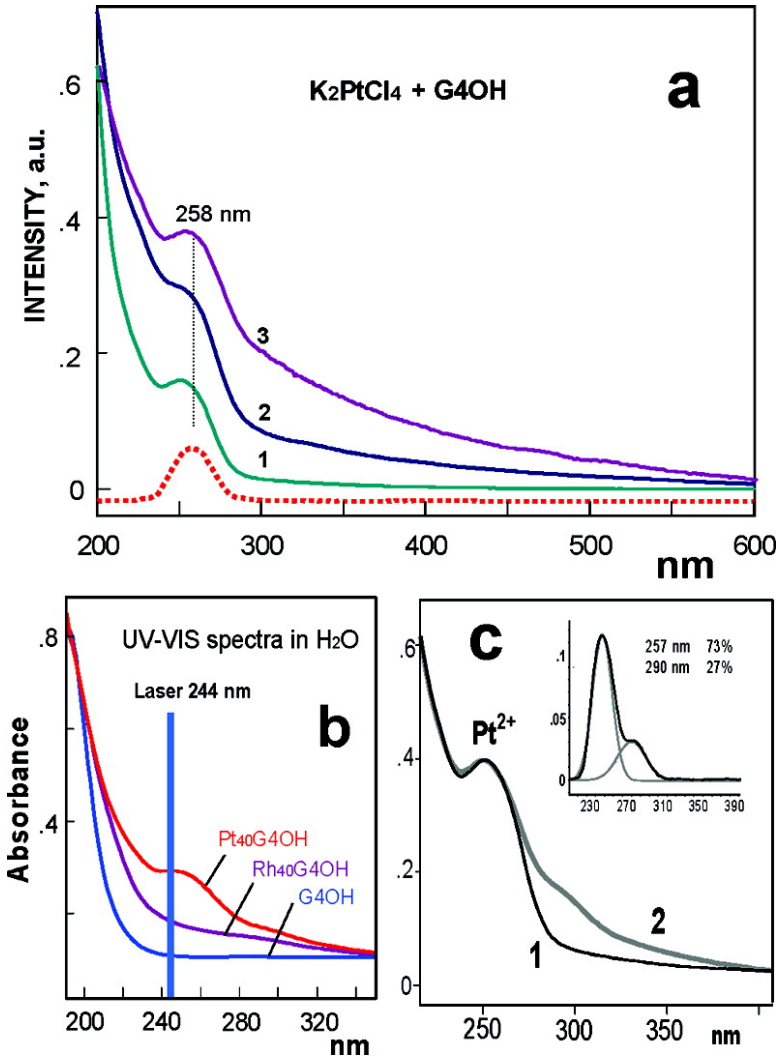

Figure 7.1: (a) UV-vis spectra of PtG4OH (1) Absorption spectrum in water solution after complexation. The background corrected spectrum is traced in dots. (2) Absorption spectrum of dry sample (on quartz window) after reduction by $NaBH_4$ (3) Diffuse reflectance spectrum of dry sample after reduction by $NaBH_4$ (b) Comparison of UV absorption spectra of PtG4OH, RhG4OH, and pure G4OH in H_2O. (c) Absorption spectra of PtG4OH (1) before reduction and (2) after reduction by $NaBH_4$. (Inset of c) Background corrected and deconvoluted UV spectrum of reduced PtG4OH.

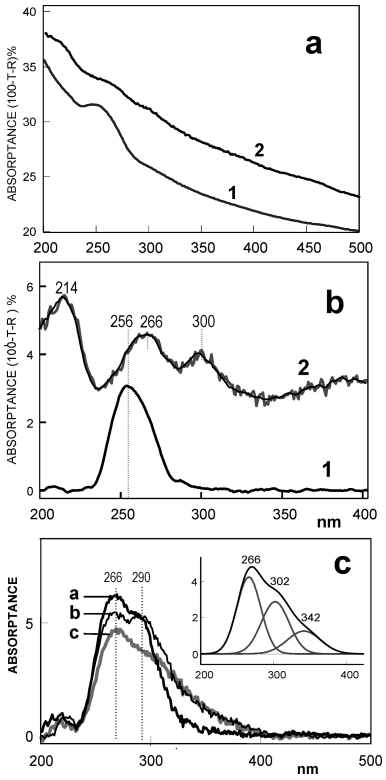

Figure 7.2: UV-vis diffuse-reflectance spectra of PtG4OH/Al. (a1) Spectrum of initial PtG4OH/Al and (a2) after reduction at 150 °C for 60 min in flow H_2/Ar. (b1) Background corrected spectra of initial PtG4OH/Al and (b2) spectrum of PtG4OH/Al after reduction at 150 °C for 60 min in flow H_2/Ar. (c) Time dependence of the charge-transfer band N $\rightarrow$ Pt^{2+} during reduction of PtG4OH in H_2/Ar flow at 150 °C: (c-a) initial, (c-b) 30 min and (c-c) 90 min. (Inset of c) The deconvoluted CT band after reduction for 90 min with three components at 266, 302 and 342 nm.

the dendrimer - a strong indication that Pt ions are complexed with amide groups. The resonance enhancement of the amide II mode, but not the amide I mode, points to the complexation of the ion specifically with the nitrogen of the amide group.

Furthermore, there is a difference in the intensity ratios of the amide I and amide II peaks compared to the pure G4OH. In peptides, the intensity of these peaks is known to be dependent on the secondary structure of the peptide; in other words, the relative orientation of the amide groups. Therefore, from the resonance Raman data, it is evident that the platinum ions in the PtG4OH are still strongly complexed with amide group nitrogen atoms and that this interaction is strong enough to drastically change the "secondary structure" of the dendrimer. Finally, Figure 7.3c shows that this strong interaction is not affected by the exposure of sodium borohydride - further evidence that the platinum remains in an ionic form.

The extreme stabilization platinum atoms by the PAMAM dendrimer cannot be explained purely by amide-Pt bond strength. Other capping agents are used in the synthesis of Pt nanoparticles that do not inhibit the metal ion reduction; one such capping agent is poly(vinylpyrrolidone). Instead it seems likely that the stabilization is provided by a chelate effect through the bonding of platinum ions to multiple amide groups at once. Figure 7 illustrates this interpretation, with the platinum coordinating to multiple nitrogen atoms and thereby acting as a structure director by forcing the amide groups into configurations appropriate for bonding. Rhodium is apparently unable to form the multiply bonded structure required for this unique stabilization.

Temperature programmed FTIR of the PtG4OH and RhG4OH systems

The thermal stability of colloidally synthesized metal particles is an important part of their characterization for their application as catalysts. The high temperatures required for catalysis often cause the aggregation of particles causing a change in their catalytic properties and drop in their overall activity. On the other hand, thermal degradation of the capping agent is frequently used to purposely clean the surface of the metal, opening up more sites for catalysis. The thermal decomposition of G4OH and PtG4OH has been studied previously using TGA[19] The thermal degradation of the organic cap can be conveniently followed using temperature programmed Fourier transform IR spectroscopy. In these experiments the dendrimer and metal-containing, sodium borohydride reduced samples were dropcast onto aluminum foil and their IR spectra were measured as the samples were subject to a heating ramp under atmospheres of O_2, H_2, and N_2. The IR spectra of the G4OH PAMAM dendrimer is shown in Figure 7.5. The assignments for the features of these spectra are presented in Table 7.1[20–22].

Heating the pure dendrimer in all atmospheres generally resulted first in the desorption of hydrogen bonded water at 100 °C. This was indicated by the decrease of the intensity of the OH stretch of water and the emergence of the terminal OH stretch at 3375 cm^{-1}, which had been obscured by the water feature. In addition, the relative intensities of the amide I and amide II modes change upon water desorption, due to the hydrogen bonding of the amide group with water. Around 220 °C a new band appears in the region between 1605 and 1620 cm^{-1}. This corresponds to the creation of CN double bonds, and the combination of this new feature and the steady decrease of intensity of the CH stretch bands and NH stretch

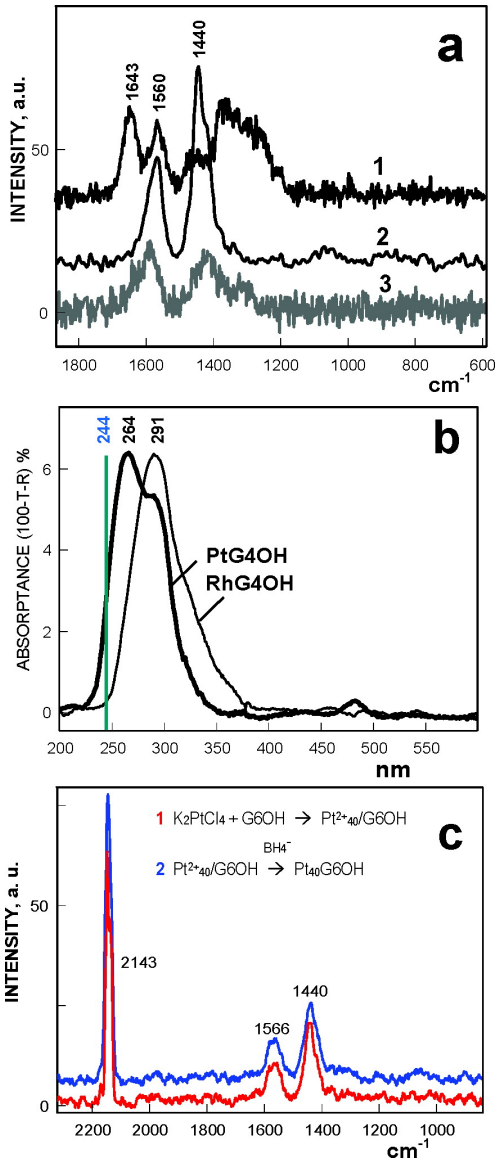

Figure 7.3: (a) UV-Raman spectra of systems dried on aluminum foil. (1) Pure G4OH, (2) PtG4OH , and (3) RhG4OH(3). (b)UV-vis spectra of PtG4OH and RhG4OH. (c) Raman spectra of PtG6OH in H_2O (1) after the "complexation" stage and (2) after reduction by BH_4^-

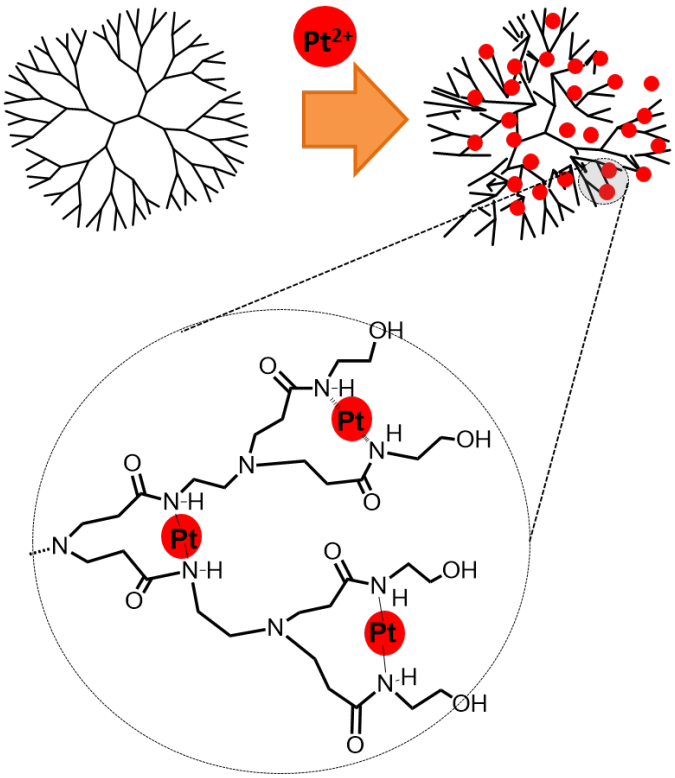

Figure 7.4: Scheme of the coordination of platinum to the G4OH dendrimer as proposed in this work.

IR (cm^{-1})	Mode[18,20–22]
3374	OH_{str} end group
3295	amide NH_{str}
3195(sh)	
3084	amide II overtone
2970	$CH_{2,ss}$
2933	
2872	$CH_{3,ss}$
2824	
1638	amide I (C=O)
1550	amide II, ν(C-N) + δ(C-N-H)
1461	CH_2 def
1432	$C_\alpha H_2$ def
1359	CH_2 wag
1151	amide III
1132	

Table 7.1: IR spectral assignments for the 4th genereration poly(amidoamine) dendrimer (G4OH)

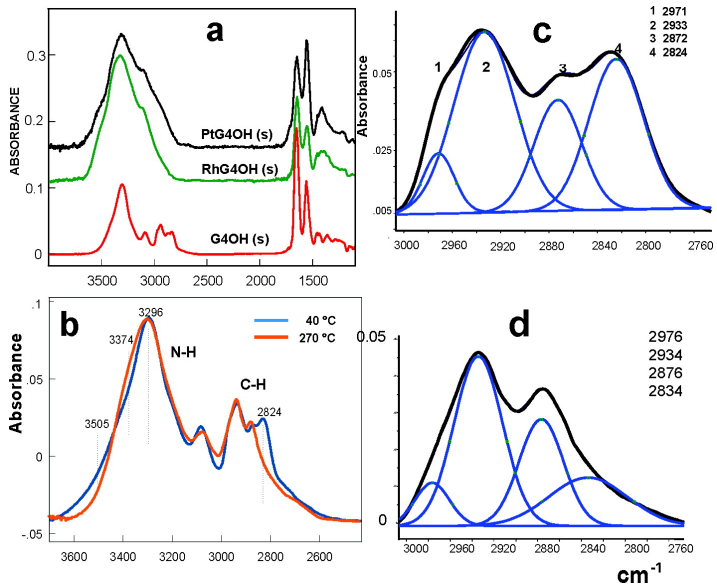

Figure 7.5: (a) FTIR-ATR spectra of G4OH, PtG4OH, and RhG4OH. Drop cast films on Ge prism, s-polarization. (b) Comparison of the FTIR-DRIFT spectra for G4OH heated in O_2 flow at 40 and 270 °C. Intensity is normalized to N-H stretch at 3296 cm^{-1}. (c) Deconvolution of the CH stretching bands (background corrected in panel b) at 40 °C. (d) Deconvolution of the CH stretching bands at 270 °C.

bands indicates a dehydrogenation of the methylene group adjacent to the amide nitrogen. This dehydrogenation process is already documented for other polyamides (Figure 7.6). The temperature programmed FTIR spectra for the pure G4OH at 40 and 270 °C is shown in Figure 7.5.

The thermal decomposition of the platinum- and rhodium-containing dendrimer was quite different from that of the pure dendrimer. The temperature resolved FTIR spectra for PtG4OH and RhG4OH are shown in Figure 7.8, and the integrated intensities of the CH, NH, and Amide I and II features are displayed next to them. Under an oxygen atmosphere the appearance of features at 667 and 2349 cm^{-1} indicates that the IR chamber is filling with CO_2, due to considerable oxidation of the dendrimer above 150 °C. The decrease in intensity at low temperatures due to the evaporation of water is seen, but above 100 °C, the

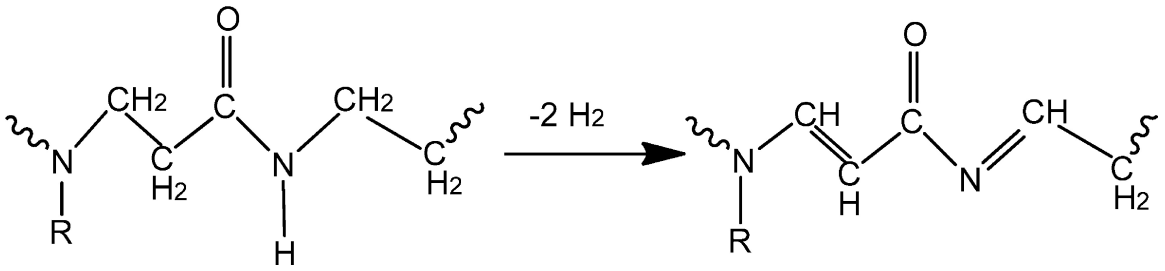

Figure 7.6: The likely products of dendrimer dehydrogenation following hydrogen abstraction at the amide-neighboring methylene group.

CH, NH, and amide I and II features move generally downward, showing that the dendrimer is undergoing fragmentation. Additionally, bands at 2070, 1950 and 1795 cm^{-1} arise in the spectra of PtG4OH and RhG4OH. These bands are characteristic of carbon monoxide on the metal surface. The multiplicity of bands is due to the variety of bonding sites (atop, bridging and 3-fold) present. This degradation process was not observed in the pure dendrimer, so it is attributed metal-catalyzed decarbonylation which leads to dendrimer fragmentation. Finally at very high temperatures (>300 °C), the FTIR spectra show very broad features, indicating that the particles are covered with a highly crosslinked, heterogeneous polyamide-polyene-like material, similar to what has been reported on PVP capped nanoparticles[12].

During the decomposition of PtG4OH in a hydrogen atmosphere we witnessed a reversal in the amide I/amide II intensity ratio, signaling a change from a "contorted", Pt-complexed dendrimer configuration to a "relaxed" configuration with the same amide I/amide II ratio as the pure dendrimer. The effect of this process on the FTIR spectra is shown in Figure 7.7. Based on our interpretation of this intensity ratio, we attribute this to the full reduction of platinum by hydrogen at 230 °C, which results in the formation metallic platinum nanoparticles simultaneous with the decomposition of the dendrimer.

Effects of ultraviolet light on the dendrimer and metal-dendrimer systems

During the Raman scattering experiments, dendrimer decomposition was observed due to the exposure to high intensity UV light produced by the argon ion laser. This can be seen in the Raman spectra in Figure 7.3c, in the form of a peak from a metal-bound carbon monoxide around 2100 cm^{-1}. Further experiments were performed to investigate the action of UV-light on the dendrimer and metal-dendrimer complexes. Dropcast samples of G4OH, PtG4OH and RhG4OH were irradiated by low-pressure mercury lamps, the main emission wavelength of which is 254 nm. The decomposition of the dendrimer could be followed *ex situ* by FTIR spectroscopy of these samples at varying time intervals (Figure 7.9).

During the exposure of the PtG4OH complexation product to 254 nm light, a change in the peak ratios of the amide I and amide II vibrations accompanies the release of Pt^{2+} ions from their strongly coordinated environment and the formation of metallic nanoparticles. The time-dependent FTIR spectra of PtG4OH UV-irradiated in O_2 and H_2 media are presented in Figure 7.9. The intensity of IR bands gradually decreases with increasing irradiation time, and new bands appear in the spectra of PtG4OH at 2230, 2030, and 1820 cm^{-1}. The new bands reflect the photocatalytic effect of platinum on the formation of nitrile band at 2230 cm^{-1} and carbon monoxide (2030, 1820 cm^{-1}) that adsorbs onto platinum. Initially only the CO band for the linear structure appears, and after 20 min CO modes of bridging structures can be seen (Figure 7.9c,d). While the formation of nitrile end groups is more evident in oxygen, the formation of bridging CO modes is more visible in flowing hydrogen. We also observe that as the radiation time increases, the AmI/AmII ratio of intensities for PtG4OH changes and become similar to the ratios for pure G4OH. We believe that the "relaxed" dendrimer 3D structure is also restored under illumination in O_2 and H_2 as a result of the reduction of platinum ions and formation of nanoparticles. Further evidence for nanoparticle formation comes from the appearance of a bridging CO band at 1816 cm^{-1} in the spectrum of PtG4OH (Figure 7.9a). The formation of Pt_n nanoparticles under UV irradiation in solution is well established from Pt^{2+} and Pt^{4+} ions[23–25]. In comparing the UV

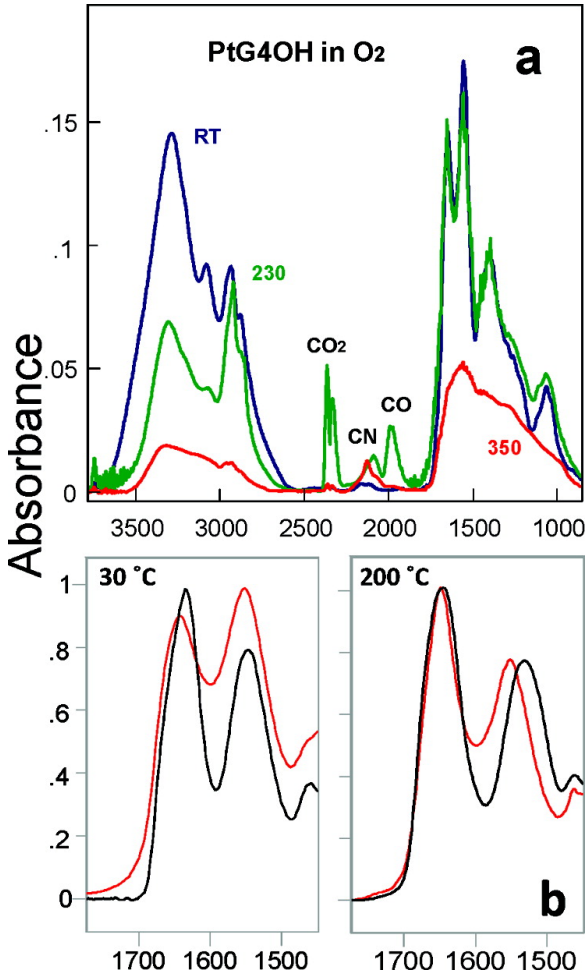

Figure 7.7: (a) FTIR spectra of PtG4OH heated in a flow of oxygen (2.5 °C/min) at three temperatures: RT-30, 230, and 350 °C. (b) Absorption bands amI and amII of G4OH (black) and PtG4OH (red) upon heating in H_2 at 30 and 200 °C.

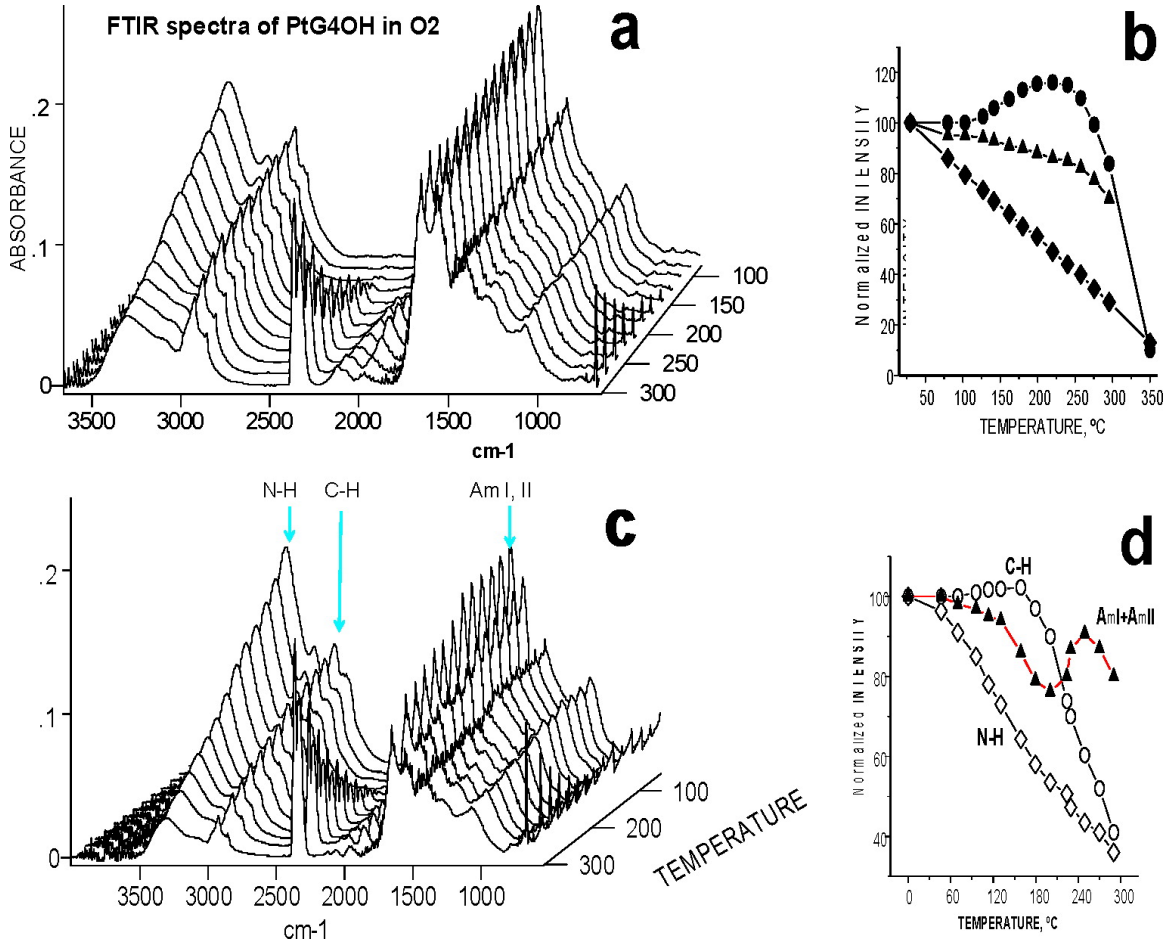

Figure 7.8: FTIR-DRIFT spectra of PtG4OH and RhG4OH heated in a flow of O_2 (2.5 °C/min.) (a) Three-dimensional spectra of PtG4OH. (b) The change in intensities for characteristic bands: N-H (♦), C-H (•), and amide I + amide II (▲).(c) Three-dimensional spectra of RhG4OH. (d) The normalized intensities for characteristic bands: N-H, C-H, and amide I + amide II.

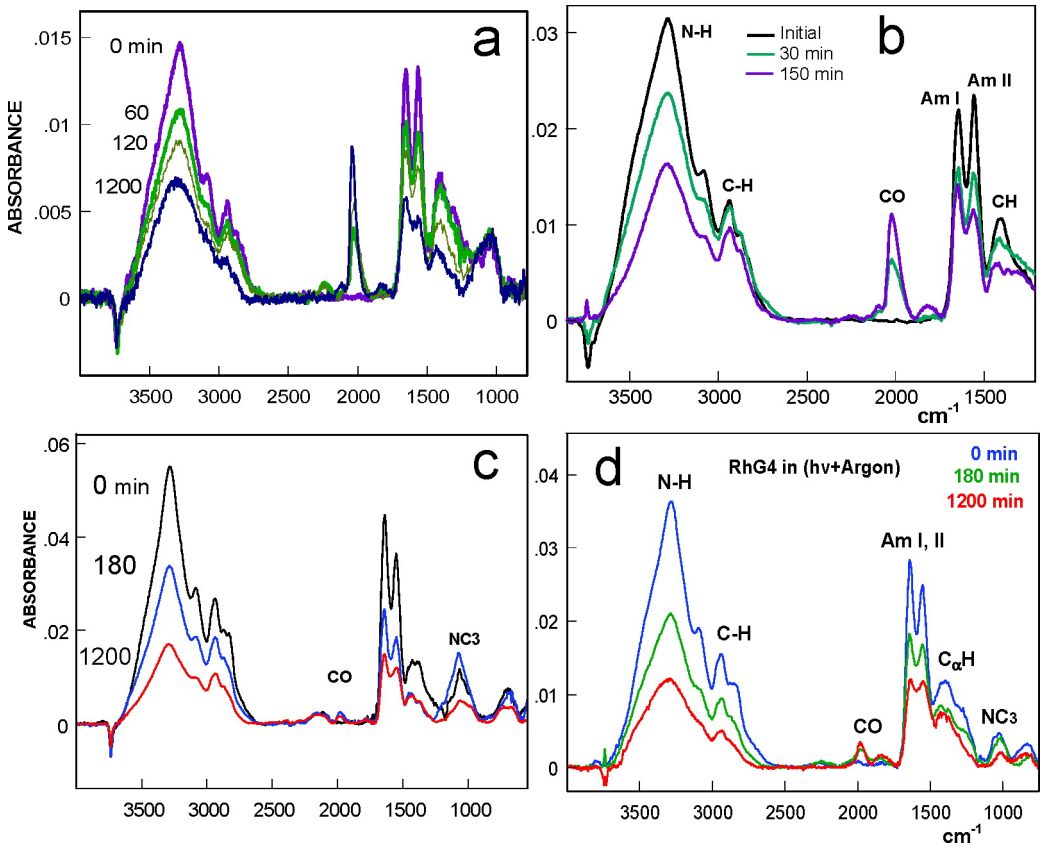

Figure 7.9: Time-dependent FTIR spectra of (a) PtG4OH irradiated in O_2 environment. (b) PtG4OH irradiated in H_2 environment. (c) RhG4OH irradiated in hydrogen flow for 0, 180, 1200 min and (d) RhG4OH irradiated in argon flow for 0, 180, 1200 min.

light-induced decomposition of the pure dendrimer in oxygen and hydrogen, it is apparent that the presence of oxygen accelerates the decomposition. At the same time, the decays of PtG4OH in O_2 and H_2 do not significantly differ (Figure 7.9a,b). Figure 7.9b, which illustrates the decomposition of the CH, NH, and combined AmI and AmII chemical groups in the dendrimer, shows that the catalytic effect of platinum in hydrogen serves to attack the amide groups but not the CH groups. The representative spectra of time-dependent photodecomposition of RhG4OH in hydrogen and argon flow are presented in Figure 7.9c,d. It is evident that photodegradation of capping G4OH in hydrogen and argon atmosphere proceeds at approximately the same rate, which indicates the major role in decomposition is that of UV-light and the minor role that of reactive media such as H_2.

UV induced platinum reduction for the formation of Pt nanoparticles in the dendrimer template

As the above work suggests that the sodium borohydride reductant is not effective in reducing platinum nanoparticles, it is desirable to find another nanoparticle formation method which can still take advantage of the size controlling properties of the PAMAM dendrimer. The FTIR and resonance Raman data presented above demonstrated that UV light was effective in causing platinum aggregation. With this knowledge we can move forward to develop a UV-induced formation of platinum nanoparticles in the PAMAM system.

UV-Vis spectroscopic monitoring of particle growth

Upon irradiation of samples of PtG4OH in the liquid phase we observe a decrease in absorption at 250 nm. The UV-vis spectra of Pt_{40}, Pt_{20}, and Pt_{10} samples irradiated for 5 minutes in Figure 7.10 illustrate this clearly. The decrease of this LMCT band, which begins immediately upon UV light exposure, is followed by an increase in the baseline, which is evidence of the formation of platinum particles. Although the use of the absorption at 250 nm to roughly determine the extent of platinum reduction has been well established, an accurate quantification is problematic, due to the overlap of the other absorptions and the changing baseline.

Ultra-high resolution TEM reveal the detailed structure of the synthesized nanoparticles. In particular, the stability of the structure in time depends strongly on the particle size. Particles >3 nm, shown in Figure 7.12, were indefinitely stable in an fcc crystalline phase under the beam. Except for slow rotation and translation across the carbon support, these particles did not exhibit marked changes over periods of 1 minute. Smaller particles, such as those between 1 and 2 nm often possessed visible lattice fringes, but appeared to briefly transition into disordered states (Figure 7.13). Their size and shape remained constant on average over 1 minute. Particles which were smaller still (< 8 atoms) usually had elongated shapes and, in many cases, consisted of linear atom chains. They did not exhibit crystal-like ordering and moved rapidly between myriad disordered configurations (Figure 7.14). Analysis of the ultrahigh resolution TEM images of Pt20G4OH samples revealed that most (61%) of the particles were non-crystalline after 6 hr of UV irradiation, and about an 8% were crystalline and 31% meso-crystalline (possessing a fcc-like structure for at least $\frac{1}{4}$ of the observation time). It is important to note, that a large fraction of platinum atoms was still

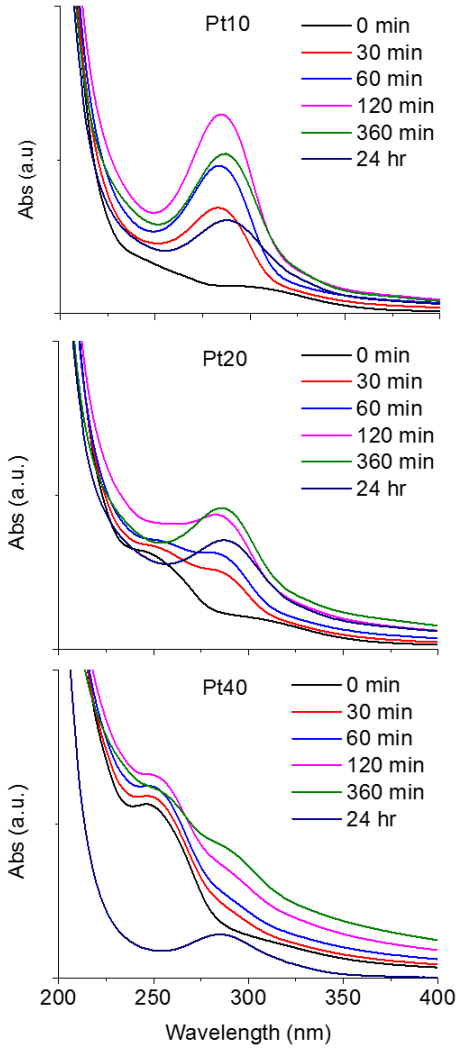

Figure 7.10: UV-Vis spectra of samples with Pt:G4OH ratios of 10 – 40 and their evolution with irradiation.

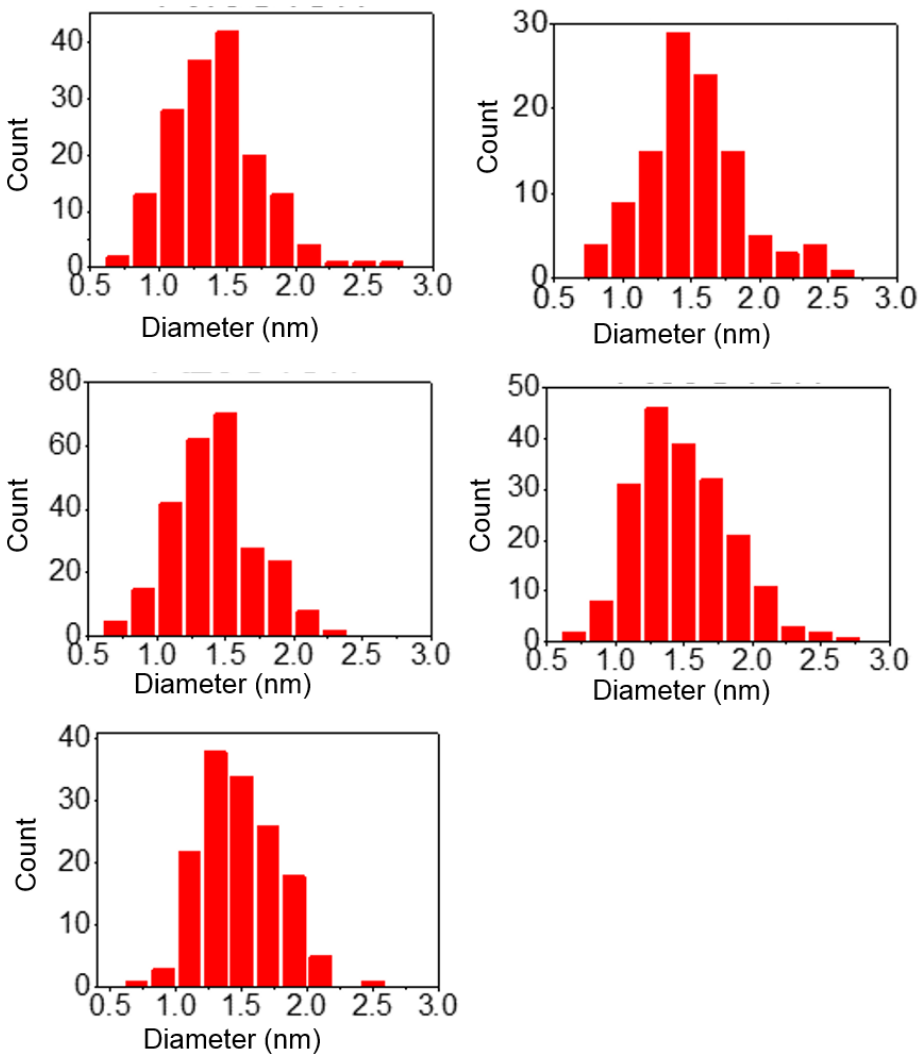

Figure 7.11: Size distributions of platinum nanoparticles synthesized using UV-induced synthesis in the PAMAM dendrimer for Pt:G4OH ratios of 10:1 to 60:1.

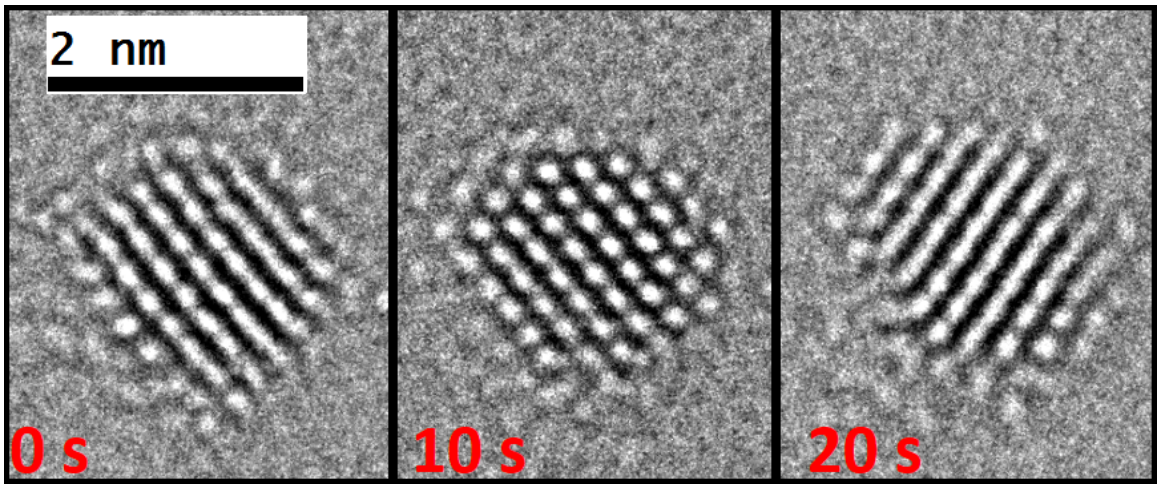

Figure 7.12: Ultrahigh resolution TEM images of a large particle whose shape and crystallinity are constant over time.

observable in the single atomic, PAMAM-coordinated form. This explains why our UV-Vis spectra have large peaks at 250 nm show that there still exist single Pt ions coordinated to PAMAM amide groups.

"Normal" HRTEM imaging was used to count larger numbers of particles and to investigate the dependence of the size on the UV irradiation time. After no irradiation, particles were not visible in HRTEM. After 15 minutes of irradiation, particles with diameters of 1.2 $\pm$ 0.3 nm were visible, but most appeared blurry, without resolvable lattice fringes. After 6 hours of irradiation the particles were still mostly blurry, but had increased slightly in size to about 1.4 nm. The particles we see in these TEM images are the same meso-crystalline and crystalline particles seen in ultrahigh resolution TEM, but the very small chains of platinum are invisible in this microscope.

The dependence of particle size on the Pt:G4OH ratio after extended irradiation (6 hr) was investigated. On average, the number of metal ions inside a dendrimer is the same as the Pt:G4OH ratio in solution. Many previous works have used the amount of metal ions in the dendrimer to control the particle size, because for most metals, the number of atoms in a particle is restricted to the number of ions that start complexed to a single dendrimer. In this case the average particle size remains remarkably constant at 1.45 $\pm$ 0.5 nm over a Pt:G4OH range from 10 to 60 (Figure 7.11). The standard deviation is also constant around 0.35 nm. Only for Pt_{80}G4OH does the average size change to 1.9 nm with a broader distribution (σ = 0.58 nm). The distribution of the Pt_{20}G4OH particles counted in HRTEM images is very similar to that obtained from ultrahigh resolution images. No particles larger than 5 nm were observed in any sample, which indicates that particle formation from platinum on outside of the dendrimer, as well as severe dendrimer degradation and particle aggregation, was successfully avoided.

Previous work has also shown that platinum in these systems can exist in a 'bimodal' distribution of particles, which are mostly metallic and another portion that are oxidized. These are likely the particles and the linear chains, respectively. We hypothesize that the 254 nm light is able to break the Pt-N bonds in the metal-dendrimer complex and the

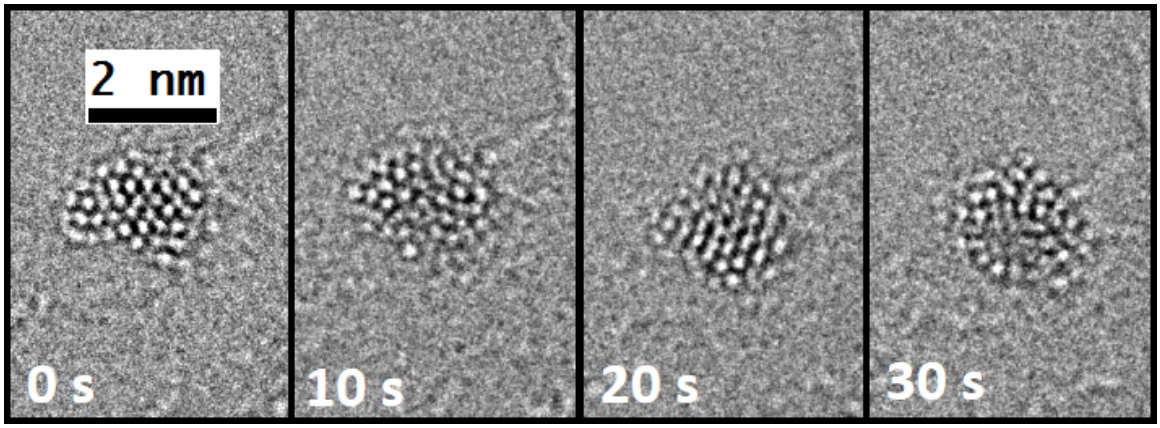

Figure 7.13: Ultrahigh resolution TEM images showing the mesocrystalline Pt particle transitioning through various crystalline (0 s, 20 s) and non-crystallne states.

atoms are able to form multinuclear ionic compounds of platinum ions coordinated with amide groups in the dendrimer - similar to "platinum blue" compounds which have been synthesized using amidate ligands[26,27]. With increasing exposure to UV light these linear chains may combine via oriented attachment to form very small, platinum aggregates, or mesoparticles, which oscillate between crystalline and non-crystalline. The mesoparticulate state is stable only below a critical number of atoms in the particle, beyond which the particles assume a crystalline state. Longer UV irradiation increases the number of these linear chains that aggregate within the G4OH causing an increase in the average size of the particles. However, their the oxidation state and capping agent electronic interaction thermodynamically stabilizes particles of $\sim$1.4 nm.

At the same time as "platinum-blue"-like compounds are formed, Pt^{2+} ions freed from their bonds in the dendrimer may also diffuse outside of the dendrimer under UV-light exposure, where it may form larger particles. Such a hypothesis explains the abrupt change in size distribution for Pt_{80} samples, because the formation of an 80-atom particle, for instance, is not favorable in a highly oxidized state, and therefore there is excess ionic Pt available for reduction outside of the dendrimer where particle size is not well controlled.

The key part of this method to controllably synthesize these mesoparticles may lie in the non-reducing nature of the UV irradiation. The ability of a particle to possess metallic properties depends on the number of atoms in the particle, because above a certain number of atoms, the system is stabilized by a phase transition from non-metallic to metallic[28]. For instance the critical threshold number of atoms necessary for platinum (with Fermi energy for metallic Pt of 5.5 eV) at room temperature should be approximately 300 atoms[29]. We hypothesize that the small size of the particles is maintained due to the lack of (or slow rate of) reduction of the particles in the dendrimer[30].

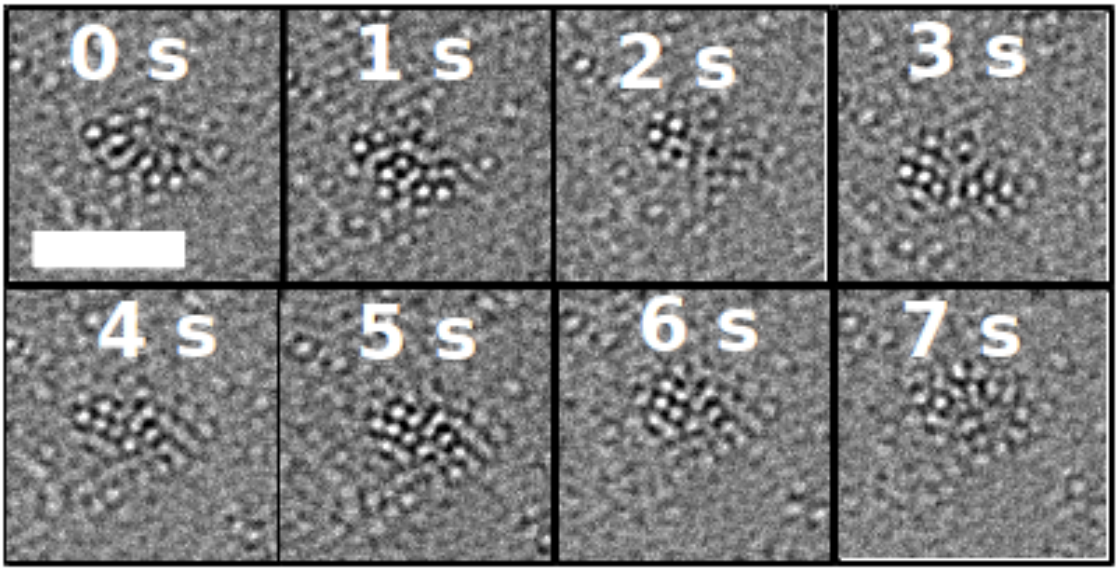

Figure 7.14: Ultrahigh resolution TEM images showing a very small particle fluidly moving between disordered structures. The scale bar in the top left image is 2 nm.

Conclusions

In this paper, we show that Pt^{2+} cations in PtG4OH strongly bond to amide nitrogen atoms, which form a coordination sphere around platinum with a strong stabilizing chelate effect. This accounts for the resistance of platinum to reduction by sodium borohydride. The diffuse-reflectance UV-vis spectra reveal the formation small Pt clusters, whose spectroscopic signature resembles platinum-blue binuclear and tetranuclear linear clusters. A spectroscopic study of thermal and photochemical decay of the capping stabilizer G4OH shows different mechanisms of stabilizer degradation.

We use the efficient release of platinum atoms from the dendrimer initiated by UV irradiation as a new mode of particle synthesis using the dendrimer template. Platinum particles formed under UV irradiation in the presence of PAMAM dendrimer leads to the formation of very small, nanoparticles via a route distinct to that of sodium borohydride reduction. Both high resolution TEM and ultrahigh resolution TEM show that the particles formed using this technique are non-crystalline, which gives them potentially different properties than larger, crystalline particles formed using the typical method with strong reducing agents.

References

[1] Astruc, D.; Chardac, F. *Chemical Reviews* **2001**, *101*, 2991–3023.

[2] Crooks, R.; Lemon, B.; Sun, L.; Yeung, L.; Zhao, M. *Dendrimers Iii: Design, Dimension, Function* **2001**, *212*, 81–135.

[3] Knecht, M.; Weir, M.; Myers, V.; Pyrz, W.; Ye, H.; Petkov, V.; Buttrey, D.; Frenkel, A.; Crooks, R. *Chemistry Of Materials* **2008**, *20*, 5218–5228.

[4] Deutsch, D.; Siani, A.; Fanson, P.; Hirata, H.; Matsumoto, S.; Williams, C.; Amiridis, M. *Journal Of Physical Chemistry C* **2007**, *111*, 4246–4255.

[5] Zhao, M.; Crooks, R. *Advanced Materials* **1999**, *11*, 217–+.

[6] Deutsch, D.; Lafaye, G.; Liu, D.; Chandler, B.; Williams, C.; Amiridis, M. *Catalysis Letters* **2004**, *97*, 139–143.

[7] Singh, A.; Chandler, B. *Langmuir* **2005**, *21*, 10776–10782.

[8] Witham, C.; Huang, W.; Tsung, C.; Kuhn, J.; Somorjai, G.; Toste, F. *Nature Chemistry* **2010**, *2*, 36–41.

[9] Borodko, Y.; Thompson, C.; Huang, W.; Yildiz, H.; Frei, H.; Somorjai, G. *Journal Of Physical Chemistry C* **2011**, *115*, 4757–4767.

[10] Alexeev, O.; Siani, A.; Lafaye, G.; Williams, C.; Ploehn, H.; Amiridis, M. *Journal Of Physical Chemistry B* **2006**, *110*, 24903–24914.

[11] Huang, W.; Kuhn, J.; Tsung, C.; Zhang, Y.; Habas, S.; Yang, P.; Somorjai, G. *Nano Letters* **2008**, *8*, 2027–2034.

[12] Borodko, Y.; Lee, H.; Joo, S.; Zhang, Y.; Somorjai, G. *Journal Of Physical Chemistry C* **2010**, *114*, 1117–1126.

[13] Borodko, Y.; Ager, J.; Marti, G.; Song, H.; Niesz, K.; Somorjai, G. *Journal Of Physical Chemistry B* **2005**, *109*, 17386–17390.

[14] Sakai, K.; Matsumoto, K. *Journal Of Molecular Catalysis* **1990**, *62*, 1–14.

[15] Siani, A.; Wigal, K.; Alexeev, O.; Amiridis, M. *Journal Of Catalysis* **2008**, *257*, 5–15.

[16] Weaver, J. *Physical Review B* **1975**, *11*, 1416–1425.

[17] Henglein, A.; Ershov, B.; Malow, M. *Journal Of Physical Chemistry* **1995**, *99*, 14129–14136.

[18] Lee, S.; Krimm, S., S Af Lee; Krimm, S. *Biopolymers* **1998**, *46*, 283–317.

[19] Ozturk, O.; Black, T.; Perrine, K.; Pizzolato, K.; Williams, C.; Parsons, F.; Ratliff, J.; Gao, J.; Murphy, C.; Xie, H.; Ploehn, H.; Chen, D. *Langmuir* **2005**, *21*, 3998–4006.

[20] Colthup, N.; Daly, L. *Introduction To Infrared And Raman Spectroscopy*; Academic Press, 1990.

[21] Murphy, W.; Zerbetto, F.; Duncan, J.; Mckean, D. *Journal Of Physical Chemistry* **1993**, *97*, 581–595.

[22] Goldfarb, T.; Khare, B. *Journal Of Chemical Physics* **1967**, *46*, 3379.

[23] Luo, X.; Imae, T. *J. Mater. Chem.* **2007**, 567.

[24] Bai, L.; Zhu, H.; Thrasher, J.; Street, S. *Acs Applied Materials and Interfaces* **2009**, *1*, 2304–2311.

[25] Einaga, H.; Harada, M. *Langmuir* **2005**, *21*, 2578–2584.

[26] Barton, J.; Best, S.; Lippard, S.; Walton, R. *Journal Of The American Chemical Society* **1978**, *100*, 3785–3788.

[27] Barton, J.; Caravana, C.; Lippard, S. *Journal Of The American Chemical Society* **1979**, *101*, 7269–7277.

[28] Landau, L.; Lifshitz, E. *Statistical Physics*; Pergamon Press, 1978.

[29] Kubo, R. *Journal Of The Physical Society Of Japan* **1962**, *17*, 975.

[30] Borodko, Y.; Ercius, P.; Pushkarev, V.; Thompson, C.; Somorjai, G. *Journal Of Physical Chemistry Letters* **2012**, *3*, 236–241.

Chapter 8

Comparison of isopropanol oxidation on platinum nanoparticles in the gas and liquid phases: Kinetics and sum-frequency generation spectroscopy

The chapter is a comparison of isopropanol (IPA) oxidation reaction on platinum nanoparticle catalysts in the gas and liquid phases. Reaction rate measurements reveal that the rate of alcohol oxidation in the liquid phase is much slower than in the gas phase and that the size dependence of the reaction rate is different for the two phases. The same enhancement of the reaction rate as described in chapter 4 is seen in these measurements, and the replacement of water with hexane, a neutral non-aqueous solvent, further verifies that water has an important role in the reaction. CH peaks in the SFG spectra of the platinum/isopropanol interface during these reactions have different intensities indicating a different orientation of the molecule on the catalyst. Orientational analysis based on a united atom model of the isopropyl group show that the isopropanol molecule on the surface may move from an orientation tilted toward the surface in the gas phase to one more perpendicular to the surface in the liquid phase.

Introduction

In catalysis, a challenge remains, which is the microscopic-scale comparison between the solid/gas interface and a solid/liquid interface. The challenge is largely technical, since gas phase studies have evolved along a trajectory using experimental measurement techniques that are largely separate from those used for the liquid phase. Gas phase measurements of catalytic surfaces evolved from vacuum techniques, such as low-energy electron diffraction, infrared reflection absorption spectroscopy, scanning tunnelling microscopy, x-ray photoelectron spectroscopy, temperature programmed desorption, and the like. On the other hand, liquid phase studies began mostly with electrochemical measurements, e.g. cyclic voltammetry, choronoamperometry, etc. and total internal reflection infrared spectroscopy. The reason for this split is the difficulty of studying the buried interface, which refers to an interface between two condensed phases. The low molecular density of the gas phase allows for the entrance and escape of optical/electron probes without the introduction of artifacts by by the bulk. In reality this is still limited to the regime of quite low pressure, but creative engineering of 'ambient pressure' photoelectron spectroscopy and STM promise to help researchers bridge the pressure gap. The liquid interface on the other hand precludes the use of almost all of these techniques. Sum-frequency generation remains one of the only techniques which can probe both interface in the same mode.

While the rates of reaction are expected to be far slower in the liquid phase due to the slow

mass diffusion to and from the catalyst surface, the difference in selectivity and dependence of the reaction rate on catalyst particle size and surface facet (particle shape) is not trivial to predict[1–5]. These changes, which to some extent do not strongly depend on the overall rate of diffusion, are good metrics by which to compare the two phases. Alcohol oxidation is an ideal reaction for comparing the gas and liquid phase catalysis. The reactants and products, ethanol and acetaldehyde in the case of this study, because of their room temperature liquid state and high vapor pressure, are easily used in both phases.

In this chapter, the catalytic properties of metal nanoparticles in the gas and liquid phase are compared[6]. The finding that not only the reaction rates, but also the size-dependent activity, are variable between phases is important, because it indicates that the mechanism of reaction or the state of the surface are vastly different between the two phases. Sum-frequency generation measurements are used to probe the nanoparticle surface and orientational analysis reveals that the orientation of the molecule on the metal surface is different in the two phases, possibly due to the high coverage of the surface by alcohol under very high 'effective pressure'.

Experimental details

Synthesis of Pt nanoparticles with various sizes

For 2 nm Pt nanoparticles, 100 mg of NaOH, 80 mg of $H_2PtCl_6{\cdot}6H_2O$ (∼0.2 mmol) and 110 mg of PVP (Mw = 29,000) were dissolved in 10 mL of ethylene glycol and the mixture was heated to 160 °C in an oil bath and held at that temperature for 2 h under argon atmosphere. The resulting nanoparticles were precipitated with 40 mL of acetone, separated by centrifuge and dispersed in 10 ml of ethanol. The nanoparticles were repeatedly washed by precipitating with hexane, centrifuging, and re-dispersing in ethanol before use. For 4 nm Pt nanoparticles, 50 mg of $H_2PtCl_6{\cdot}6H_2O$ and 220 mg of PVP (MW = 29,000) were dissolved in 10 mL of ethylene glycol and the mixture was heated to 180 °C in an oil bath and held at that temperature for 0.5 h under argon atmosphere. The resulting nanoparticles were precipitated with 40 mL of acetone and re-dispersed in 10 mL of ethanol. The nanoparticles were repeatedly washed by precipitating with hexane, centrifuging, and re-dispersing in ethanol before use.

For 6 nm Pt nanoparticles, 80 mg of platinum (II) acetylacetonate (∼0.2 mmol) and 55 mg of PVP (MW = 55,000) were dissolved in 5 mL of ethylene glycol. The solution was then heated to 200 °C in an oil bath and held at that temperature for 10 min under argon atmosphere. Cooled to room temperature, the resulting nanoparticles were precipitated with 45 mL of acetone and re-dispersed in 10 mL of ethanol. The nanoparticles were repeatedly washed by precipitating with hexane, centrifuging, and re-dispersing in ethanol before use.

For 8 nm Pt nanoparticles, 80 mg of platinum (II) acetylacetonate (∼0.2 mmol) and 110 mg of PVP (MW = 29,000) were dissolved in 10 mL of ethylene glycol. The solution was then heated to 200 °C in an oil bath and held at that temperature for 2 h under argon atmosphere. Cooled to room temperature, the resulting nanoparticles were precipitated with 40 mL of acetone and re-dispersed in 10 mL of ethanol. The nanoparticles were repeatedly washed by precipitating with hexane, centrifuging, and re-dispersing in ethanol before use.

Catalyst preparation

SBA-15 and MCF-17 were synthesized according to the literature[7,8]. Catalysts for liquid phase reactions were prepared by loading 2 or 4 nm Pt nanoparticles on SBA-15 with an average pore size of ∼10 nm and 6 or 8 nm Pt nanoparticles on MCF-17 with pore sizes in the range of 20-50 nm. Pt nanoparticles were mixed with the mesoporous silica support in ethanol and sonicated for 2 h. The products were collected by centrifuge and washed with ethanol for 3 times before they were dried at 60 °C in an oven. The amount of Pt loaded on silica was measured by inductively coupled plasma atomic emission spectroscopy. Catalysts for gas phase reactions were prepared by drop-casting ethanol dispersions of Pt nanoparticles on SiO_2 coated Si wafers.

Catalytic measurements

For liquid-phase catalysis, 3-10 mg of Pt/silica catalyst was dispersed in 2 mL of liquid containing certain amount of IPA. The mixture was then sealed in a 20 mL glass vial with magnetic stirring at a certain speed and kept at a certain temperature in an oil bath. After 2 h of reaction, the vial was cooled to room temperature and the catalyst was removed from the liquid by centrifuge. The supernatant was injected into a gas chromatography (GC) with a flame ionization detector to analyze the reaction conversion, namely the ratio between acetone and IPA.

Liquid-phase oxidation of IPA was carried out in sealed vials where the dissolved oxygen in the liquid was used as a reactant with the sealed gas-phase air as a reservoir. Conversion of oxygen (the limiting reactant) was typically kept below 20% so that the oxygen concentration in liquid did not undergo significant decrease throughout the reaction. Pt nanoparticles loaded into mesoporous silica were used as catalysts. Reaction rates were normalized to the number of surface Pt atoms assuming the density is the same as that of a Pt (111) single-crystal surface.

For gas-phase catalysis, the reactions were carried out in a batch-mode reactor equipped with a boron nitride substrate heater and a metal bellows circulation pump for gas mixing. The reactor was typically filled with 10 Torr of IPA, 50 Torr of oxygen and 710 Torr of helium at 60 °C. The products were detected by a GC with a flame ionization detector. The number of active sites for each catalyst was measured from an ethylene hydrogenation reaction with 100 Torr of H_2 and 10 Torr of ethylene at 25 °C following the IPA oxidation reaction. A turnover frequency of 11.7 molecules·site^{-1}·s^{-1} for ethylene hydrogenation on Pt surface was used to calculate the number of Pt active sites for the nanoparticle catalysts[5].

SFG measurements

SFG experiments were carried out in a system described previously[9]. A mode-locked Nd:YAG laser (Continuum Leopard D10, 20 ps, 20 Hz, 1064 nm) was used to pump frequency conversion stages to generate two pulses, a visible pulse (532 nm, 130 μJ) and a tunable mid-IR pulse (2800 cm^{-1} to 3600 cm^{-1}, 200 μJ). These pulses were overlapped on at 62° (visible) and 45° (mid-IR) on the sample (platinum nanoparticles) which had been deposited on the bottom of a quartz prism. Experiments were performed in the ppp polarization combination. The reflected component of SFG was collected and detected using a photomultiplier tube

with a gated integrator unit. Data points in spectra shown in this paper were an average of 100 measurements each. Samples were prepared by depositing Langmuir-Blodgett films of silica embedded 4 nm Pt nanoparticles on sapphire prisms followed by calcination in air at 550 °C for 3 h. To prepare 4 nm Pt nanoparticles embedded in silica, 300 μL of Pt nanoparticle ethanol suspension (∼4 mg/mL) and 5.0 μL of tetraethyl orthosilicate were mixed with 15 mL of ethanol, to which 2.25 mL of ammonium hydroxide was added drop-wise within 5 min under stirring. The mixture was then sonicated for 2 h. The product was precipitated by hexane and collected by centrifugation.

For gas phase SFG measurements, pure oxygen was bubbled through isopropanol and sent through the SFG cell at 18 °C. In liquid phase measurements liquid isopropanol was passed through the cell using a peristaltic pump.

Results and Discussion

Nanoparticle synthesis

TEM imaging of the synthesized nanoparticles shows their uniform size and spherical shape. The average diameters for the nanoparticles were approximately 2 nm for the ethylene glycol synthesis with PVP as a capping agent in the presence of NaOH and 4 nm in the similar synthesis in the absence of NaOH. The synthesis using a method with platinum(II)acetylacetonate resulted in particles with a diameter of 6 nm and 8 nm depending on the reaction time. Figure 8 shows the resultant particles from the four synthetic protocols. The uniform size distribution of colloidally synthesized nanoparticles is ideal for size-dependent studies in catalysis.

Liquid phase isopropanol oxidation kinetics

Because the cleavage of CC bonds is slow at the temperatures typically used for alcohol oxidation the liquid phase, secondary alcohols, such as isopropanol, yield acetone as the only major product in these reactions. While the selectivity was constant with particles size, the activity of the catalyst varied greatly as particle sized was changed. In pure isopropanol with 1.6 mM oxygen the turnover frequency (TOF) of IPA oxidation on 2 nm platinum particles was calculated to be 0.046 s^{-1} (Figure 8a). The turnover frequency refers to the number of acetone molecules created per active platinum site per unit time. On 4 nm particles the TOF increased to 0.084 s^{-1}, and the rate continued to increase as size increased to 6 and 8 nm, which had TOFs of 0.168 and 0.302 s^{-1}, respectively. A similar trend has been reported for platinum nanoparticles in electrochemical oxidation of methanol and oxygen reduction[10–12]. Platinum nanoparticles of very small sizes are known to be more susceptible to oxidation which could be the cause of the lower turnovers for the 2 and 4 nm particles here[13,14]. Another possible explanation is the poisoning of the highly reactive corner and edge atoms, both of which exist in higher numbers on smaller particles, by their strong binding with oxygen or other species.

The temperature dependence of the reaction rate was investigated for isopropanol oxidation in mixtures of isopropanol in water and hexane and with neat isopropanol. In pure IPA the activation energy was found between 54 and 62 kJ/mol and did not change with particle size. In hexane/IPA mixture the activation energy was slight lower and still size

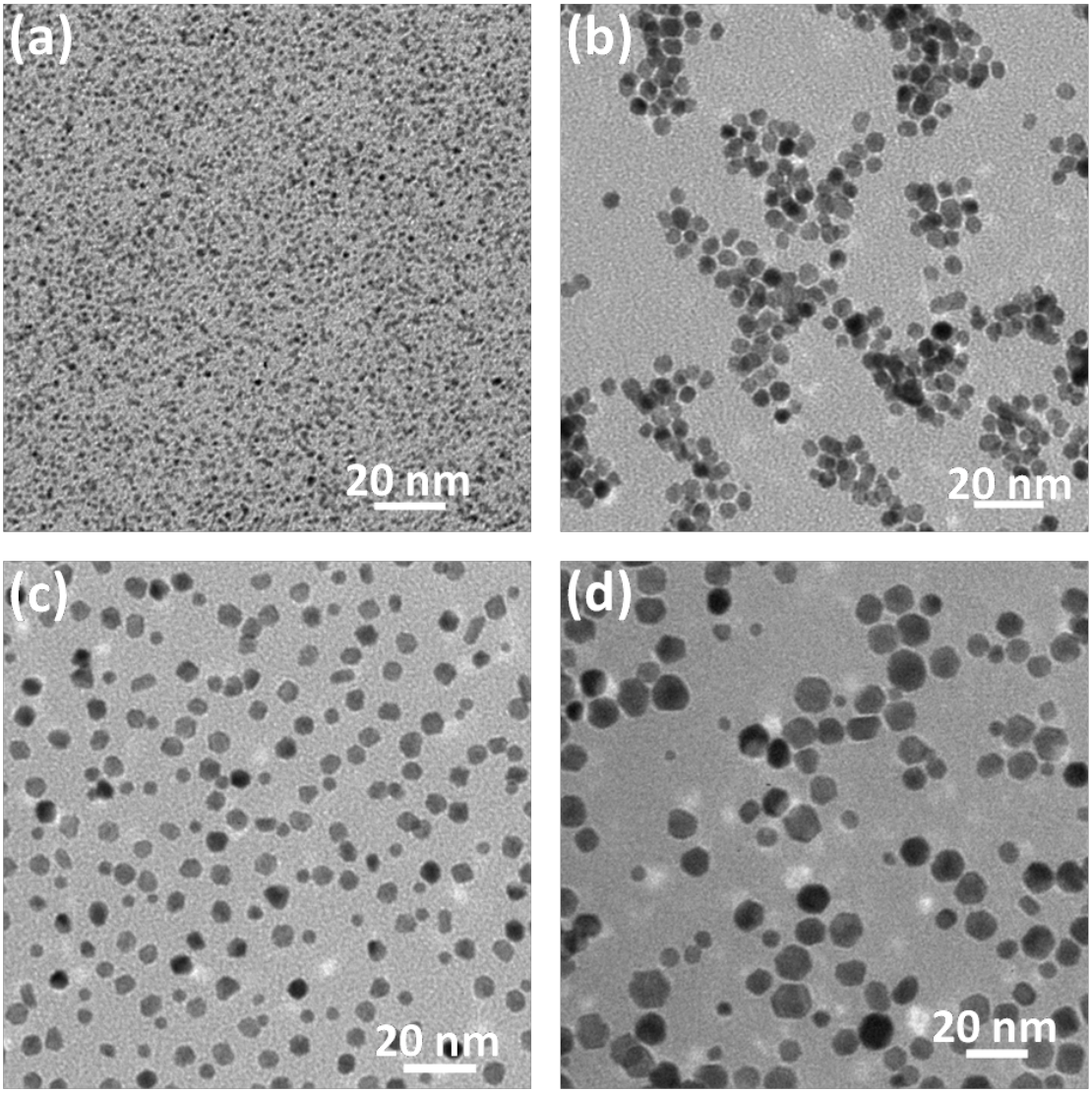

Figure 8.1: TEM images of synthesized Pt nanoparticles with average sizes of (a) 2 nm synthesized by reduction in ethylene glycol with NaOH, (b) 4 nm synthesized by reduction in ethylene glycol without NaOH, (c) 6 nm synthesized from Pt(II) acetylacetonate and (d) 8 nm also synthesized from Pt(II) acetylacetonate.

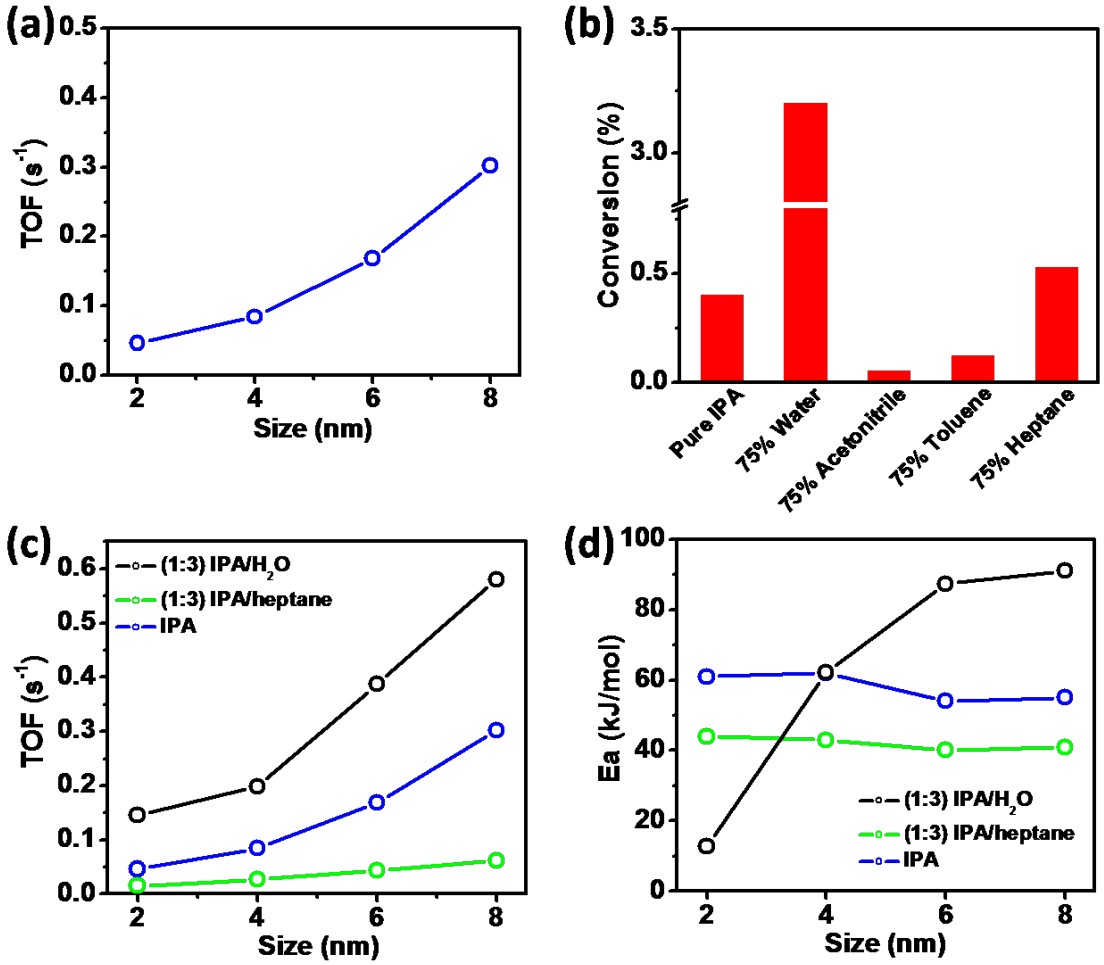

Figure 8.2: Liquid-phase IPA oxidation reaction. (a) TOF in pure IPA catalyzed by Pt nanoparticles with various sizes at 60 °C. (b) Reaction conversion in pure IPA and IPA diluted with various solvents, catalyzed by 4 nm Pt nanoparticles at 60 °C. (c) Comparison of size-dependent TOF in pure IPA and IPA diluted with water and heptane at 60 °C. (d) Comparison of reaction activation energy in pure IPA and IPA diluted with water and heptane, catalyzed by Pt nanoparticles with various sizes at 60 °C.

independent (Figure 8d). Mixture of water and IPA stood out in that the particle size had a large effect on the activation energy, suggesting that the presence of water changed the rate limiting step - either by changing the relative rates of elementary steps, or by introducing a new reaction mechanism altogether. The activation energy for 2 nm platinum particles was only 13 kJ/mol and increased to 62 kJ/mol with an increase in particle size to 4 nm. At 6 and 8 nm, the activation energy further increased to 88 and 91 kJ/mol.

To investigate the use of solvent in the reaction, mixtures of isopropanol in hexane and water at ratios of 1:3 were compared to pure isopropanol. For this comparison, 4 nm particles were used. Dilution with water resulted in an increase of the rate of reaction by a factor of ∼8. The studies of alcohol oxidation on evaporated platinum films in chapter 4 has shown that water can cause rate enhancement in the oxidation reaction. This has been reported in several other publications as well[15,16]. The use of acetonitrile and toluene as solvents substantially lowered catalytic activity. Figure 8b shows the effects of the solvent on the reaction rate. It is possible that, in the case of acetonitrile, the strong interaction of the electron donor with the platinum surface causes blockage of the active sites. Toluene may have a similar inhibiting effect due to interaction of π electrons with the surface or by true chemisorption. Catalysts in heptane, a molecule without a π electron system, had similar turnovers as those in pure IPA, meaning that hexane may serve well as a neutral solvent. The size dependence for IPA mixtures with water and hexane had similar particle size dependences as pure IPA (Figure 8c).

Gas phase isopropanol oxidation

Gas-phase oxidation of IPA was performed in a batch mode reactor with Pt nanoparticles deposited on SiO_2 substrates as catalysts. With 10 Torr of IPA and 50 Torr of O_2 as reactants at 60 °C, a weaker dependence of catalytic activity on nanoparticle size was observed for the Pt catalysts than in the liquid-phase reaction. The reaction rate was similar across all particle sizes, except for 2 nm which exhibited a lower activity (Figure 8a)

Previous X-ray photoelectron spectroscopy (XPS) studies revealed that at 2 nm, platinum nanoparticles are not fully metallic, and can be easily oxidized. Larger nanoparticles are fully metallic. Particle oxidation could be the cause for the uniqueness of 2 nm particles in the gas phase reaction rates. In the gas phase, the concentration if IPA is far lower than in the liquid phase. 50 Torr O_2 corresponds to a molarity of 0.48 mM, 5 order of magnitude lower than the liquid molarity. The oxygen concentration in the gas phase remained comparable with pure liquid IPA in terms of molarity. In spite of the lower concentration, the reaction rates in the gas phase were 10-40 times higher than in the liquid phase. This is shown in Figure 8a. Decreasing the alcohol concentration in the liquid phase by diluting the alcohol with hexane resulted in an overall rate decrease compared to the gas phase by 400-1100 times. This can be explained by mass transfer effects.

The effect of water on the reaction rate in the gas phase was a strong inhibition of the reaction, in contrast to its effect in in the liquid phase. When 2 Torr of water vapor was introduced into the reaction system to give a water/IPA molar ratio of 1 : 5, the IPA oxidation TOF decreased by 40% (Figure 8b).

The very different role played by water in the liquid phase and the gas phases suggests different reaction pathways for IPA oxidation at the two interfaces. The liquid-phase reaction

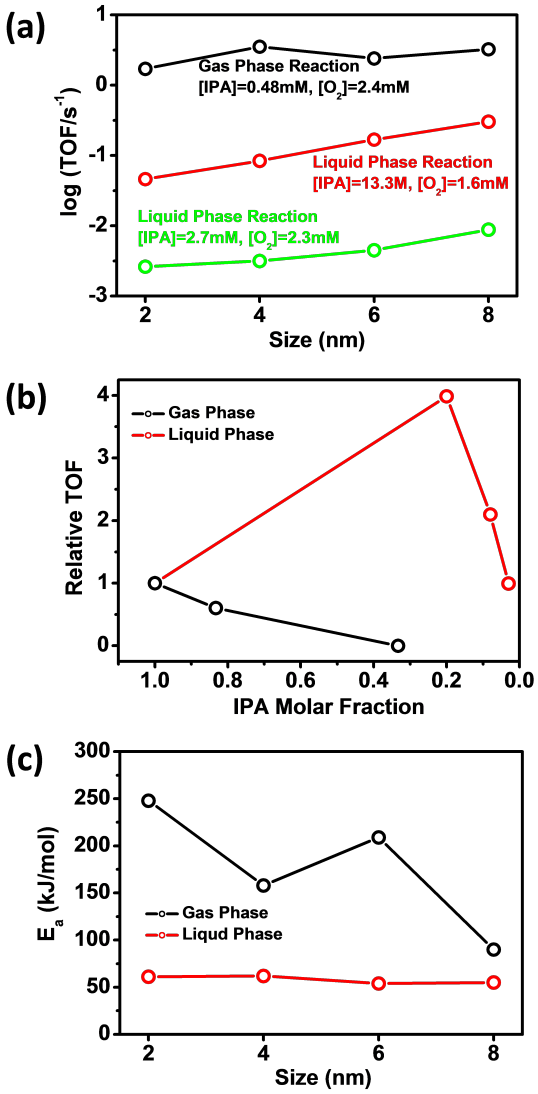

Figure 8.3: Gas-phase IPA oxidation reaction. (a) Size-dependent TOF in the gas-phase reactions compared to that in the liquid-phase reactions in pure IPA and IPA diluted with heptane. (b) Dependence of catalytic activity on water incorporation in the gas-phase and liquid-phase IPA oxidation reactions catalyzed by 4 nm Pt nanoparticles at 60 °C. (c) Size-dependent reaction activation energy for the gas-phase IPA oxidation reaction compared with that for the liquid-phase reaction in pure IPA.

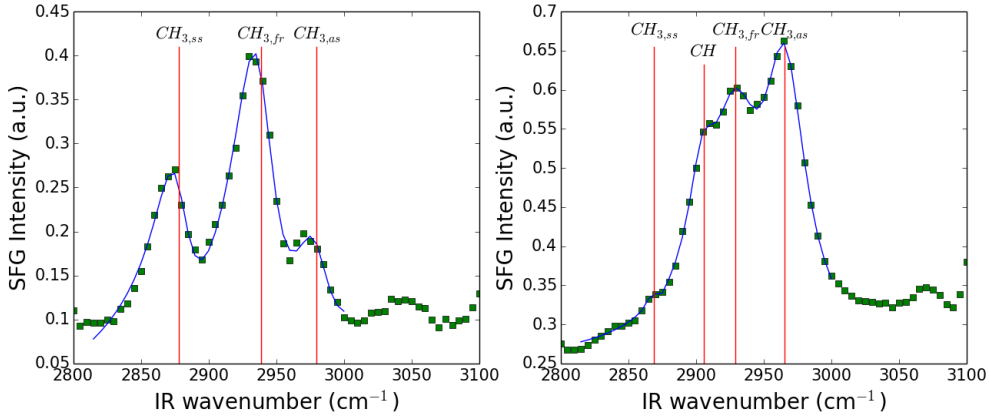

Figure 8.4: SFG vibrational spectra of pure IPA obtained on the surface of 4 nm Pt nanoparticles under gas-phase and liquid-phase reaction conditions. The results of the fitting procedure is shown by the blue line. The vertical red lines mark the frequencies of symmetric stretch ($CH_{3,ss}$ 2870 cm^{-1}), CH stretch (2905 cm^{-1}), the Fermi resonance mode ($CH_{3,fr}$ 2940 cm^{-1}), and asymmetric stretch ($CH_{3,as}$ 2970 cm^{-1}) of the isopropyl moiety.

process was dominated by IPA dehydrogenation on the Pt surface. Water could stabilize the intermediates and thus promote the reaction. For the gas-phase reaction, it is possible that both IPA and oxygen need to be adsorbed on the catalyst surface. Water vapor might compete for the active sites with IPA or oxygen and therefore lower the reaction rate. The mechanistic differences between the liquid-phase and gas-phase reactions were also revealed by study of temperature-dependent catalytic activity. The reactions in the gas phase exhibited significantly higher activation energy with stronger dependence on the size of Pt nanoparticles than the liquid-phase reactions. Unlike the liquid-phase reaction where the activation energy was between 54 and 62 kJ/mol and not significantly influenced by the size of the Pt nanoparticles, the gas-phase reaction over 2 nm Pt nanoparticle catalyst showed activation energy as high as 248 kJ/mol which decreased considerably with the increase of Pt nanoparticle size (Figure 3c). The activation energy for the gas-phase reaction over 8 nm Pt nanoparticles was 90 kJ/mol, still much higher than that for the liquid-phase reaction.

Sum-frequency generation of isopropanol on nanoparticles in the liquid and gas phases

SFG vibrational spectroscopy was used to probe the adsorbed molecules on Pt nanoparticles under IPA oxidation reaction conditions in both the gas phase and the liquid phase. Under the gas-phase reaction condition, three vibrational features were observed on the surface of 4 nm Pt nanoparticles, corresponding to symmetric stretch ($\sim$2875 cm^{-1}), Fermi resonance mode ($\sim$2940 cm^{-1}), and asymmetric stretch ($\sim$2970 cm^{-1}) of the methyl groups in IPA species (Figure 8). In the liquid phase, increased intensity for the asymmetric stretch and decreased intensity for the symmetric stretch of IPA species were detected on 4 nm Pt nanoparticle surface (Figure 8), indicating different conformations of IPA species at the solid/liquid interface than the solid/gas interface.

The basics of orientational analysis is covered in this work in chapter 2, and orientational

analysis for methyl groups have been discussed thoroughly by Wang[17]. Isopropanol presents a slightly more complicated analysis due to its having two methyl groups. One way to account for two methyl groups on a molecule is to assume their fixed orientation with respect to one another, and calculate the molecule's susceptibility from the sum of the non-linear susceptibilities of the individual methyl groups[18]. Orientational analysis for isopropanol has also been considered by Kataoka *et al.* using a united atom approach[19]. The united atom method utilizes symmetry arguments to describe the collective contributions of the IPA methyl groups to the SFG signal by a non-linear susceptibility of the entire isopropyl group with C_{2v} symmetry. Their work includes explicit derivations of the susceptibility elements in lab coordinates as a function of the Euler angles describing the orientation of the isopropyl group[19] with respect to the surface. Here their method is used to calculate the orientation of the isopropanol molecule from the ratio of intensities of the CH_3 asymmetric and symmetric stretching peaks. The Fresnel factors were calculated using equations in chapter 2, taking the refractive index of quartz to be 1.46, of air to be 1.00, of isopropanol in the visible to be 1.38 and in the IR to be 1.31. An average of the refractive indices of quartz and air or isopropanol was used for the interfacial refractive index in the calculation of L_{zz}. We take the ratio of the non-linear susceptibility elements of the methyl groups β_{aac}/β_{ccc} to be the same as the accepted value for ethanol, which is 3.4. Also, the value of β_{caa}/β_{ccc} was calculated from the Raman depolarization ratios as described in the work of Wang *et al.*

The orientation of the isopropyl group is fully described by the three Euler angles, θ, ϕ, and χ. These are the tilt angle to the surface normal of the vector bisecting the C-C bonds in the isopropyl group, the rotational angle of the C-C-C plane with respect to a plane perpendicular to the surface, and the rotation of the bisector around the surface normal. Since the surface possesses $C_{\infty v}$ symmetry, total isotropy in the χ coordinate - rotation of the molecule around the surface normal - is assumed. Thus the molecule can be described by just θ and ϕ. With only the *ppp* polarization combination it is not possible to determine the value of these parameters absolutely, but the value of θ can be calculated for an assumed value of ϕ, for instance. Figure 8.5 shows the intensity ratio as calculated by the united atom method as a function of θ for a number of assumed values of ϕ, which are shown in the legend. Here a low value of θ describes a molecule with its isopropyl group pointing up from the surface ('standing up') and a high value represents a molecule close to the surface ('lying down'). A high value of ϕ describes an isopropyl group with its two methyl groups equidistant to the surface (' surface parallel'), and a low value describes the group rotated perpendicular to the surface ('surface perpendicular'). The bold blue horizontal lines in Figure 8.5 are the values of the ratio from our experimental data, 0.24 for the gas phase conditions, and 38 for the liquid phase conditions. Figure 8.6 is a map of possible orientations which would reproduce our spectral intensities to within 20%. It can be seen that in the liquid phase, the isopropyl group is surface-perpendicular and standing up, while in the gas phase the orientation of the molecule is not as defined, a variety of orientations is possible, based on our SFG data. The plot in Figure 8.6 shows that the molecule may be standing up or it could be lying parallel to the surface with a very high tilt angle. Cartoons of the relative orientations of the molecules in the gas phase and liquid phases are shown in Figure 8.6. We attribute this change in conformation to higher surface coverages of the alcohol at higher molecular densities in the liquid phase. Such differences are likely to be responsible for the observed distinctive kinetics of the liquid-phase and gas-phase reactions.

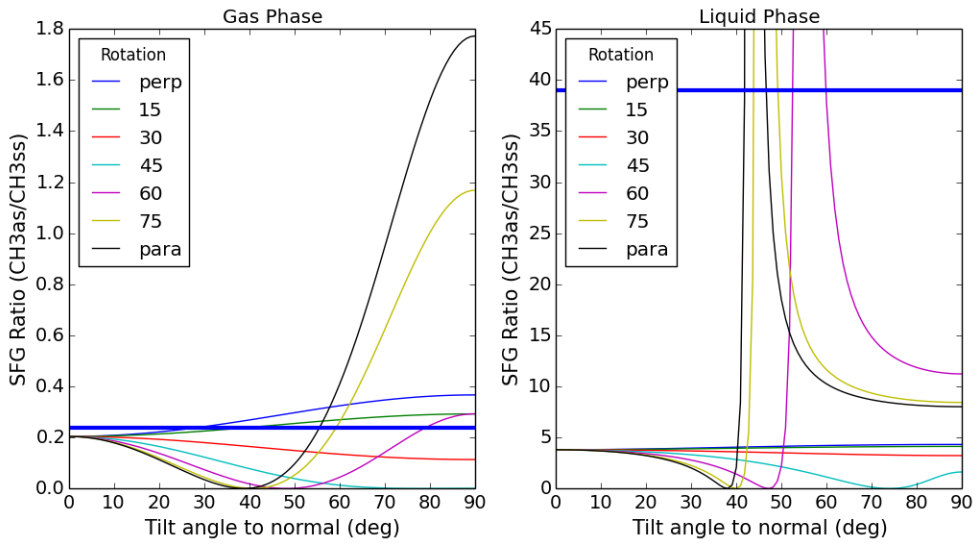

Figure 8.5: The ratio of intensities of the CH_3 asymmetric stretch mode (2970 cm^{-1}) to the CH_3 symmetric stretch mode (2870 cm^{-1}) for isopropanol using the united atom model. The rotational angle, ϕ, is listed in the legend. The ratios obtained by experiment are given by the thick blue horizontal lines. Left: the ratio using Fresnel factors for the gas phase system. Right: the ratio using Fresnel factors for the liquid system.

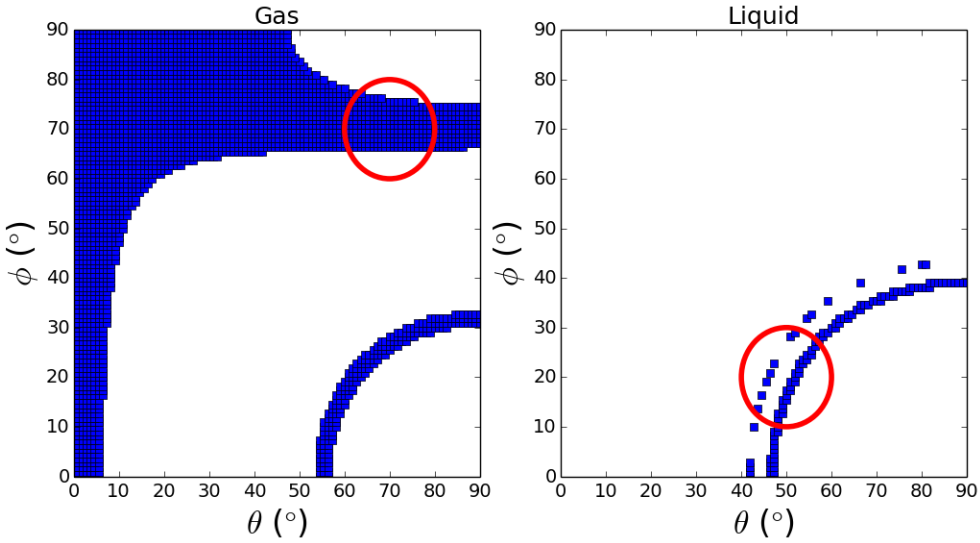

Figure 8.6: Orientation maps showing the orientations of the isopropyl group of IPA which would have a methyl asymmetric/methyl symmetric intensity ratio within 20% of the data obtained by SFG. On the left, the possible range of orientation in the gas phase is colored in blue. On the right, the orientations obtained from the liquid phase data are plotted.

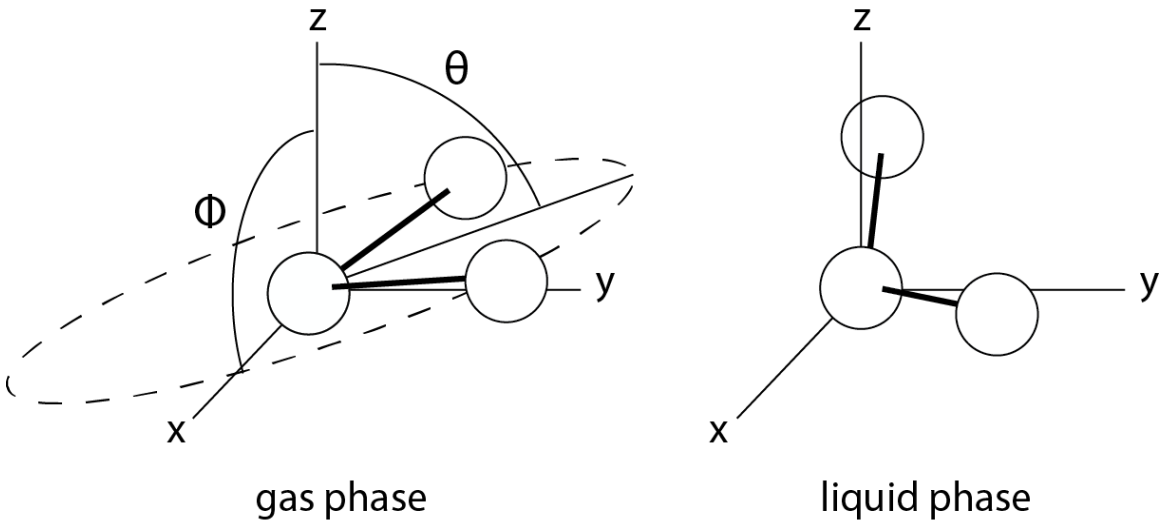

Figure 8.7: Graphical depictions of the orientation of the isopropyl group of IPA in the gas and liquid phase. The cartoons are plotted to depict orientations from the encircled regions in Figure 8.6.

Conclusions

We have studied the IPA oxidation reactions catalyzed by Pt nanoparticles with tunable sizes in both the liquid phase and the gas phase. The liquid-phase reaction differs from the gas-phase reaction in reaction rate, dependence of catalytic activity on nanoparticle size, effect of water addition, activation energy, and dependence of activation energy on nanoparticle size. The results indicate different kinetic processes at the solid/liquid interface vs the solid/gas interface for the same reaction.

A comparison of sum-frequency generation measurements of platinum surfaces in the liquid and the gas phase show a very different ratio of asymmetric and symmetric stretching intensities. These intensity ratios indicate a different configuration of the molecule with respect to the surface. Calculations based on SFG theory show that isopropanol is standing up more under liquid phase conditions than under gas phase conditions. Such a difference in conformations may be the cause or the effect of very different reaction pathways, which correlates with our kinetic results.

References

[1] Grass, M. E.; Rioux, R. M.; Somorjai, G. A. *Catalysis Letters* **2009**, *128*, 1–8.

[2] Rioux, R. M.; Hsu, B. B.; Grass, M. E.; Song, H.; Somorjai, G. A. *Catalysis Letters* **2008**, *126*, 10–19.

[3] Kuhn, J. N.; Huang, W.; Tsung, C.-K.; Zhang, Y.; Somorjai, G. A. *Journal Of The American Chemical Society* **2008**, *130*, 14026.

[4] Pushkarev, V. V.; Musselwhite, N.; An, K.; Alayoglu, S.; Somorjai, G. A. *Nano Letters* **2012**, *12*, 5196–5201.

[5] Wang, H.; Wang, Y.; Zhu, Z.; Sapi, A.; An, K.; Kennedy, G.; Michalak, W. D.; Somorjai, G. A. *Nano Letters* **2013**, *13*, 2976–2979.

[6] Wang, H.; Sapi, A.; Thompson, C.; Zherebetskyy, D.; Wang, L.; Krier, J.; Somorjai, G. *In Preparation*

[7] Zhao, D.; Huo, Q.; Feng, J.; Chmelka, B.; Stucky, G. *Journal Of The American Chemical Society* **1998**, *120*, 6024–6036.

[8] Schmidt-Winkel, P.; Lukens, W.; Zhao, D.; Yang, P.; Chmelka, B.; Stucky, G. *Journal Of The American Chemical Society* **1999**, *121*, 254–255.

[9] Thompson, C.; Carl, L.; Somorjai, G. *Journal Of Physical Chemistry C* **2013**, *49*, 26077–26083.

[10] Joo, S. H.; Kwon, K.; You, D. J.; Pak, C.; Chang, H.; Kim, J. M. *Electrochimica Acta* **2009**, *54*, 5746–5753.

[11] Shao, M.; Peles, A.; Shoemaker, K. *Nano Letters* **2011**, *11*, 3714–3719.

[12] Tritsaris, G. A.; Greeley, J.; Rossmeisl, J.; Norskov, J. K. *Catalysis Letters* **2011**, *141*, 909–913.

[13] Mallat, T.; Baiker, A. *Catalysis Today* **1994**, 247.

[14] Mallat, T.; Baiker, A. *Chem. Rev.* **2004**, 3037.

[15] Akpa, B.; D'Agnostino, C.; Gladden, I.; Hindle, K.; Manyard, H.; McGregor, J.; Li, R.; Neurock, M.; Sinha, N.; Stitt, E.; Weber, D.; Zeitler, J.; Rooney, D. *J. Catal.* **2012**, 30.

[16] Chibani, S.; Michel, C.; Delbecq, F.; Pinel, C.; Besson, M. *Catal. Sci. Technol.* **2013**, 339.

[17] Lu, R.; Gan, W.; Wu, B.; Zhang, Z.; Guo, Y.; Wang, H. *Journal Of Physical Chemistry B* **2005**, *109*, 14118–14129.

[18] Chen, H.; Gan, W.; Wu, B.; Wu, D.; Zhang, Z.; Wang, H. *Chemical Physics Letters* **2005**, *408*, 284–289.

[19] Kataoka, S. *J. Am. Chem. Soc.* **2006**, 5516.

Chapter 9

An SFG study of interfacial amino acids at the hydrophilic SiO_2 and hydrophobic deuterated polystyrene surfaces

Introduction

Biointerfaces, the region of interaction between living organisms and synthetic materials, is an active and growing area of research important to the development of myriad biotechnologies. Devices interfacing with the body, which include stints and contact lenses, rely critically on the host organism's acceptance of the material as benign, a process which depends on the adsorption of biological molecules (proteins etc.) on their surfaces. Studying the modes of adsorption of small, simple molecules like amino acids at the interface of water and a solid is a tractable method for understanding the fundamental factors governing the body's response to the introduction of a medical device. We have used sum-frequency generation to determine the interactions of amino acids on hydrophilic and hydrophobic surfaces with the solid/liquid interface[1–3]. While the system is very different from the catalytic surfaces discussed in the rest of this work, the concepts applied here are identical. In this chapter, the SFG investigation of eigth amino acids, L-phenylalanine, L-leucine, glycine, L-lysine, L-argnine, L-cysteine, L-alanine and L-proline on silica and polystyrene surfaces is discussed. These surfaces serve as models for the surfaces of all materials which lie somewhere on the spectrum of hydrophilicity[4].

Experimental details

SFG measurements

SFG measurements were performed using a Continuum Leopard Nd:YAG laser with 20 ps pulses at 1064 nm. These were converted using a commercial OPG/OPA system to 532 nm and tunable mid-IR pulses (2800-3600 cm^{-1})[3,5–8]. These pulses were incident on the sample at 65° and 42°, respectively. The prism substrates were placed on top of an o-ring filled with pH 7.4 phosphate buffered saline (PBS)/biomolecule solution in a clean Petri dish. All measurements were conducted in *ssp* polarization, referring to surface parallel polarizations of SFG and visible pulses and surface perpendicular polarization of IR light. The data points in spectra shown in this work are the averages of 400-600 shots.

Quartz crystal microbalance measurements

QCM was used to confirm the presence of amino acids adsorbed at the SiO_2 surface. A Q-Sense D300 instrument was used with SiO_2 QCM sensor crystals. The Sauerbrey equation and third harmonic of the resonant frequency were used to relate the frequency change to the adsorbed mass. The sensitivity of the instrument was approximately 2 nm/cm^2 which is approximately 1/10 of a monolayer.

SFG sample preparation

SiO_2 prisms were prepared by cleaning in concentrated H_2SO_4/No-Chromix solution for 12 h prior to use. Prisms were rinsed in deionized water and cleaned using oxygen plasma treatment (Herrick, Ithaca, NY) for 60 s. The O_2 plasma treatment was used to remove residual organic surface contaminants and maximize SiO_2 surface oxidation.

Polystyrene surfaces were prepared using a prism cleaned as described above. Thin films of d_8-polystyrene (MW $\approx$ 300,000, Polymer Source) were prepared by spin coating the prisms with a solution of the deuterated polystyrene dissolved in toluene at 3% w/w. The spin coated prisms were annealed at 100 °C for 12 hr to ensure surface flatness. The thickness of the films so prepared was determined to be 105 nm by ellipsometry.

Results and discussion

SFG spectra

SFG spectra of aqueous interfaces in the region between 2800-3600 cm^{-1} contained broad OH stretching features centered at 3200 and 3400 cm^{-1}. The 3200 cm^{-1} peak is frequently referred to as the "ice-like" water peak and the peak at 3400 cm^{-1} is referred to as the "liquid-like" water peak. These terms refer to the extent of hydrogen bonding between water molecules[9–13].

Above 3000 cm^{-1}, the spectrum may also contain contributions from amino acids used in this study. At pH 7.4 the amino acids studied here are zwitterionic. The NH_3^+ group can have two stretching modes near 3030 cm^{-1} and 3450 cm^{-1}[14]. Cyclic dimers of amino acids are known to have spectral features in this region as well[15]. Amino acids with amines on their side chain may have additional features in these region as well, due to NH_2 stretching modes[16].

amino acid	concentration (mg/mL)	interface	adsorbed mass (ng/cm^2)	95% CI (ng/cm^2)
L-phenylalanine	5	PS	57	4
L-phenylalanine	5	SiO_2	63	4
L-arginine	15	SiO_2	196	20
L-alanine	40	PS	469	33
L-cysteine	35	SiO_2	245	22

Table 9.1: Adsorbed mass at the aqueous liquid-solid interface determined by QCM

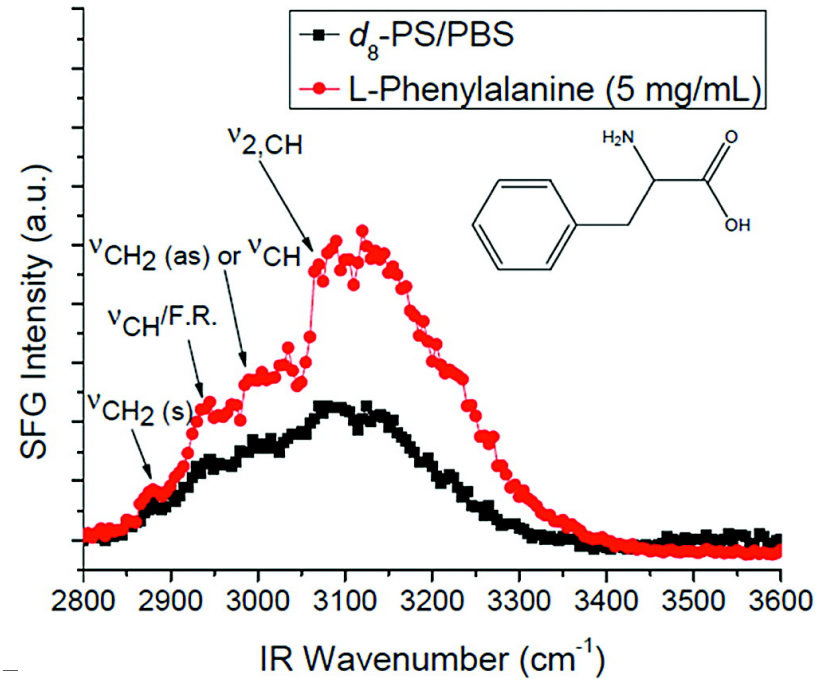

Figure 9.1: SFG spectrum of d_8PS/PBS interface before (black squares) and after (red circles) addition of phenylalanine (5 mg/mL). The vibrational modes at 2875 and 2939 cm^{-1} are attributed to CH_2 symmetric and a CH combination band/Fermi resonance, respectively. The peak at 2991 cm^{-1} is identified as a CH combination band or a CH_2 asymmetric stretch. Finally, the largest peak at 3049 cm^{-1} is indicative of the aromatic CH $\nu 2$ stretch of the amino acid phenyl side chain.

SFG of the hydrophobic deuterated polystyrene interface

Control spectra of phosphate buffered saline at the d_8-polystyrene interface is presented as background spectra in Figures 9.2-9.9. These spectra possess a broad, low-intensity feature centered around 3100 cm^{-1}. This feature, which has been noted and discussed in prior work, we attribute to a continuum of OH stretching modes and is consistent with previous studies at the d_8-polystyrene/water interface[3,5,6,8,17,18].

The SFG spectrum of L-phenylalanine in PBS at the hydrophobic interface is shown in Figure 9.1. The addition of L-phenylalanine to the system causes an enhancement of the SFG signal of water. The change of the spectrum upon addition of amino acid to the solution is a sign that the amino acid is present at the interface. Four CH vibrational peaks could be fit in this spectrum at 2875, 2939,2991 and 3049 cm^{-1}. These are attributed to the $CH_{2,ss}$, $CH_{2,fr}$ of the carbon atom directly connected to the phenyl ring in phenylalanine[1]. The peak at 2991 cm^{-1} is assigned to a combination band or $CH_{2,as}$ mode citeHall2010. Features above 3000 cm^{-1} can be attributed to the phenyl group, as very few aliphatic CH stretching modes are observed in this region, and aromatics are known to have spectral features here. QCM measurements indicated an adsorbed mass of 57 $\pm$ 4 ng/cm^2 at this interface. All QCM results are shown in Table 9.1.

The spectrum of L-leucine at the polystyrene interface is shown in Figure 9.2. Three

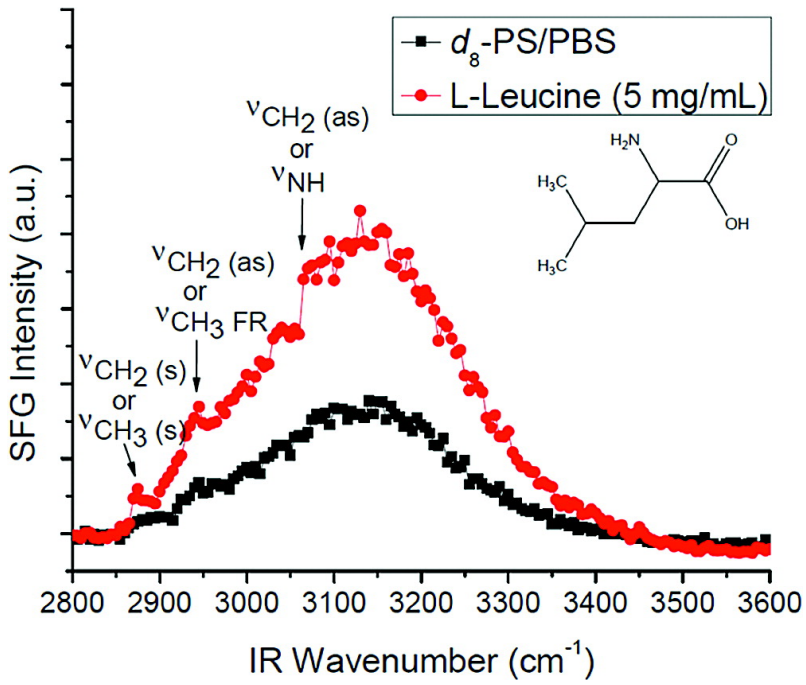

Figure 9.2: SFG spectrum of the d_8PS/PBS interface before (black squares) and after (red circles) the addition of leucine (5 mg/mL). The vibrational mode at 2874 cm^{-1} is attributed to either a CH_3 symmetric stretch from the terminal methyl groups or a CH_2 symmetric stretching mode. The larger peak at 2942 cm^{-1} is indicative of a CH_3 Fermi resonance or a CH_2 asymmetric stretch. The vibrational mode fit in the spectrum at 3056 cm^{-1} may be due to a highly perturbed $CH_2(as)$, NH dimer, or NH stretching vibrational mode.

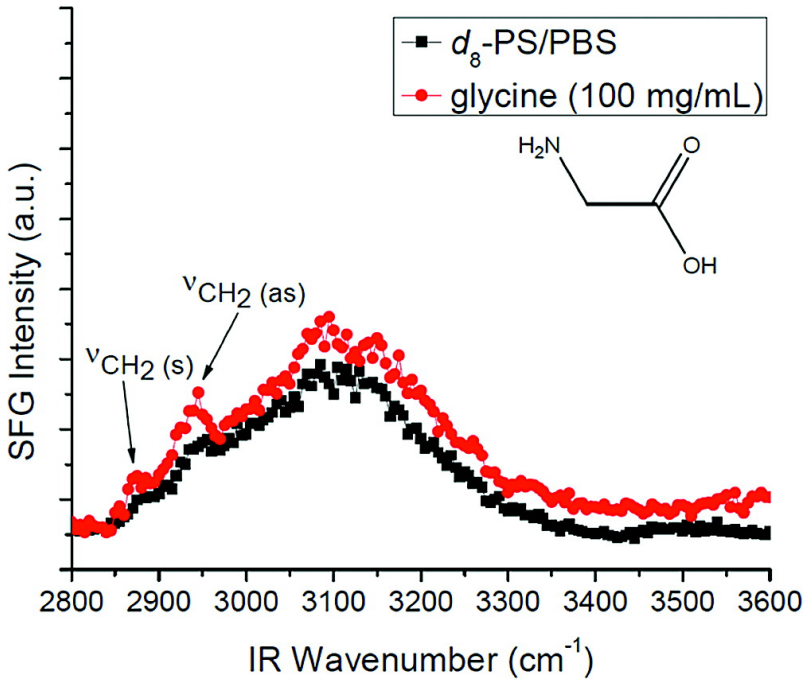

Figure 9.3: SFG spectrum of the d_8PS/PBS interface before (black squares) and after (red circles) the addition of glycine (100 mg/mL). The vibrational mode at 2873 cm^{-1} is attributed to a CH_2 symmetric stretching mode, and the larger peak at 2939 cm^{-1} is identified as originating from a CH_2 asymmetric stretch.

CH features could be identified in this spectrum. A peak found at 2874 cm^{-1} could be attributed to a $CH_{3,ss}$ or $CH_{2,ss}$ or a combination of these[5,6,8,17,19–21]. The mode at 2942 has been attributed to the $CH_{3,fr}$ mode. The origin of a mode at 3056 cm^{-1} is unclear, but may belong to perturbed $CH_{2,as}$, or NH cyclic dimers[15,18]. As with phenylalanine, the addition of amino acid to the solution resulted in a large increase in the signal of water at the interface.

The SFG spectrum of glycine is shown in Figure 9.3. Two peaks in the spectrum (2873, and 2939 cm^{-1}) of glycine can be assigned to $CH_{2,ss}$ and $CH_{2,as}$ modes. Although this would seem to contradict the assignments for peaks of L-leucine, the glycine feature may have shifted due to the high amino acid concentration (100 mg/mL) required to see SFG features from glycine at this surface. The features of water are mostly unchanged by the amino acid introduction, unlike the other amino acids heretofore discussed. Glycine, having only a hydrogen atom as a "side chain" may not be able to induce the same change because it may not strongly prefer any one orientation on the surface of polystyrene.

The spectrum of L-lysine is shown in Figure 9.4. The addition of L-lysine resulted in the appearance of peaks at 2845, 2848, 2874, and 2942 cm^{-1}. The strongest modes in the spectrum at 2874 cm^{-1} and 2942 cm^{-1} have been assigned to $CH_{2,ss}$ and $CH_{2,as}$ modes previously[3]. Although it was possible to fit a peak at 3040 cm^{-1}, the feature reduced the quality of the other peak fits. The water signal is increased on addition of L-lysine and the possible appearance of and NH peak is observed.

Figure 9.5 contains the spectrum of L-arginine at the polystrene/PBS interface. Fitting this spectrum revealed peaks at 2880 cm^{-1} and 2935 cm^{-1}. These are believed to be the

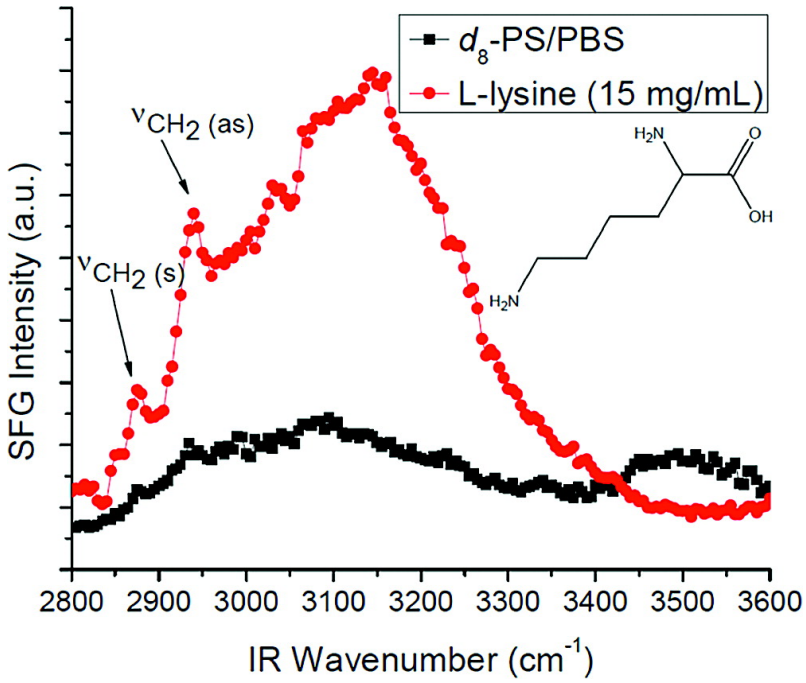

Figure 9.4: SFG spectrum of the d_8PS/PBS interface before (black squares) and after (red circles) the addition of lysine (15 mg/mL). The vibrational mode at 2874 cm^{-1} is attributed to a CH_2 symmetric stretch and a larger peak at 2942 cm^{-1} is indicative of a CH_2 asymmetric stretch from the lysine side chain. The dramatic increase in signal upon the addition of l-lysine is attributed to a change in the net orientation of interfacial water as well as possible contributions from NH stretching modes of the acid's terminal amine group or backbone.

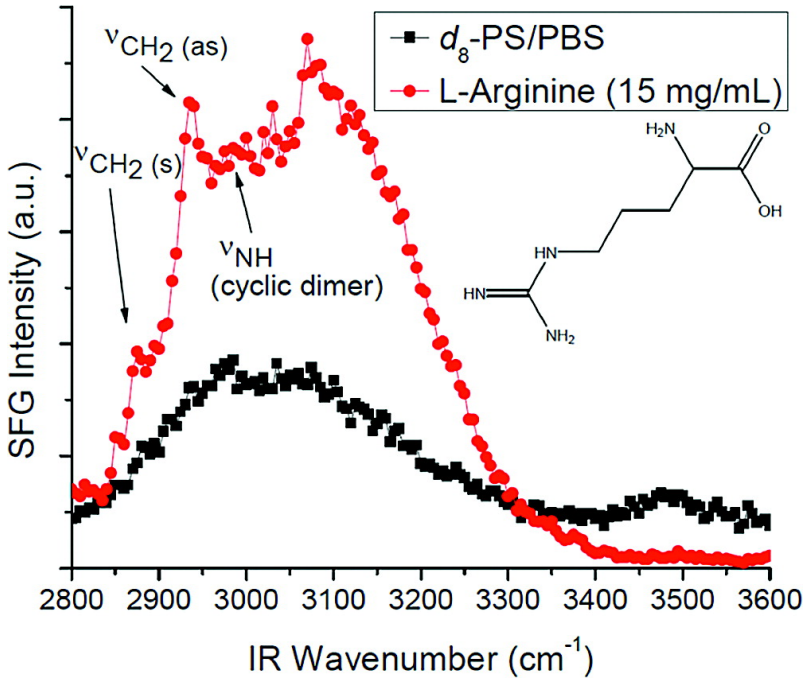

Figure 9.5: SFG spectrum of the d_8PS/PBS interface before (black squares) and after (red circles) the addition of arginine (15 mg/mL). The vibrational mode at 2880 cm^{-1} is attributed to a CH_2 symmetric stretch and a larger peak at 2935 cm^{-1} is indicative of a CH_2 asymmetric stretch. Another peak centered at 2977 cm^{-1} was fit to the spectrum and is attributed to the formation of a cyclic dimer species forming between two neighboring arginine molecules on the hydrophobic surface. The dramatic increase in signal near 3100 cm^{-1} upon the addition of arginine is attributed to change in the net orientation of interfacial water as well as NH stretching modes of the amino acid's terminal guanidino group or backbone.

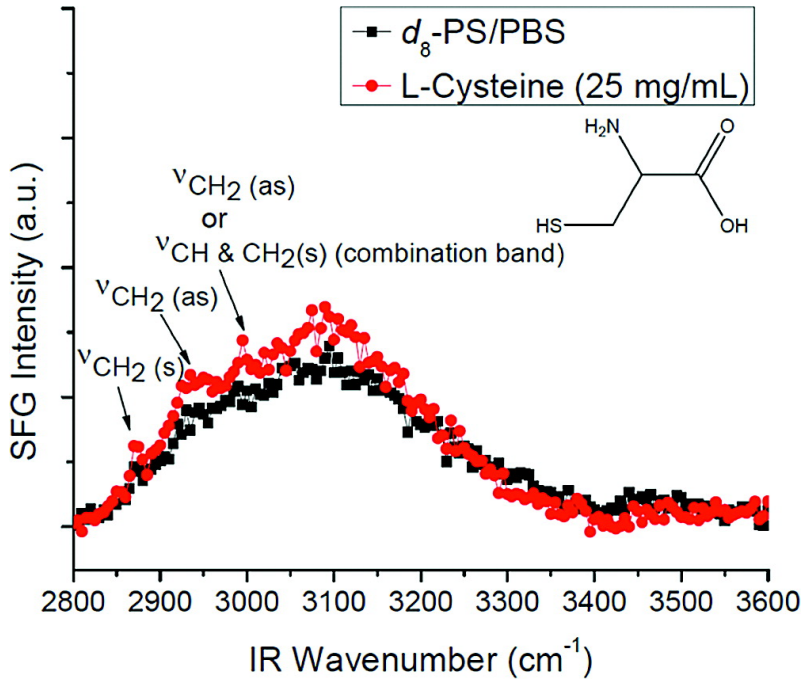

Figure 9.6: SFG spectrum of the d_8PS/PBS interface before (black squares) and after (red circles) the addition of cysteine (25 mg/mL). The vibrational mode at 2872 cm^{-1} is attributed to a CH_2 symmetric stretching mode, and the peak at 2935 cm^{-1} is identified as originating from a CH_2 asymmetric stretch. A third CH vibrational mode is observed at 2993 cm^{-1} and is assigned as either a perturbed $CH_{2,as}$ mode, or a combination band of the $CH_{2,ss}$ and CH stretches of solvated cysteine molecules.

symmetric and asymmetric stretching modes of the methylene groups of the amino acid side chain. We assign a peak at 2977 cm^{-1} to NH cyclic dimer formation[15]. L-arginine had a similar effect to lysine, leucine and phenylalanine, in that it increased the signal of water. It is similar to lysine in that it may also contribute to the spectrum with its NH group.

L-cysteine at the PBS/d_8-polystyrene interface shows symmetric and asymmetric CH_2 stretches at 2872 and 2935 cm^{-1} (Figure 9.6). A peak at 2993 cm^{-1} is difficult to assign, but this could be a perturbed CH_2 mode, as recent computational work has shown the possibility of such a mode at approximately that frequency. L-cysteine is like glycine in its small effect on the overall intensity of the water signal.

The spectrum of L-proline is shown in Figure 9.7. The CH modes seen in this spectrum are at 2875 cm^{-1}, possibly a combination band of $C_\beta H_2$, $C_\gamma H_2$, and $C_\delta H_2$, and at 2934 cm^{-1}, similarly a combination mode, and at 2984 cm^{-1}, from a combination of $C_\beta H_2$, $C_\gamma H_2$ modes[3,22]. The asymmetric modes are higher in frequency than for other amino acids, due to the strain in the proline ring. The signal above 3000 cm^{-1} shows the greatest change of all the amino acids which comes from a dramatic reoganization of the interfacial water and NH stretcing modes from the amino acid[23–25]. In fact the broad peaks are almost always a complicated combination of multiple OH (and in this case NH) features which are broadened due to various extents of hydrogen bonding.

The SFG spectrum of L-alanine is shown in Figure 9.8. The spectrum of L-alanine shows

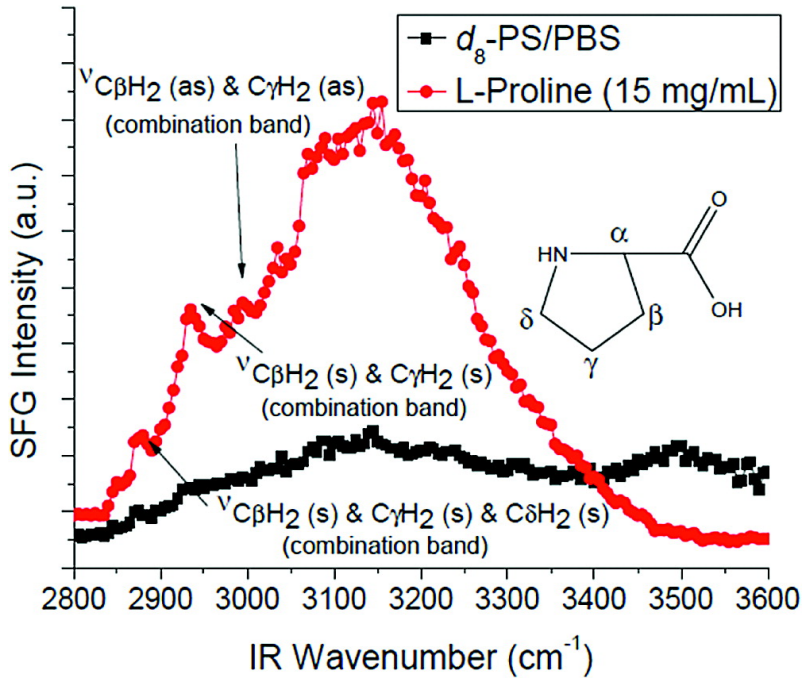

Figure 9.7: SFG spectrum of the d_8PS/PBS interface before (black squares) and after (red circles) the addition of proline (15 mg/mL). The vibrational mode at 2875 cm^{-1} is attributed to a combination of $C_\beta H_2$ (s), $C_\gamma H_2$ (s), and $C_\delta H_2$ (s) modes. The peak at 2934 cm^{-1} is identified as combination mode from $C_\beta H_2$ (s) and $C_\gamma H_2$ (s) vibrations. Finally, the combination mode at 2984 cm^{-1} originates from $C_\beta H_2$ (as) and $C_\gamma H_2$ (as) vibrations. The broad increase of SFG signal in the region 3000-3400 cm^{-1} upon the addition of proline is attributed to change in the net orientation of interfacial water as well as NH stretches of the heterocyclic amino acid.

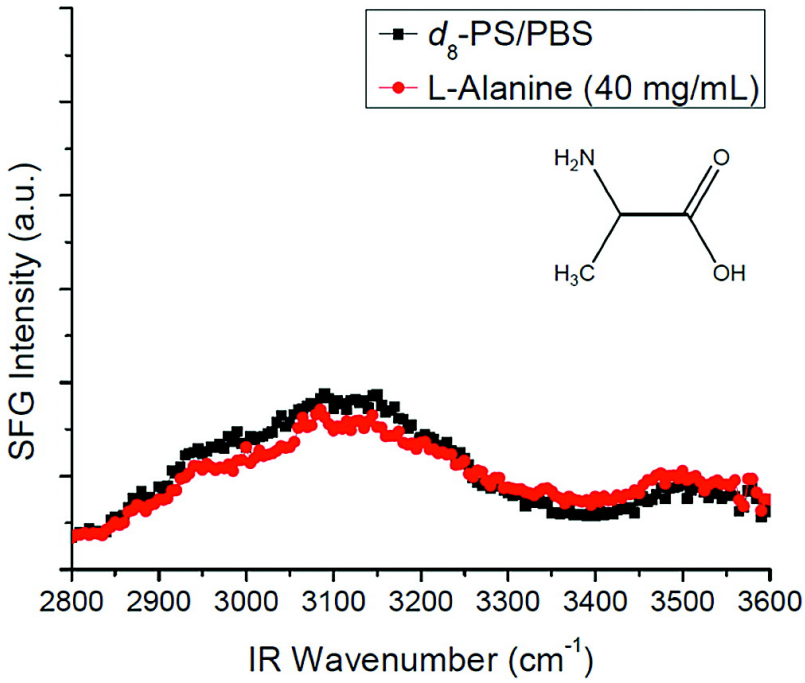

Figure 9.8: SFG spectrum of the d_8PS/PBS interface before (black squares) and after (red circles) the addition ofalanine (40 mg/mL). No CH vibrational modes are observed, and the water signal is unperturbed after the adsorption of amino acid.

no CH modes in the spectrum at this interface. The background intensity is also unchanged upon addition of the amino acid. QCM however shows that the molecule is indeed adsorbed on the surface with a coverages of 469 ± 33 nm/cm^2. The SFG silence of this molecule, which is favorably adsorbed on the polystyrene surface, could be attributed to the lack of ordering of the molecule at the interface.

SFG data at the hydrophilic SiO_2 interface

The SFG spectra of PBS at the SiO_2 interface is shown in Figures 9.10-9.17 as background spectra. Two broad features at 3200 and 3400 cm^{-1} are seen in these spectra, which are attributed to the OH stretching modes of water. As discussed above the OH stretching modes are often referred to as "ice-like" and "liquid-like".

No amino acid at the SiO_2 interface was seen to have clear CH stretch modes in the SFG spectra. However, just as at the polystyrene interface, the presence of amino acids at the interface had a significant effect on the SFG signal of water. This is in accord with work that showed that charged adsorbates alter OH vibrational features of water[26]. The absence of CH features is attributed to the zwitterionic interactions between amino acids and the negatively charged SiO_2 surface under these conditions. We expect that the adsorption will be driven by Coulombic forces, causing the amino acid to adsorb through the charged ends rather than the side chain.

Figures 9.10-9.12 show the SFG spectra of L-leucine, L-argnine and L-lysine at the hydrophilic SiO_2 interface. All of these spectra show an enhancement of the OH peaks from

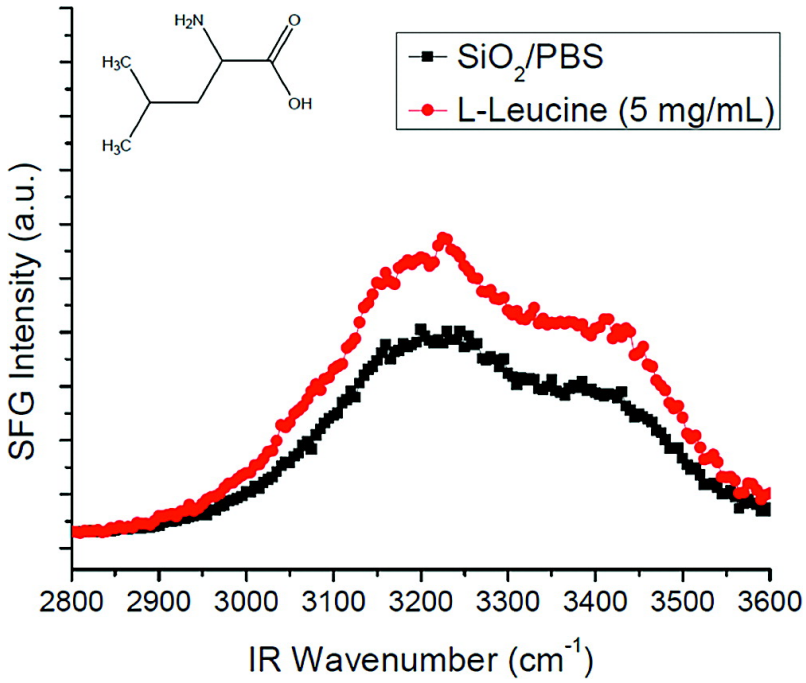

Figure 9.9: SFG spectrum of PBS/SiO_2 interface before (black squares) and after (red circles) addition of leucine (5 mg/mL). No hydrocarbon vibrational modes are observed, but an enhancement in the broad spectral features at 3200 and 3400 cm^{-1} occurs upon the addition of leucine. This result suggests that the presence of the hydrophobic amino acid can cause a change in the net orientation of interfacial water at the SiO_2/PBS interface.

water upon adsorption of the amino acids. Basic SFG theory dictates that the net orientation of molecules at an interface will cause a high signal in the case of a highly ordered interface or a low signal in the case of little ordering. Therefore we attribute the change in water signal to an increase in the ordering of water at the SiO_2 interface. It is not surprising that a doubly charged amino acid would have a strong interaction with water molecules, causing a large change in the overall structure of the surface. QCM confirms the presence of L-arginine on the surface of silica. Therefore we attribute the lack of CH features from this amino acid to its lack of order on the surface.

Glycine, L-cysteine and L-alanine SFG spectra are shwon in Figures 9.13-9.15. All of these amino acids resulted in a *decrease* of the SFG intensity of water at the silica surface. The decrease could be due to a change in orientation of water molecules or the displacement of water from the silica surface as a results of the adsorption of amino acid. As with the other amino acids, none of these molecules produced a CH feature in these spectra.

L-phenylalanine and L-proline had no effect on the SFG spectra at the silica interface. Neither the "ice-like" water signal nor the "liquid-like" water signal show any change upon the addition of amino acid in either of these spectra. QCM measurements confirmed the adsorption of amino acids at this interface, however, no evidence of their presence was seen in the SFG spectra. Previous work at higher concentrations of L-proline were seen to have a decreasing effect in the SFG intensity of water at the surface[3]. In that study, some CH peaks were observed indicating that the L-proline may have the effect of displacing water

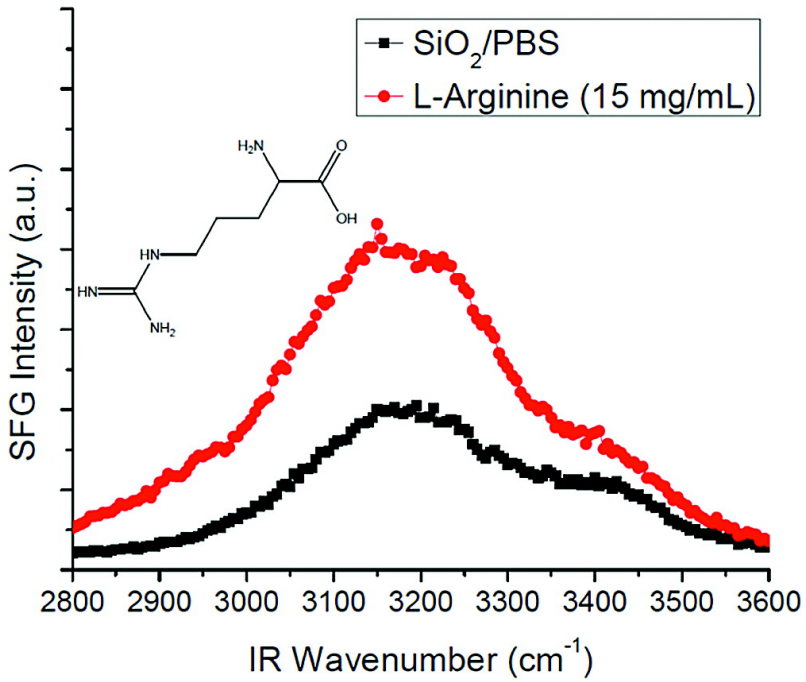

Figure 9.10: SFG spectrum of PBS/SiO_2 interface before (black squares) and after (red circles) addition of arginine (15 mg/mL). No hydrocarbon vibrational modes are observed upon the addition of arginine, but an enhancement and substantial peak broadening occurs in the spectral features at 3200 and 3400 cm^{-1}. This result suggests that the presence of the arginine can cause a change in the net orientation of interfacial water at the SiO_2/PBS interface.

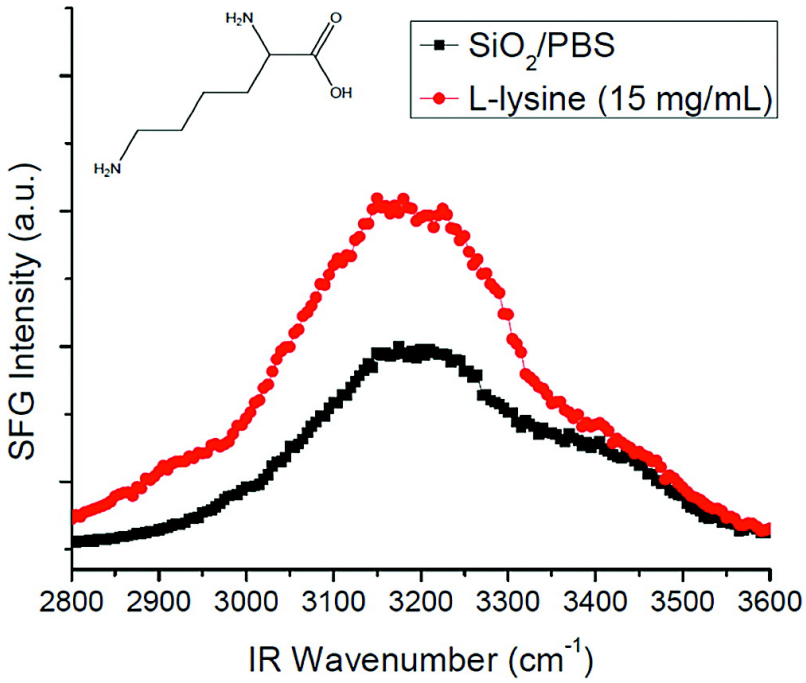

Figure 9.11: SFG spectrum of PBS/SiO_2 interface before (black squares) and after (red circles) addition of (15 mg/mL). No hydrocarbon vibrational modes are observed upon the addition of arginine. However, similar to the SFG spectrum of l-arginine at the SiO_2/PBS interface, this spectrum shows a significant enhancement and peak broadening occurring in the spectral features at 3200 and 3400 cm^{-1}. This result suggests that the presence of the lysine amino acid molecules causes a change in the net orientation of interfacial water at the SiO_2/PBS interface.

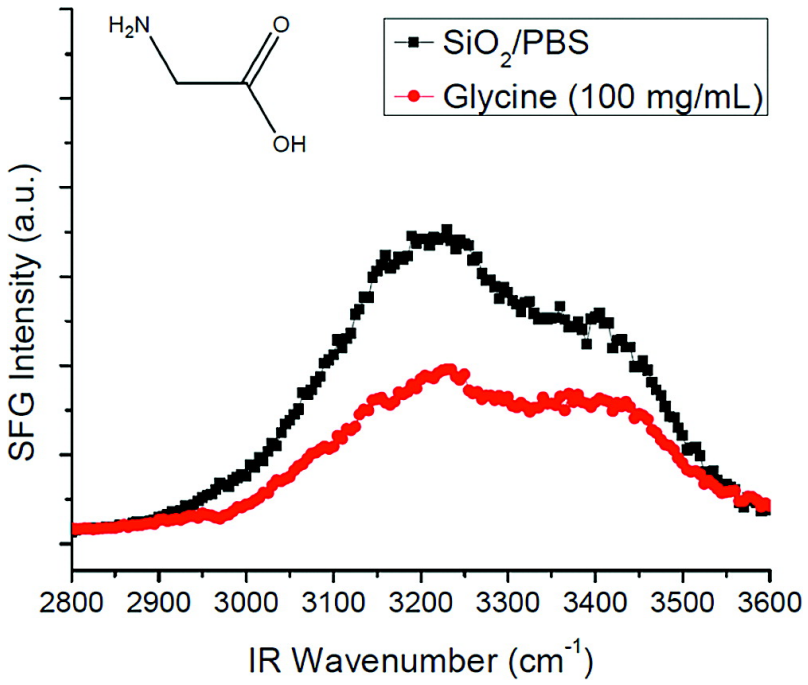

Figure 9.12: SFG spectrum of the SiO_2/PBS interface before (black squares) and after (red circles) the addition of glycine (100 mg/mL). SFG signals at 3200 and 3400 cm^{-1} are reduced upon addition of the amino acid.

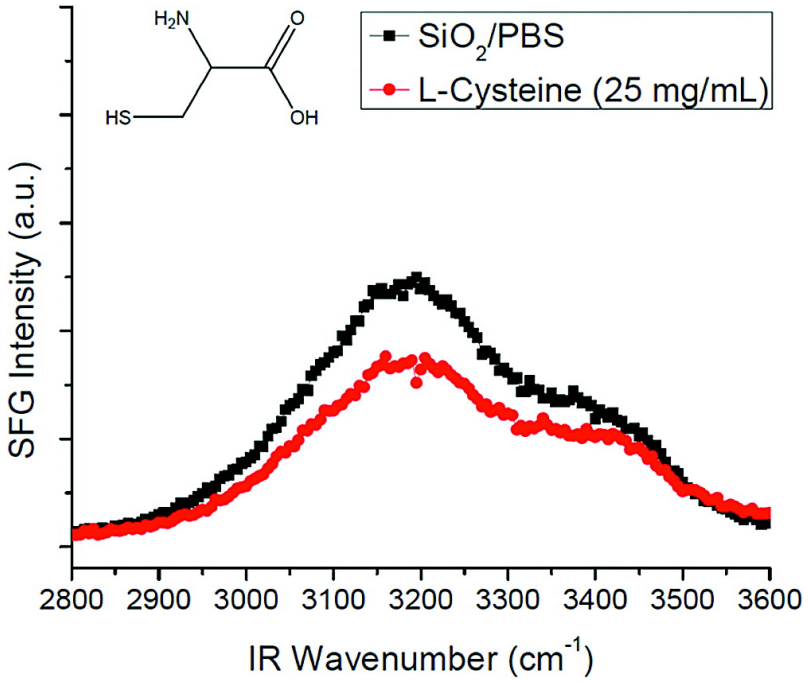

Figure 9.13: SFG spectrum of the SiO_2/PBS interface before (black squares) and after (red circles) the addition of l-cysteine (25 mg/mL). SFG signals at 3200 and 3400 cm^{-1} are reduced upon addition of the amino acid.

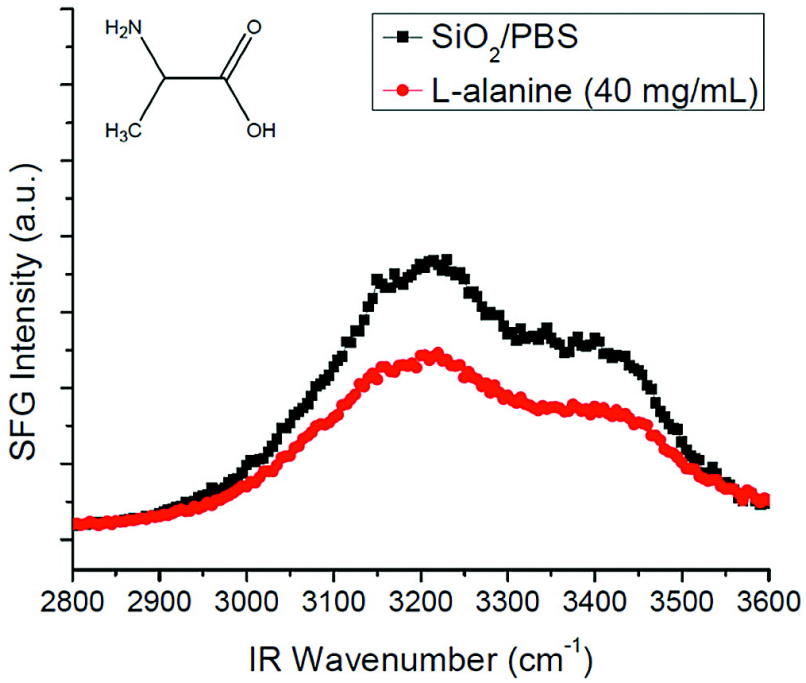

Figure 9.14: SFG spectrum of the SiO_2/PBS interface before (black squares) and after (red circles) the addition of alanine (40 mg/mL). SFG signal at 3200 and 3400 cm^{-1} are reduced upon addition of the amino acid.

from the surface of silica.

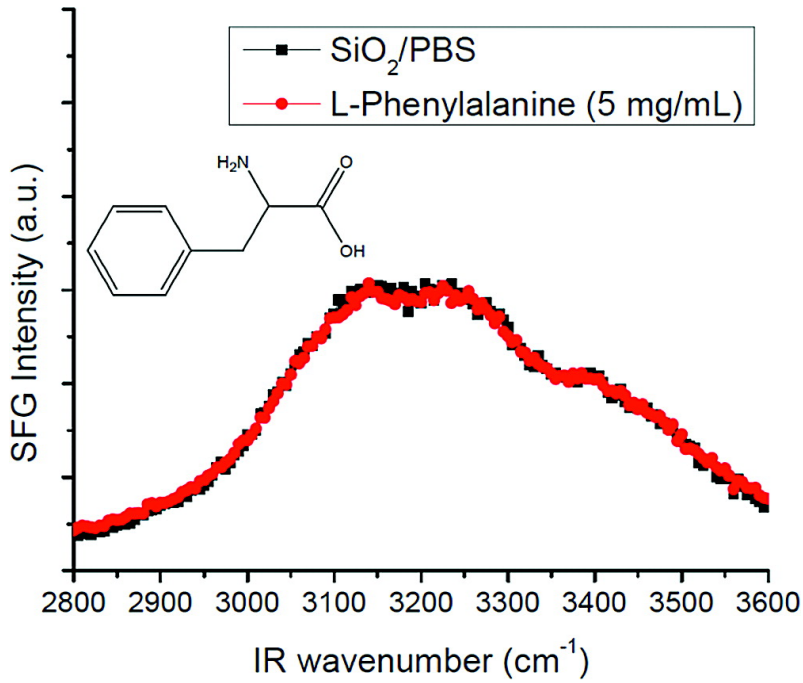

Figure 9.15: SFG spectrum of PBS/SiO_2 interface before (black squares) and after (red circles) addition of phenylalanine (5 mg/mL). No changes in water signal at 3200 or 3400 cm^{-1} are observed upon the addition of amino acid.

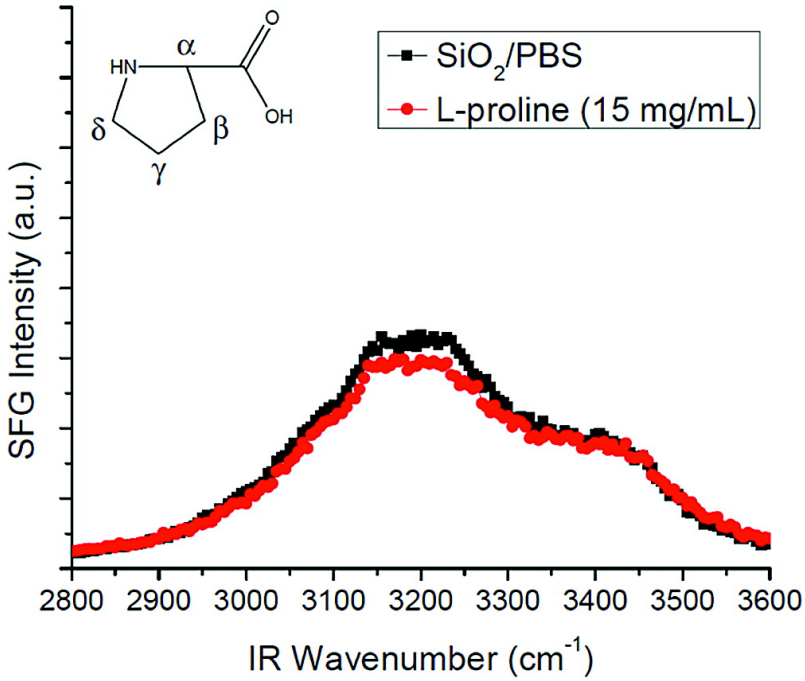

Figure 9.16: SFG spectrum of the SiO_2/PBS interface before (black squares) and after (red circles) the addition of proline (15 mg/mL). No changes in water signal at 3200 or 3400 cm^{-1} are observed upon the addition of amino acid.

Conclusions

In this study, we have investigated the adsorption of eight amino acids at hydrophilic and hydrophobic surfaces. The SFG results indicate that under most circumstances the adsorption of amino acids at the surface has a significant effect on the orienation or overall concentration (possible both) of interfacial water. This was seen in the increase and decrease of "ice-like" and "liquid-like" water peaks for almost all the amino acids at both hydrophilic and hydrophobic interfaces. The extent to which the amino acids cause the reorientation of water varies widely and is dependent on the identity of the amino acid.

References

[1] Hall, S.; Hickey, A.; Hore, D. *Journal Of Physical Chemistry C* **2010**, *114*, 9748–9757.

[2] Paszti, Z.; Guczi, L. *Vibrational Spectroscopy* **2009**, *50*, 48–56.

[3] York, R.; Holinga, G.; Somorjai, G. *Langmuir* **2009**, *25*, 9369–9374.

[4] Holinga, G.; York, R.; Onorato, R.; Thompson, C.; Webb, N.; Yoon, A.; Somorjai, G. *J. Am. Chem. Soc.* **2011**, 6243.

[5] Mermut, O.; York, R.; Phillips, D.; Mccrea, K.; Ward, R.; Somorjai, G. *Biointerphases* **2006**, *1*, P5–P11.

[6] York, R.; Mermut, O.; Phillips, D.; Mccrea, K.; Ward, R.; Somorjai, G. *Journal Of Physical Chemistry C* **2007**, *111*, 8866–8871.

[7] York, R.; Li, Y.; Holinga, G.; Somorjai, G. *Journal Of Physical Chemistry A* **2009**, *113*, 2768–2774.

[8] Mermut, O.; Phillips, D.; York, R.; Mccrea, K.; Ward, R.; Somorjai, G. *Journal Of The American Chemical Society* **2006**, *128*, 3598–3607.

[9] Tian, C.; Shen, Y. *Chemical Physics Letters* **2009**, *470*, 1–6.

[10] Sovago, M.; Campen, R.; Bakker, H.; Bonn, M. *Chemical Physics Letters* **2009**, 7–12.

[11] Noah-Vanhoucke, J.; Smith, J.; Geissler, P. *Journal Of Physical Chemistry B* **2009**, *113*, 4065–4074.

[12] Auer, B.; Skinner, J. *Chemical Physics Letters* **2009**, 13–20.

[13] Fan, Y.; Chen, X.; Yang, L.; Cremer, P.; Gao, Y. *Journal Of Physical Chemistry B* **2009**, *113*, 11672–11679.

[14] Larsson, L. *Acta Chemica Scandinavica* **1950**, *4*, 27–38.

[15] Sutherland, G. *Advances In Protein Chemistry* **1952**, *7*, 291–318.

[16] Weidner, T.; Breen, N.; Drobny, G.; Castner, D. *Journal Of Physical Chemistry B* **2009**, *113*, 15423–15426.

[17] Phillips, D.; York, R.; Mermut, O.; Mccrea, K.; Ward, R.; Somorjai, G. *Journal Of Physical Chemistry C* **2007**, *111*, 255–261.

[18] York, R.; Browne, W.; Geissler, P.; Somorjai, G. *Israel Journal Of Chemistry* **2007**, *47*, 51–58.

[19] Watry, M.; Richmond, G. *Journal Of Physical Chemistry B* **2002**, *106*, 12517–12523.

[20] Ji, N.; Shen, Y. *Journal Of Chemical Physics* **2004**, *120*, 7107–7112.

[21] Breen, N.; Weidner, T.; Li, K.; Castner, D.; Drobny, G. *Journal Of The American Chemical Society* **2009**, *131*, 14148–+.

[22] Reva, I.; Stepanian, S.; Plokhotnichenko, A.; Radchenko, E.; Sheina, G.; Blagoi, Y. *Journal Of Molecular Structure* **1994**, *318*, 1–13.

[23] Krimm, S.; Dwivedi, A. *Journal Of Raman Spectroscopy* **1982**, *12*, 133–137.

[24] Miyazawa, T. *Journal Of Molecular Spectroscopy* **1960**, *4*, 168–172.

[25] Krimm, S.; Bandekar, J. *Advances In Protein Chemistry* **1986**, *38*, 181–364.

[26] Chen, X.; Flores, S.; Lim, S.; Zhang, Y.; Yang, T.; Kherb, J.; Cremer, P. *Langmuir* **2010**, *26*, 16447–16454.

DISCLAIMER

This document was prepared as an account of work sponsored by the United States Government. While this document is believed to contain correct information, neither the United States Government nor any agency thereof, nor the Regents of the University of California, nor any of their employees, makes any warranty, express or implied, or assumes any legal responsibility for the accuracy, completeness, or usefulness of any information, apparatus, product, or process disclosed, or represents that its use would not infringe privately owned rights. Reference herein to any specific commercial product, process, or service by its trade name, trademark, manufacturer, or otherwise, does not necessarily constitute or imply its endorsement, recommendation, or favoring by the United States Government or any agency thereof, or the Regents of the University of California. The views and opinions of authors expressed herein do not necessarily state or reflect those of the United States Government or any agency thereof or the Regents of the University of California.